Chem Soc Rev

REVIEW ARTICLE

View Article Online
View Journal | View Issue

Cite this: *Chem. Soc. Rev.*, 2021, **50**, 3143

Pyrene-based metal organic frameworks: from synthesis to applications

F. Pelin Kinik, † Andres Ortega-Guerrero, † Daniele Ongari, Christopher P. Ireland and Berend Smit *

Pyrene is one of the most widely investigated aromatic hydrocarbons given to its unique optical and electronic properties. Hence, pyrene-based ligands have been attractive for the synthesis of metal–organic frameworks (MOFs) in the last few years. In this review, we will focus on the most important characteristics of pyrene, in addition to the development and synthesis of pyrene-based molecules as bridging ligands to be used in MOF structures. We will summarize the synthesis attempts, as well as the post-synthetic modifications of pyrene-based MOFs by the incorporation of metals or ligands in the structure. The discussion of promising results of such MOFs in several applications; including luminescence, photocatalysis, adsorption and separation, heterogeneous catalysis, electrochemical applications and bio-medical applications will be highlighted. Finally, some insights and future prospects will be given based on the studies discussed in the review. This review will pave the way for the researchers in the field for the design and development of novel pyrene-based structures and their utilization for different applications.

Received 10th September 2020

DOI: 10.1039/d0cs00424c

rsc.li/chem-soc-rev

1 Introduction

A chromophore is a molecule which is capable of absorbing particular wavelengths of visible light, giving rise to some changes in electron density after the excitation process. Chromophore organic molecules have unique characteristics; such as high charge carrier mobility, light absorption, solution processability, thermal stability, and availability for the coordination with metal ions.[1] Among chromophoric materials, conjugated π-systems are perfect candidates for applications based on fluorescence, phosphorescence, or charge separation.[2] Pyrene is a highly symmetrical four-benzene-ringed polycyclic aromatic hydrocarbon, which is one of the most studied chromophore molecules after its discovery in the residue of the distillation of coal tar in 1837.[3] After it became commercially available, the first use of pyrene was for the synthetic dye industry thanks to its intense yellow colour. With the discovery of its favorable properties as being a "fluorophore"

Laboratory of Molecular Simulation (LSMO), Institut des Sciences et Ingénierie Chimiques (ISIC), Ecole Polytechnique Fédérale de Lausanne (EPFL), Rue de l'Industrie 17, CH-1951 Sion, Valais, Switzerland. E-mail: berend.smit@epfl.ch
† These authors contributed equally to this work.

F. Pelin Kinik

Fatma Pelin Kinik received her BSc degree (2015) in Chemical Engineering from Istanbul Technical University (Turkey). She received her MSc degree (2017) in Chemical & Biological Engineering Department of Koç University (Turkey). Currently, she is a PhD student under the supervision of Prof. Berend Smit at EPFL, focusing on hydrogen generation using MOFs by heterogeneous catalysis and photocatalysis.

Andres Ortega-Guerrero

Andres Ortega-Guerrero received his undergraduate degree in electronics engineering from Universidad del Valle in Cali, Colombia. Later he received a MSc on Nanoscience and Nanotechnology from Katholieke Universiteit Leuven, Belgium and Technische Universität Dresden, Germany. Currently, he is a PhD student in Berend Smit's group, investigating the electronic and optical properties of MOFs for photocatalysis using computational methods.

with excellent emission properties, having long excited-state lifetime and successful electron hole-pair dissociation, pyrene has been one of the most investigated aromatic hydrocarbons.[4]

Pyrene molecule allows the addition of different functional groups by traditional synthetic techniques such as formylation/acetylation, bromination, de-*tert*-butylation, oxidation, and borylation reactions.[1] In this way, pyrene-based molecules have been used as substrates in the synthesis of molecules such as nanographenes and metal cages.[5] In addition, the optical properties of pyrene have been exploited in different materials such as organic light-emitter diodes (OLEDs) due to its emission characteristics, as well as organic photovoltaics (OPVs) and solar cells due to its absorption properties.[1]

Owing to their promising optical and structural characteristics, pyrene-based molecules have attracted the researchers in the field of metal–organic frameworks (MOFs) to be used as ligands. MOFs are crystalline materials consist of metal-based building blocks linked by organic bridging ligands. By the careful combining of these metal nodes with these ligands, MOFs with desired properties can be obtained for target applications. The optical characteristics of pyrene as a MOF-ligand give pyrene-based MOFs some promising optical properties. These include its excimer formation combined with long-lived excited states, high fluorescence quantum yield, exceptional distinction of the fluorescence bands for monomer and excimer, and the sensitivity of its excitation spectra to micro-environmental changes.[4] The coordination of pyrene-based ligands with metal centres can give rise to new photophysical and photochemical properties, which cannot be observed if the pyrene molecule is isolated.[6] These properties have been successfully incorporated in MOF structures to the design of an extensive variety of luminescence and photocatalytic applications. The functionalization of pyrene with different groups including carboxylates, phosphonates, and sulfonates facilitates the generation of different MOF structures with diverse metal-ion coordination chemistry. Thanks to the structural variability and aromaticity of pyrene-based ligands, MOFs with promising features (*e.g.*, large surface area, suitable pore size and shape, π–π stacking interactions) can be obtained for the adsorption and separation of different molecules. Moreover, the introduction of pyrene-based ligands into the MOF structures can enhance the electron transfer efficiency due to the strong π–π interactions between the pyrene and the reactant molecule, resulting in promising activity in heterogeneous catalytic applications. Consequently, pyrene-based MOFs are a growing field with published structures in the literature displaying interesting topological, optical, and physicochemical properties covering a suprisingly large number of different applications.

This increasing number of studies of pyrene-based MOFs in different fields has motivated this review. One can find reviews relate other chromophoric MOF families, such as porphyrin-based MOFs.[7–9] In this review article, the reader can find information about the design and the development of pyrene-based molecules as organic linkers for MOF synthesis. The synthesis of pyrene-based MOFs and their post-synthetic modification using different methods (*e.g.*, atomic layer deposition

Daniele Ongari

Daniele Ongari received his diploma in chemical engineering from Politecnico di Milano. In 2019, he completed his PhD under the supervision of Prof. Berend Smit at EPFL. His research focuses on the investigation of microporous materials, in particular MOFs and COFs, using computational methods to assess their performances for molecular adsorption and catalysis.

Christopher P. Ireland

Christopher P. Ireland obtained his PhD under the supervision of Prof. Matthew J. Rosseinsky at the University of Liverpool, where his work involved the synthesis of metal oxides for photocatalytic and optical applications. After time at UCL and the University of Cambridge, he was awarded a Marie Curie Fellowship in 2015 to move to the LSMO group at EPFL, led by Prof. Berend Smit. His research interests at EPFL involves the synthesis and characterization of metal–organic frameworks for environmental applications, such as carbon capture, and photocatalytic hydrogen generation.

Berend Smit

Berend Smit received a MSc in Chemical Engineering in 1987 and a MSc in Physics both from the Technical University in Delft. In 1990, he received a cum laude PhD in Chemistry from Utrecht University. He was a (senior) Research Physicists at Shell Research before he joined the University of Amsterdam. In 2004, he was elected Director of the European Center of Atomic and Molecular Computations (CECAM) Lyon France. In 2007 he became Professor of Chemical Engineering and Chemistry at U. C. Berkeley and Faculty Chemist at LBNL. Since July 2014 he is full professor at EPFL.

in MOFs to install metal ions (AIM), solvothermal deposition in a MOF (SIM), or solvent-assisted ligand incorporation (SALI)) are covered in detail. The nature of pyrene proposes different optical characteristics by exploiting its ground and excited state properties, which makes this molecule appealing for many applications. In addition, pyrene-based MOFs can lead to unique topology-based properties as a result of combining pyrene molecule with different transition metal ions. MOFs offer a great platform to combine different electronic, physicochemical, and topological properties in one porous material. Therefore, a specific application can take advantage of either one or couple of these characteristics at the same time. In this review, we discuss the most promising results of such pyrene-based MOFs combining different properties in several applications; including luminescence sensing, photocatalysis, adsorption and separation of molecules, heterogeneous catalysis, electrochemistry applications and biomedical applications. This review can pave a way for researchers working on the development of novel pyrene ligands and pyrene-based MOFs for different applications.

2 Design and synthesis of pyrene-based metal organic frameworks (MOFs)

2.1 Pyrene-based building blocks as organic linkers in MOFs

Thanks to its fascinating characteristics, pyrene has been considered as a starting material for creating building blocks for MOFs, which makes this molecule even more attractive. By using pre-existing pyrene as the core, different electrophilic aromatic substitutions at different positions can be applied by direct or indirect methods, resulting in (i) 1-substituted pyrenes, (ii) 1,3,6,8-tetrasubstituted pyrenes, (iii) 1,6- and 1,8-disubstituted pyrenes, (iv) 1,3-disubstituted pyrenes, (v) 2,7-disubstituted pyrenes, and (vi) 4,5,9,10-tetrasubstituted pyrenes (Fig. 1).[4] Among the substituted pyrene molecules, 1,3,6,8-tetra substituted pyrenes are the most studied ones for designing building blocks to be used in MOF synthesis. Being the most electron-rich and active centers, 1-, 3-, 6- and 8-positions on the pyrene core are the most favourable connection points for the electrophilic substitution, based on both experimental results and the calculations of molecular orbitals.[4] According to theoretical calculations, the energy of the 1-, 3-, 6-, and 8-positions are lower by 8.8 kcal mol^{-1} than the 2- and 7-positions.[1] There are several in-depth articles on the design and synthesis of substituted pyrenes that can participate in creating different molecular architectures.[4,10,11]

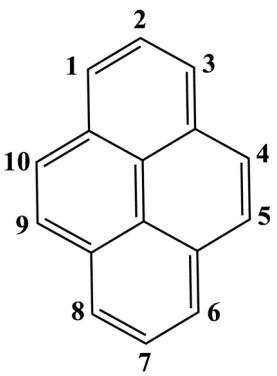

Fig. 1 Illustration of the aromatic substitutions at different positions of pyrene.

The bromine atom of a C–Br bond can easily be transformed to a C–C bond, C–N bond, or other group by Pd-catalyzed cross-coupling reactions.[1] Given this, bromopyrenes have been thoroughly explored as key precursors for constructing building block materials. The synthesis of 1,3,6,8-tetrabromopyrene by Suzuki or Sonogashira coupling reactions gave rise to a increasing number of functionalized pyrene structures, which can be used in the synthesis of MOFs as organic ligands.[4] The interest in the design of pyrene-based building blocks for MOF synthesis has tremendously increased after the synthesis of some novel pyrene-based tetratopic ligands. An important milestone was the synthesis of 1,3,6,8-tetrakis(*p*-benzoic acid)pyrene (TBAPy) ligand, which was obtained using a standard Suzuki–Miyaura reaction between 1,3,6,8-tetrabromopyrene and (4-(ethoxycarbonyl)phenyl)boronic acid, to design a fluorescent-MOF to respond to small guest molecules.[12] TBAPy is a fluorescent ligand where the pyrene core is relatively rigid, and the benzoate groups substituted at the 1-, 3-, 6-, and 8-positions have a degree of rotational freedom. The carboxylate groups make this molecule attractive to link to the metal in a MOF. To date, different types of metals including alkali earth metals, transition metals, and post-transition metals have been coordinated with TBAPy ligand, resulting in 3D networks. These structures will be discussed in detail in the following sections. Following the interest on TBAPy, the researchers lately have focused on the synthesis of bulkier ligands by the incorporation of longer aromatic chains, such as biphenyl carboxylate and phenylethynyl carboxylate groups. Although tetra-substituted pyrenes are the most studied ligands for pyrene-based MOF synthesis, some other-mono and -di coordinated carboxylate-pyrene ligands and pyrene itself have also been studied for MOF synthesis. The functionalization of 2- and 7-positions on pyrene towards electrophilic aromatic substitution are less favorable than 1-, 3-, 6- and 8-positions, yet they can be activated selectively if a very bulky electrophile is employed.[10] Pyrene-2,7-dicarboxylic acid (H_2PDC) is as an example of the 2,7-disubstituted building blocks used in MOF synthesis. A Zn-MOF synthesized with H_2PDC (IRMOF-14)[13] has been particularly interesting thanks to its metal-substituted analogues M-IRMOF-14 (M = Zn, Cd, Be, Mg, Ca, Sr) with different chemical bonding, electronic structure, and optical properties.[14] Table 1 summarizes the structures and short names of pyrene-based ligands used in the synthesis of different MOFs to date.

2.2 Synthesis of pyrene-based MOFs

The first use of pyrene molecule with MOFs was in 1995, where it was intercalated into a copper(I) coordination polymer as a guest molecule.[15] The solvation of crystal data demonstrated that pyrene molecules could be placed in between the phazine

Table 1 The summary of pyrene-based MOFs. The interactive version of this table, for a full visualization of the three-dimensional structure of these MOFs and their pore properties, can be browsed at https://www.materialscloud.org/discover/pyrene-mofs[64]

Pyrene-based ligands	Structures	MOFs	Metals used in MOFs	Ref.
2,7-Pyrenedicarboxylic acid (PDC)		IRMOF-14 MOF-80 Sr(μ-DEF)(μ-PDC) NU-400	Zn(II) Tb(III) Sr(II) Zr(IV)	13 43 45 65
1,3,6,8-Pyrenetetrasulfonate (L_3)	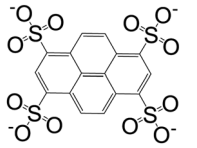	$[Ag_4(L_3)(Pyr)_4(H_2O)2$ $[Dy_4(\mu\text{-pytet})$ $(\mu_4\text{-pytet})_2(DMF)_{20}$ $(H_2O)_2]\cdot 4DMF\cdot 4H_2O]_n$	Ag(I) Dy(III)	44 66
2-(Pyrene-1-carboxamido)terephthalic acid	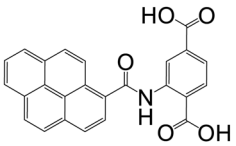	CPP-17-X	Gd(III), Eu(III), and Tb(III)	67
Octaethyl pyrene-1,3,6,8-tetraphosphonate	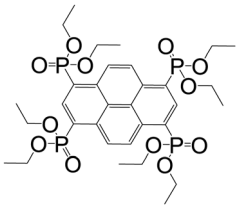	CALF-25	Ba(II)	53
Pyrene-1,3,6,8-tetracarboxylic acid (PTCA)	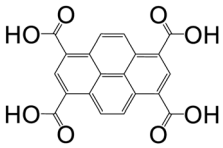	Mg-PTCA Ni-PTCA Zn-PTCA Cd-PTCA NU-1106	Mg(II) Ni(II) Zn(II) Cd(II) Zr(IV)	68 69 70 71 72
1,6-Pyrenedithiolate (PDT)	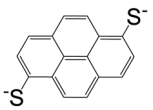	$[Cd(PDT)_2][Cd(en)_3]$	Cd(II)	52
1,6-Bis(diphenyl phosphino)pyrene	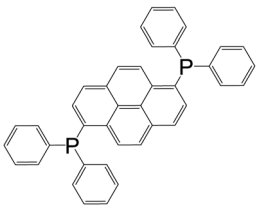	$[Ag_2L_2(OTf)_2]$ $[Cu_2L_2(MeCN)_4]_2^+$ $[Cu_2L_2I_2]$	Ag(I) Cu(I) Cu(I)	48
3,3′,3″,3′′′′-(Pyrene-1,3,6,8-tetrayl)tetrabenzoic acid (PTTB)	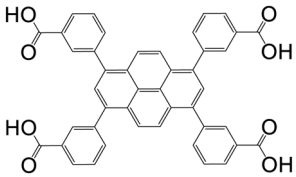	UTSA-72	Zn(II)	73
1,3,6,8-Tetrakis(4-methylthiophenyl)pyrene (L_8)	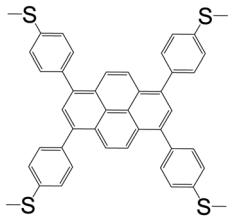	$L_{82}BiBr_3$	Bi(III)	46

Table 1 (*continued*)

Pyrene-based ligands	Structures	MOFs	Metals used in MOFs	Ref.
(4,4′-(2,8-Di-*tert*-butyl-4,10-dihydropyreno[4,5-*d*:9,10-*d*′]diimi-dazole-5,11-diyl)dibenzoic acid) (CIP)	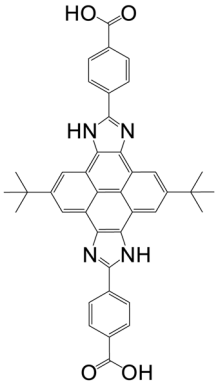	MAS-1	Cu(II)	47
1,3,6,8-Tetrakis(4-carboxylphenyl)pyrene (TBAPy)	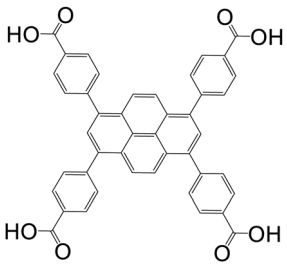	ROD-7	In(III)	12
		Zn-TBAPy	Zn(II)	60
		NU-1000	Zr(IV)	74
		NU-901	Zr(IV)	75
		Ni-TBAPy	Ni(II)	76
		ROD-6	Mn(II)	77
		ROD-8	Cd(II)	57
		NU-505(Zn, Ni)	Zn(II), Ni(II)	78
		Zn-TBAPy	Zn(II)	61
		NU-1300	U(VI)	79
		MLM 1–3	Zr(IV)	80
		MIT-26	Mg(II)	51
		UOF-1, UOF-2	U(VI)	81
		Cd-TBAPy	Cd(II)	58
		$Zr(TBAPy)_5(TCPP)$	Zr(IV)	82
		SION-7	Mg(II)	83
		SION-19	Zn(II)	84
		AlPyr-MOF	Al(III)	85
		Bi-TBAPy	Bi(III)	86
		Bi-TBAPy	Bi(III)	87
		Fe-TBAPy	Fe(II)	88
		Cd-TBAPy	Cd(II)	59
		Yb-TBAPy	Yb(III)	89
		JXNU-5	Eu(III)	90
		SION-8	Ca(II)	91
		Zn-TBAPy	Zn(II)	62
		Bi-NU-901	Bi(III)	92
		bioMOF 1	Zn(II)	93
		Zn-TBAPy	Zn(II)	94
		M-TBAPy (M = Co, Zn)	Co(II), Zn(II)	95
		TDL-Mg	Mg(II)	96
		ACM-1	Ti(IV)	97
		SION-82	Sr(II)	98
1,3,6,8-Tetrakis(3,5-isophthalic acid)pyrene (TIAPy) or 1,3,6,8-tetrakis(3,5-dicarboxyphenyl)pyrene (tdcppy)	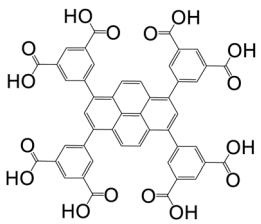	JUC-118	Zn(II)	49
		MgMOF	Mg(II)	99
		Co-tdcppy	Co(II)	100
		JUC-119	Eu(III)	101
		JUC-138	In(III)	102

Table 1 (*continued*)

Pyrene-based ligands	Structures	MOFs	Metals used in MOFs	Ref.
1,3,6,8-Tetrakis(4-(α-carboxy-(*R*)-α-methyl)methoxy-2,6-dimethylphenyl)pyrene (PLA)	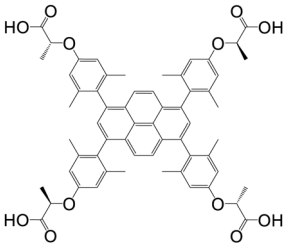	Zn-PLA	Zn(II)	103
3,3′,3″,3‴-(Pyrene-1,3,6,8-tetrayltetrakis(benzene-4,1-diyl))tetraacrylate (PTSA)	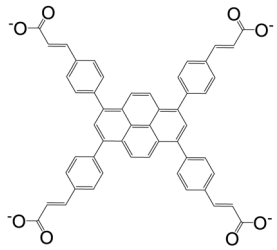	BUT-72	Zr(IV)	55
6,6′,6″,6‴-(Pyrene-1,3,6,8-tetrayl)tetrakis(2-naphthoate)(PTNA)	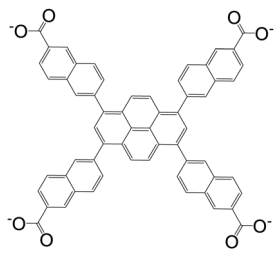	BUT-73 NU-1003	Zr(IV) Zr(IV)	55 104
4,4′,4″,4‴-(Pyrene-1,3,6,8-tetrayltetrakis(ethyne-2,1-diyl))tetrabenzoic acid (PTBA)	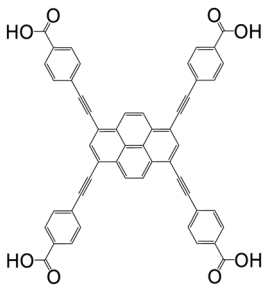	NU-1100 Zrptba	Zr(IV) Zr(IV)	105 54
1,3,6,8-Tetrakis(2,6-dimethyl-4-(α-carboxy)methoxyphenyl)pyrene	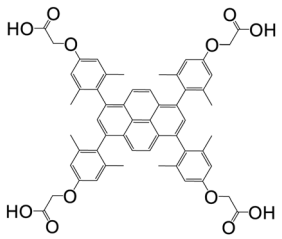	Mn-L	Mn(II)	106
7,7′,7″,7‴-(Pyrene-1,3,6,8-tetrayl)tetrakis(9,9-dimethyl-9H-fluorene-2-carboxylic acid)	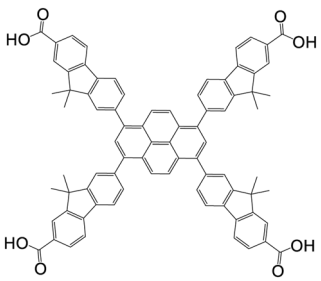	NU-1004	Zr(IV)	107

Table 1 (*continued*)

Pyrene-based ligands	Structures	MOFs	Metals used in MOFs	Ref.
4,4′,4″,4‴-(pyrene-1,3,6,8-tetrayltetrakis(9,9-dimethyl-9H-fluorene-7,2-diyl))tetrabenzoic acid (Py-FP)	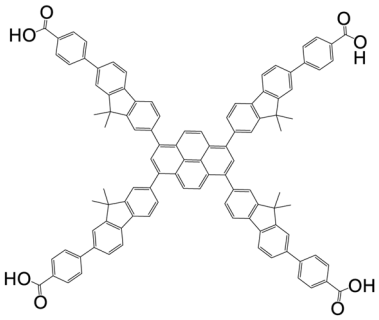	NU-1105	Zr(IV)	108
1,3,6,8-Tetrakis(4′-carboxy[1,1′-biphenyl]-4-yl-)pyrene (TCBPPy)	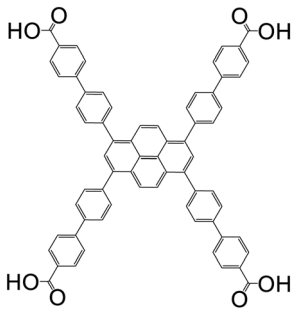	LMOF-1	Zr(IV)	109
4′,4‴,4⁗,4⁗′-(Pyrene-1,3,6,8-tetrayl)tetrakis(2′,5′-dimethyl-[1,1′-biphenyl]-4-carboxylic acid) (Py-XP)	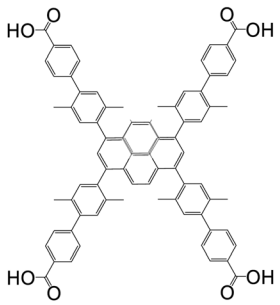	NU-1101	Zr(IV)	50
4,4′,4″,4‴-((2,7-Di-*tert*-butylpyrene-4,5,9,10-tetrayl)tetrakis(ethyne-2,1-diyl))-tetrabenzoate (BPETB)	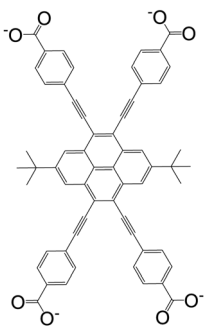	PCN-822(Zr, Hf)	Zr(IV) Hf(IV)	110
4,4′,4″,4‴-((Pyrene-1,3,6,8-tetrayltetrakis(benzene-4,1-diyl))tetrakis(ethyne-2,1-diyl))tetrabenzoic acid (Py-PTP)	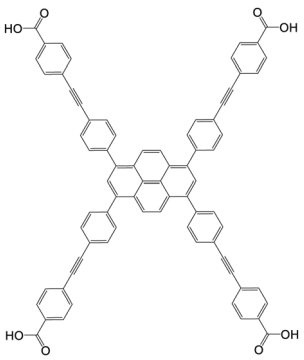	NU-1006 NU-1103	Zr(IV) Zr(IV)	107 50

Table 1 (*continued*)

Pyrene-based ligands	Structures	MOFs	Metals used in MOFs	Ref.
4,4′,4″,4‴-((1*E*,1′*E*,1″*E*,1‴*E*)-(Pyrene-1,3,6,8-tetrayltetrakis(benzene-4,1-diyl))tetrakis(ethene-2,1-diyl))tetrabenzoic acid	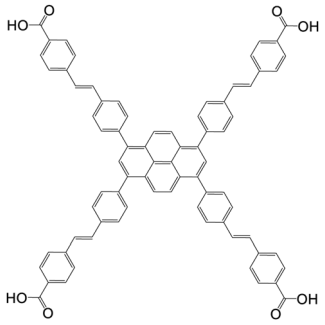	NU-1005	Zr(IV)	107
4′,4″,4‴,4⁗-(Pyrene-1,3,6,8-tetrayl)tetrakis(2′,2″,5′,5″-tetramethyl-[1,1′,4′,1″-terphenyl]-4-carboxylic acid	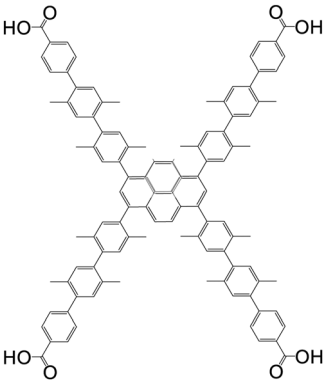	NU-1007	Zr(IV)	107

stacks in a one-dimensional chain thanks to their suitable size and shape. The use of pyrene as a guest molecule in a MOF was performed in many other studies in the following years, to take advantage of the favorable characteristics of pyrene for different applications.[16–39] The pyrene molecule can be included in MOFs also by (i) its attachment to an organic linker, and (ii) its use as a building block for the construction of the MOF after inserting desired functionalizations.[2] In this review, we will mainly focus on the use of pyrene-based organic building blocks in the synthesis of MOFs. The use of pyrene chromophore for constructing MOF structures was first performed by the incorporation of 2,7-diazapyrene[40,41] and naphtho(2,3-*a*)pyrene[42] molecules as building blocks into 1D and 2D coordination polymers. An important study for the use of pyrene molecule in MOF synthesis was the study of Eddaoudi *et al.*,[13] where the systematic design of pore size and functionality in isoreticular MOFs were investigated for methane storage. This study was the first example of a highly porous, 3D pyrene-based metal–organic network. The increasing number of attempts for designing new pyrene-based building blocks has resulted in an increasing number of novel MOF structures. Early studies mainly focused on the design and synthesis of novel pyrene-based MOFs.[43–49] With the increasing attention, investigations have been concentrated on the structural properties,[50–52] and stability of pyrene-based structures in different environments,[53–56] in order to open a road for other researchers in the field. With the better understanding of the structures, the possible applications of these structures have started to be considered, which will be discussed in the following sections.

An interesting feature of pyrene-based MOFs is that the use of the same metal and the ligand in the synthesis can result in different topologies and structural properties. A well-known example is cadmium-based pyrene-MOFs, in which the syntheses have been performed with a specific cadmium salt ($Cd(NO_3)_2 \cdot 4H_2O$) and TBAPy ligand, resulting in three different MOFs with different structures.[57–59] ROD-8 is a 3D rod-type MOF with 1D porous channels and it crystallizes in the monoclinic space group $P21/c$.[57] Although the positions of the oxygens in carboxylates in TBAPy are crystallographically fixed, the pyrene core with four branching phenyl groups can exhibit disorder with two different positions as shown in Fig. 2(a). Depending on the distribution of the two positions of the ligand, ROD-8 can be described by the two extreme ordered derived nets, *lrk* and *lrl*, which are both derived from the basic net *lrj*. ROD-8 was found to be promising for CH_4 capture by virtue of its structural properties. Another example is Cd-TBAPy, which is a 2D layered framework with 1D channels (Fig. 2(b)) crystallized in triclinic space group $P\bar{1}$.[58] Owing to its π-conjugated 2D layered structure and visible-light absorption edge of ≈600 nm, both water reduction and oxidation under visible-light irradiation can be performed with Cd-TBAPy. The last case is $[Cd(TBAPy)(H_2O)_2]\cdot 4(H_2O)_n$ **(S1)**, a 3D structure with 1D chains (Fig. 2(c)) crystallizes in a monoclinic space group $P21/n$.[59] **S1** behaves as a thermometer for fluorescence sensing of temperature in a wide temperature range. Interestingly, the resulting MOFs perform well for such different applications based on their

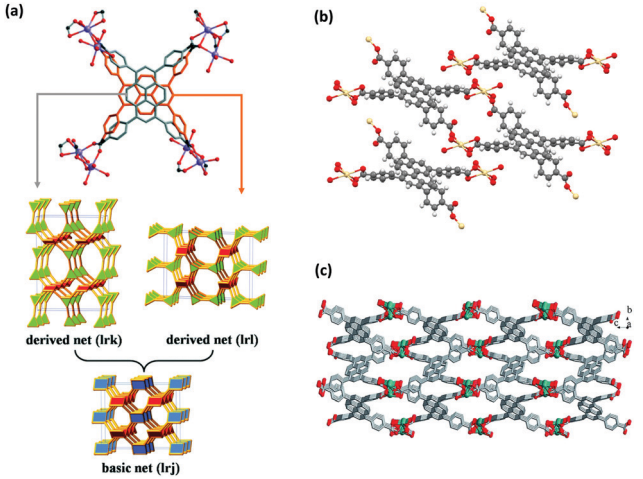

Fig. 2 (a) The 3D structure of ROD-8.[57] Although the positions of the carboxylate-O in TBAPy are crystallographically fixed, the voids allow the pyrene core with four branching phenyl groups to rattle between the two extreme positions of perpendicular orientation (demonstrated in silver and orange). Therefore, the overall 3D MOF experiences a type of framework disorder. The two positions can be regularly or randomly distributed in the framework, resulting in derived *lrk* and *lrj* nets. (b) The structural representation of 2D layers of Cd-TBAPy.[58] (c) The 3D structure of **S1**.[59] Reprinted with permission from ref. 57 and 59.

structural characteristics. It should be highlighted that not only the starting materials but also the synthesis conditions and solvents used in the synthesis of ROD-8 and Cd-TBAPy are very similar: they were both synthesized at 120 °C for 72 h using a mixture of DMF/dioxane/H_2O mixed solvent. In the case of **S1**, the conditions are slightly different: a DMF/H_2O solution was used and the synthesis was performed at 140 °C for 72 h. Nonetheless, the main difference between the three cases were the concentrations and the ratios of the metal salt and the ligand.

Another example is Zn-based pyrene-MOFs, where the syntheses have been performed with Zn-salts and TBAPy ligand. Due to the different solution environments, different Zn-TBAPy-MOFs with different characteristics have been obtained.[60–62] The structural comparisons between $[Zn(TBAPy)_{1/2}(H_2O)_2]$,[62] $[Zn_2(TBAPy)(H_2O)_2]\cdot(Guests)_x$),[60] $[Zn_2(TBAPy)]$,[60] and $[Zn_2(TBAPy)(H_2O)_2]\cdot3.5DEF$[61] showed that the use of an ionic liquid in the synthesis of $[Zn(TBAPy)_{1/2}(H_2O)_2]$ resulted in a large separation between the parallel pyrene cores, allowing intercalation of the other layers to form the highest dense packing of chromophores. It is well known that the structure and morphology of MOFs depend on not only the reactants but also many synthetic condition parameters; including solvent type, pH value of the reaction mixture, time, the molar ratio of starting materials, the presence of counterions and pressure.[63] These parameters are deterministic on the structural chemistry of ligands and the assembly process of ligands with metal centres, leading to products with diverse structures.[63] This can explain the structural variety of Cd-TBAPy and Zn-TBAPy MOFs well.

When the pyrene-based MOFs in which the metal ions with the same coordination environment are considered, the situation is even more interesting. Similar to the cases above, the reaction solvents and conditions used in the synthesis of TBAPy MOFs based on In(III),[12] Zn(II),[60] Mg(II)[68] and Zr(IV)[74] are comparable (DMF and H_2O and/or dioxane and/or HCl). Within these frameworks, all aforementioned metal ions are octahedrally coordinated; however, none of these frameworks is isostructural to each other. This is due to the formation of different forms of metal nodes (chains or clusters) as well as different orientation of TBAPy ligand around the metal atoms. This was proved by the investigation of $([Zn_2(TBAPy)(H_2O)_2]\cdot(Guests)_x)$.[60] When the axial coordinated H_2O molecule to Zn(II) was removed upon activation, the MOF has a different topology in which Zn(II) was found to be tetrahedrally coordinated. This clearly explains that the role of the central metal atom (and thus the formation of metal clusters or chains) is also important for the final topology of the framework. In addition, the orientation of the TBAPy ligand around the metal atom is dependent on the available coordination sites of the metal atom. Based on these examples, it can be deduced that the structural differences unveil the need for more dedicated studies for the exploration of the synthesis conditions of pyrene-based MOFs.

The interest in pyrene-based MOFs has tremendously increased with the synthesis of NU-1000, a zirconium-based MOF consisting of eight-connected octahedral $[Zr_6(\mu_3\text{-}O)_4(\mu_3\text{-}OH)_4(OH)_4(H_2O)_4]^{8+}$ nodes bridged by the carboxylate groups of TBAPy ligands (Fig. 3(a) and (b)).[74,111] The extended 3D structure of NU-1000 has uniform hexagonal channels with the diameter of 31 Å and triangular channels with the diameter of 10 Å (Fig. 3(c)), in addition to the smaller pores with the diameter of 8 Å separating the *ab* layers along the *c* direction (Fig. 3(d)).[111] Due to its attractive properties such as having a high Brauner–Emmett–Teller (BET) surface area (2320 $m^2\ g^{-1}$) and pore volume (1.4 $cm^3\ g^{-1}$), good thermal stability, fluorescence properties and the suitability of the structure for metalation or other types of functionalization, NU-1000 has drawn attention since its first synthesis. As a result, the chemical and structural properties of NU-1000 have been deeply studied experimentally and computationally; by exploring its synthesis conditions,[112–117] structural stability,[118,119] proton topology and surface chemistry,[120–123] and designing organic linkers for its better crystallinity.[124]

2.3 Post-synthetic modification of pyrene-based MOFs

Post-synthetic modification has been a favourable approach for tuning the physical and chemical properties of MOFs by introducing different functionalities into the structure after the framework is synthesized. Post-synthetic modifications can be performed by the modification of the linkers through covalent bond formation or cleavage, or the modification of the metal clusters by introducing the formation and/or cleavage of coordination bonds.[125] In the case of pyrene-based MOFs, the most common post-synthetic modifications are (i) the incorporation of metal ions *via* atomic layer deposition in a MOF (AIM),[126–128] (ii) solvothermal deposition in a MOF (SIM),[129] and (iii) solvent-assisted ligand incorporation (SALI).[130–132] These methods are especially attractive for the post-synthetic modification of TBAPy-based MOFs due to the presence of eight terminal (*i.e.* non-bridging) –OH groups on

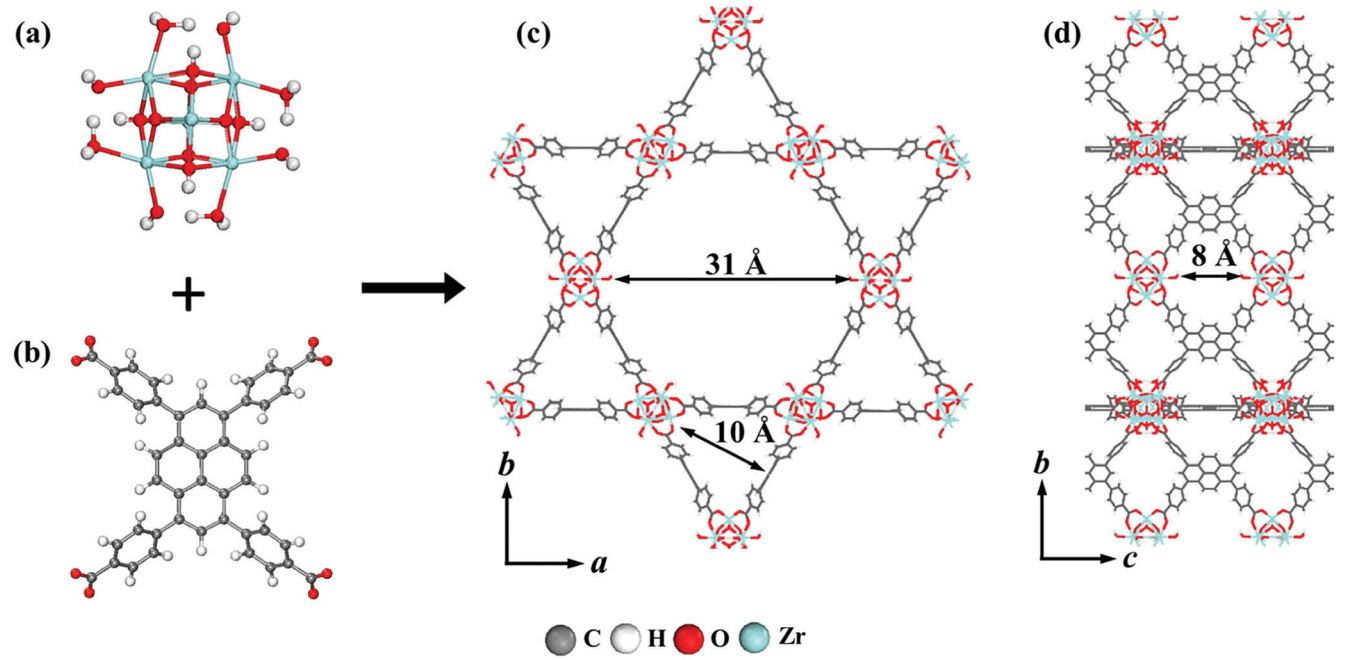

Fig. 3 The structure of NU-1000 (a) the Zr node, (b) TBAPy ligand, (c) the hexagonal and triangular channels along the *c* direction, and (d) the small pore connecting the *ab* layers along the *c* direction. Reprinted with permission from ref. 111.

the ligand, which makes the structure suitable for channel modification.

2.3.1 Atomic layer deposition in MOF (AIM) and solvothermal deposition in MOF (SIM). The incorporation of active metal sites into MOF structures has been a favorable way to introduce desired functional behavior for several applications, such as gas storage, gas separation, and catalysis. It is mostly performed in a solution environment, which can result in undesired blockage of the open metal sites by the solvent molecules. Therefore, post-synthetic metalation from the vapor-phase can be proposed as an alternative solution to eliminate purification and activation steps and inhibit open metal site blocking by solvent molecules. Atomic layer deposition (ALD) is a vapor-phase synthetic technique which allows the film growth in a cyclic manner. During each reaction, the precursor is introduced into a chamber under vacuum for a specific amount of time until it fully reacts with the substrate surface through a self-limiting process. By this way, there is no more than one monolayer forming at the substrate surface. Subsequently, the chamber is purged with an inert carrier gas (typically N_2 or Ar) to remove any unreacted precursor or reaction by-products. This step is followed by the counter-reactant precursor pulse and purge, creating up to one layer of the desired material. This process is cycled until the target film thickness is achieved.[133] These chracteristics of ALD has drawn attention by MOF researchers for the deposition of metal species on the interior pore surface of the MOFs to tune their surface chemistry. In the case of MOFs, instead of a continuous film, the product should be an array of uniformly sized and uniformly spaced node-supported clusters. The cluster size can be controlled on the basis of the number of ALD growth cycles.[134] Mondloch *et al.*[74] first applied ALD on a MOF for the post-metalation as shown in Fig. 4, which was named as ALD In a MOF (AIM) technique. AIM was developed to incorporate catalytically active metal sites, including various metal oxides, sulfides, or single metal sites, in MOFs by a site-specific and atomically controlled approach. The purpose of AIM is to prevent atom/ion migration and catalyst sintering, which are common deactivation mechanisms of support materials, especially during the catalytic applications at elevated temperatures and under a reducing environment. AIM approach inhibits the loss of catalytic activity by isolating anchored metal sites from each other using lengthy organic spacers.[135]

In a typical AIM experiment, the metal precursor is used as the first reactant while the co-reactant can differentiate depending on the desired resulting product (*e.g.* H_2O vapor can be used for the single-metal site or metal-oxide formation, whereas H_2S can be pulsed for the metal-sulfide formation). A custom-made stainless steel sample holder containing MOF powder is placed in the ALD chamber. Then, the sample is heated up to 125 °C before exposure to reagents to remove physisorbed water. After heating, the metal precursor is introduced and maintained at a temperature around 100–140 °C, where the pulses of metal precursor follows the time sequence of t_1–t_2–t_3: t_1 is the precursor pulse time, t_2 is the substrate exposure time, and t_3 is the inert gas purge time. To ensure full metalation of the metal sites of the MOF throughout the microcrystals, the metal pulsing cycle is repeated couple of times. Then, the sample is subsequently exposed to co-reactant pulses with a specific t_1–t_2–t_3 time sequence. Following the AIM, the sample is thermally activated. Although AIM is a useful method for the metalation of nodes, the MOF should have some characteristics to be considered for AIM, including relatively good stability and labile sites for replacement. Hence, AIM was first performed on NU-1000, due to its advantageous properties: (i) having mesoporous

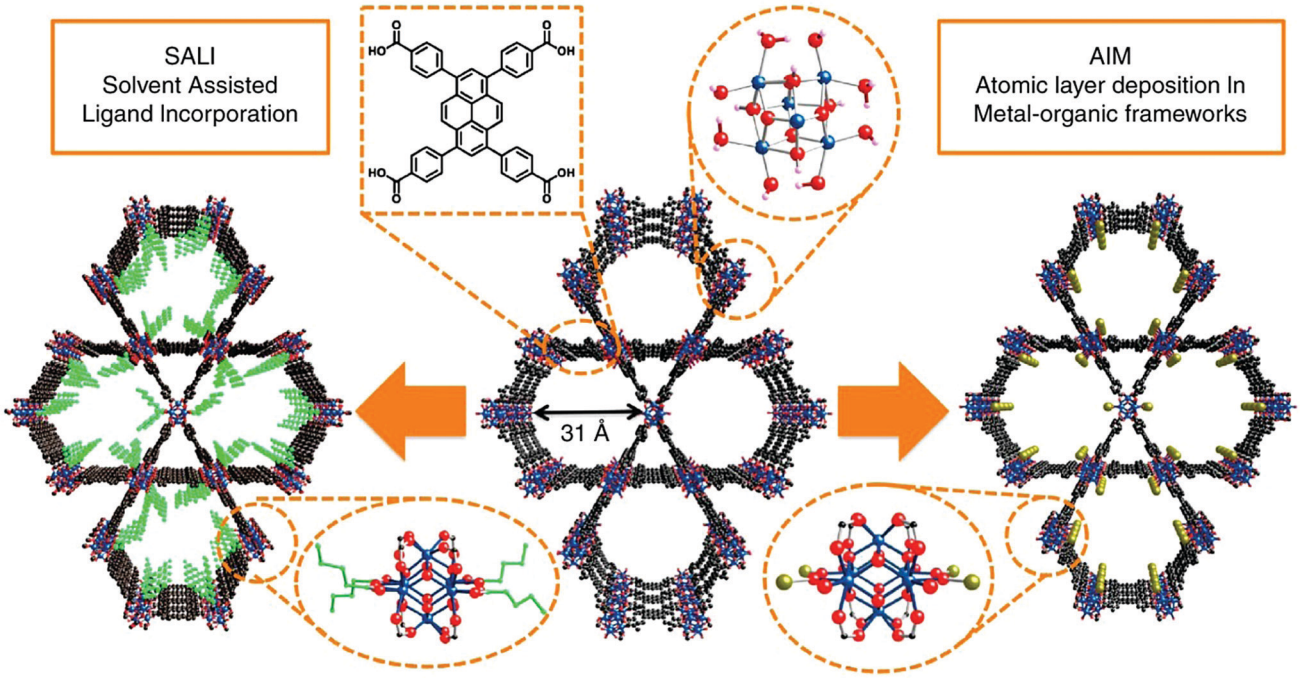

Fig. 4 Post-synthetic functionalization of NU-1000 by AIM and SALI. The ligand incorporation into NU-1000 by SALI is represented in green, and the gold sphere shows the metal cluster introduced into NU-1000 by AIM. Color code: Zr: blue; O: red; and C: black. Reprinted with permission from ref. 112.

pores to ease the diffusion of ALD reactants, (ii) having thermal and hydrolytical stability, and (iii) the presence of functional groups (–OH groups) on Zr_6 nodes to ensure the metalation. As a proof of concept, the first attempt of AIM with NU-1000 was performed with Zn and Al in an ALD reactor at 110 and 140 °C, resulting in Zn-AIM and Al-AIM successfully.[74] PXRD measurements showed the retained crystal structure after the metalation while BET measurements indicated a decrease in surface area of NU-1000 from 2320 $m^2\ g^{-1}$ to 1580 and 1160 $m^2\ g^{-1}$ for Zn-AIM and Al-AIM, respectively. The metalation of NU-1000 has been performed with different single metals and metal clusters up to date thanks to AIM.[126,136–138] Some of them were found to be very promising for different applications, mainly for catalysis, which will be discussed in Section 3. Furthermore, the bonding energetics of metal vapor adsorption onto NU-1000 for the metalation of the nodes has been investigated using different experimental techniques and density functional theory (DFT).[139]

The other common method for cluster metalation in a pyrene-based MOF is solvothermal deposition in MOF (SIM), which is complementary to gas-phase metalation of the node (AIM). In this method, the modifying metal species are dissolved in a non-reactive solvent (*e.g.* dimethylformamide (DMF), methanol or heptane) followed by soaking of the MOF into the solution.[140] In some cases, the metal precursors are only stable in air- and water-free environments, therefore the deposition is performed under inert conditions (*i.e.* in an Argon filled glovebox) by using anhydrous solvents.[141–144] The solution can be left at room temperature,[141–145] or heated at a certain temperature[129,146,147] for a specific amount of time, to provide the formation of metal species on the structure. The resulting powder is washed and then activated in a drying oven. In order to perform SIM efficiently, it is important to have a the metal source which is reactive toward –OH and H_2O functionalities on the metal node, and the structural integrity should be unaffected from the metalation to preserve the original characteristics. The metal should be soluble in the solvent; however, it should be highlighted that the formation of coordination complexes between the metal source and the solvent should be inhibited.[148] A color change can be observed in the samples, indicating the successful incorporation of metal species. As in the case of AIM, Zr-nodes of NU-1000 have been modified with different species; such as ions,[146,149] oxides,[141,142,145] sulfides,[143] and single-metal atoms[144,147] to date for different target applications.

Although both AIM and SIM are successful methods for incorporating metal species into the structure, there are some structural differences in the resulting samples, causing different performances on a specific application. In order to investigate this, Li *et al.*[149] made a study where the incorporation of Co(II) ions to the Zr_6 nodes of NU-1000 was performed *via* SIM and AIM, denoted as Co-SIM + NU-1000 and Co-AIM + NU-1000, respectively. Both catalysts were first subjected to an activation process, by heating at 230 °C with a flow of 48 mL min^{-1} O_2 (10% diluted with He) and 96 min^{-1} of C_3H_8 (3%, diluted with Ar) until the propane conversion is constant. After activation, both materials were found to be active toward the oxidative dehydrogenation of propane to propene, at reaction temperatures as low as ≈200 °C. However, catalytic activity as well as propene selectivity of these two catalysts were different under the same experimental conditions due to the differences in the Co species generated in Co-SIM + NU-1000 and Co-AIM + NU-1000 materials

upon activation, which was analyzed by *in situ* X-ray absorption spectroscopy. Upon activation with O_2, a new Co···Co interaction appeared for Co-AIM + NU-1000, which is absent in Co-SIM + NU-1000. This observation indicates that the selection of the post-modification method can be of importance depending on the target application.

2.3.2 Solvent-assisted ligand incorporation (SALI). Another common post-synthetic modification for pyrene-based MOFs is solvent assisted ligand incorporation (SALI) (Fig. 4). SALI relies on the acid–base chemistry between the aqua/hydroxo sites on the metal clusters on the MOF and the organic ligands with charge-compensating groups (*e.g.* carboxylate and phosphonate), resulting in the functionalization of the robust MOFs through a combined moiety.[130,140] SALI approach results in the introduction of functional groups as charge compensating and strongly bound moieties to the MOF node *via* ionic bonding. Ligands incorporated *via* SALI can be elaborated *via* condensation, metalation, azide click, and catalyst activation reactions.[134]

Owing to its high thermal and chemical stability as well as the presence of the terminal –OH groups on the Zr metal nodes, NU-1000 has been found promising for the functionalization with different moieties by SALI. Deria *et al.*[130] used the approach SALI with NU-1000 for the first time in the literature, by attaching perfluoroalkyl carboxylic acids of varying chain length (1, 3, 7, and 9) within the mesoporous channels of the MOF. SALI was performed by soaking NU-1000 in a concentrated solution of fluoroalkane carboxylic acid ligand in DMF at 60 °C for 18–24 h. The resultant materials were named as SALI-*n* (*e.g.*, SALI-1–SALI-9), where n is defined based on the length of the carboxylic acid ligand used in the synthesis. The N_2 adsorption isotherms and BET surface area analyses of SALI-*n* samples indicated a systematic decrease in surface area from 2320 $m^2 g^{-1}$ for NU-1000 to 1710 and 870 $m^2 g^{-1}$ for SALI-1 and SALI-9, respectively. In addition, the pore sizes and pore volumes of the samples decreased with increasing chain length of the modifying ligand. Nevertheless, CO_2 adsorption studies showed that perfluoroalkane-functionalized nodes in the SALI-*n* system increased the affinity toward CO_2, resulting in systematically higher values for *Q*st with increasing chain length. Followed by this study, different ligands have been introduced to NU-1000 by SALI and the resulting materials were found to be promising for separation, catalysis and storage.[131] Furthermore, SALI modification can be followed by AIM or SIM to deposit single metal sites on the incorporated ligand. SALI method can expand the pyrene-based MOFs in several directions by the incorporation of various types of charged anchoring moieties, multiple light harvesters or redox active moieties for the design of functional arrays or photoredox antenna systems.[151]

2.3.3 Nanocasting. The metal or cluster sites in the MOF themselves can be catalytically active for many different reactions. However, most MOFs can retain their crystallinity only up to 400 °C in air. Above these temperatures, they tend to collapse because of the decomposition of organic linkers connecting the metal sites, resulting in the aggregation of metal clusters. Hence, MOFs cannot be used for some industrially important reactions that occur only at high temperatures, such as catalytic dehydrogenation of alkane and water gas shift reactions.[150] To address this, nanocasting in MOFs has been found to be a promising templating strategy to maintain the activities of MOF-derived catalytic sites at high temperatures. In nanocasting, the MOF is heated up to a temperature where the organic linkers in MOF are eliminated. The heat treatment is applied in the presence of a secondary porous skeleton, in order to stabilize and isolate the remaining oxometal cluster sites in a thermally stable matrix. NU-1000 has been studied for nanocasting thanks to its large hexagonal channels allowing the accommodation of different precursors for a secondary porous skeleton. The precursors inside the channels of NU-1000 can be transformed into a network structure either by gelation or polymerization, followed by a thermal treatment method (*e.g.* calcination or pyrolysis) which converts the precursors to the corresponding oxide or carbon scaffolds and removes the linkers from the original NU-1000.[152] To apply nanocasting, NU-1000 was heated in static air until above its decomposition temperature (500 °C or more) in a tube furnace with a heating ramp rate of 2 °C min^{-1} and maintained at that temperature for 1 h in the presence of a secondary porous medium. By high-temperature treatment, the TBAPy linkers are removed from the structure, however the catalytic activity of Lewis acidic oxozirconium clusters in NU-1000 can be remained. Malonzo *et al.*[150] stabilized Zr cluster sites in NU-1000 by supporting them in silica, first by the preparation of a silica nanocast of NU-1000 (SiO_2@NU-1000), and then removal of the linker by calcination at different temperatures (500 to 700 °C), resulting in samples denoted as Zr_6@SiO_2 (Fig. 5). The presence of silica in the pores of NU-1000 provided the anchoring sites for the oxozirconium clusters in NU-1000, which act as Lewis acid sites. After the organic linkers were removed, catalytically active MOF-derived single-site Zr clusters were formed on silica support. The same approach has been applied with different secondary skeletons such as TiO_2, polymeric, and carbon scaffolds successfully.[152,153] The resulting structures can be promising single-site catalysts suitable for high-temperature reactions.

3 Applications of pyrene-based MOFs

3.1 Luminescence sensing

A celebrated feature of MOFs is the control of their physical properties by the selection of the organic and inorganic units. These properties include photoemission, which arises following the absorption of radiative excitation energy. The emission can take place by fluorescence (emission from a singlet excited state to the ground state) or by phosphorescence (emission from a triplet excited state to the ground state) (Fig. 6). MOFs including these emitting properties are known as ''luminescent MOFs''.[154] The origin of the luminescence in MOFs can be associated with a variety of mechanisms due to the structural diversity of MOFs.[155] This can include ligand-based emission,[66]

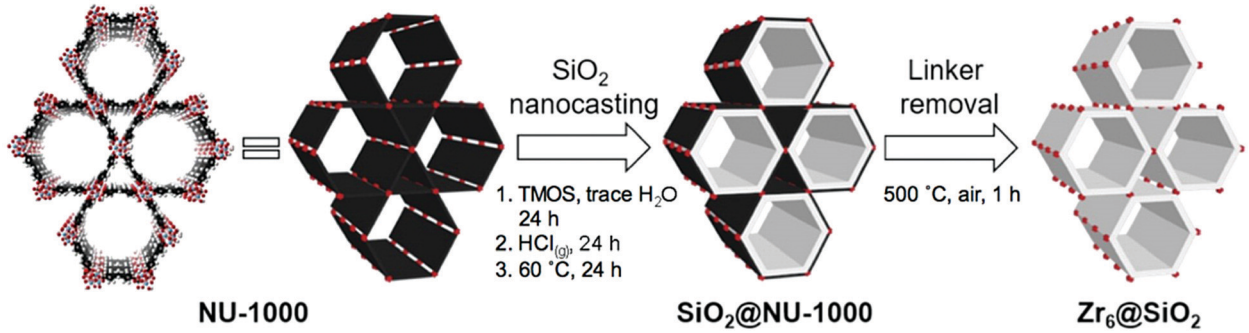

Fig. 5 The schematic representation for the nanocasting process of NU-1000 with silica. The image on the left represents the NU-1000 structure with Zr-clusters (red) and TBAPy linkers (black). The white layer in the middle image represents silica. Reprinted with permission from ref. 150.

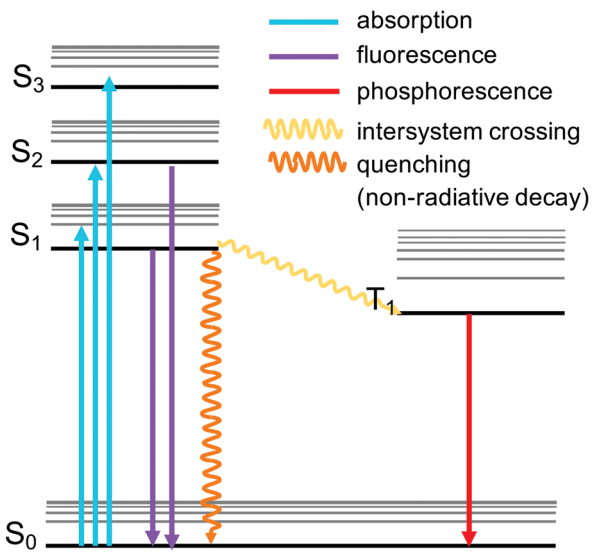

Fig. 6 Jablonski diagram of the pyrene MOFs involved in luminescence sensing.

metal-based emission,[67,89] emission due to excimer formation,[156] or guest induced emission.[155,157] Pyrene-based MOFs have been attractive for sensing applications due to the fluorescence properties of pyrene. Pyrene has a very characteristic violet emission colour when illuminated under UV light in dilute solutions, due to its monomer emission occurring between 370 and 420 nm, arising from the $\pi \rightarrow \pi^*$ transitions. Pyrene molecules can present an additional band called "excimer" emission occurring at longer wavelengths (ranging from 425 to 550 nm, centered around 460 nm) as a result of one electronically excited pyrene molecule interacting with a second one in its ground electronic state.[158] The pyrene excimer emission is an excited-state process that depends on the orientation and proximity between the two pyrene molecules, which usually tends to form strong π–π stacking.[159,160] The two main factors affecting the luminescence properties of pyrene excimers include the π–π orbital overlapping and interplanar distance.[160,161] This property can be used in porous materials containing pyrene to develop sensors for the detection of guest molecules such as gases, organic molecules, and metals, when pyrenes are localised in the structure (Table 2). Since pyrene is a florescent probe whose spectrum is responsive to the polarity of its environment, different environmental parameters can be also detected by utilizing the excimer fluorescence of pyrene. In addition, pyrene molecules can also exhibit excimer emission and emission from higher excited states.[162] Stylianou *et al.*[12] reported the increase of the lifetime emission of a coordinated pyrene indium MOF (In-TBAPy), compared to the isolated pyrene molecules. Likewise, the emission wavelength, lifetime, and intensity of In-TBAPy can be tuned with the selection of guest species and loadings. The structure and chemical nature of guest molecules have a direct influence on the luminescence properties of pyrene-based MOFs.[99,101,106,163] Moon *et al.*[164] used SALI to incorporate 5(6)-carboxynaphthofluorescein (CNF) within NU-1000 to modify the optical properties of the material. The new MOF, NU-1000-CNF, displayed visually colorimetric pH sensing ability, where it has reversible colour change when exposed to solutions or vapors of varying pH.[164] Such optical response diversity and sensitivity in pyrene-MOFs with luminescence have placed them as potential luminescent probe materials, due to the fact that they can serve as sensory systems of analytes that are bound to the MOFs by virtue of their porosity.[109]

Table 2 shows different applications of pyrene-based MOFs in luminescence sensing applications. One of the applications is the sensing of nitro-aromatic explosive molecules. This application exploits the π-donor nature of the pyrene linkers with the electron-deficient nature of nitroaromatics, in order to sense the analytes *via* fluorescence quenching mechanism. Bajpai *et al.*[106] synthesized the Mn-L MOF for nitroaromatic explosives sensing. Mn-L displayed a gradual decrease in fluorescence intensity upon increasing the concentration of nitroaromatic molecules. Thus, the photoexcited MOF electrons located in the conduction band of Mn-L interact with the LUMO of the analytes *via* charge transfer, leading to the diminution of the fluorescence. Different nitroaromatic explosives displaced a linear relationship of the Stern–Volmer curve, yet 2,4,6-trinitrotoluene (TNT) presented higher value of Stern–Volmer quenching constant along with higher quenching efficiency (74%). Similarly, other MOFs have been exploiting this charge-transfer interaction displaying selective sensitivity for explosives like nitrobenzene,[99,109] 2,4,6-trinitrophenol,[163] and 2,4,6-trinitrotoluene.[165]

Table 2 Luminescent sensing applications of pyrene-based MOFs

Application	Analyte	MOF name	Mechanism	Excitation (nm)	Ref.
Explosives	2,4,6-Trinitrotoluene (TNT)	Mn-L	Quenching fluorescence	330	106
	Nitrobenzene (NB)	LMOF-1	Quenching fluorescence	370	109
	Nitrobenzene (NB)	MgMOF	Quenching fluorescence	300	99
	2,4,6-Trinitrophenol (TNP)	Pyrene-tagged UiO-66-NH_2	Quenching fluorescence	360	163
	2,4,6-Trinitrotoluene (TNT)	UiO-66-Py	Quenching fluorescence	365	165
Gas and toxic molecules	H_2S	$Zr(TBAPy)_5(TCPP)$	Turn-on fluorescence	365	168
	O_2	Yb^{III}-TBAPy	Quenching fluorescence	355	89
	Acetone	Bio-MOF Zn-MOF (1)	Quenching fluorescence	280	94
	$Cr_2O_7^{2-}$	NU-1000	Quenching fluorescence	400	170
Ions	Cu^{2+}	CPP-16	Quenching fluorescence	335	156
	OH^-	JUC-119	Stokes shift luminescence	300	101
	Cu^{2+}	MIL-53-L	Quenching fluorescence	337	171
	Hg^{2+}	SALI-MAA-3eq MOF	Quenching fluorescence	365	172
Biomolecules	Histidine	Zn-PLA	Quenching fluorescence	355	103
	1-Hydroxypyrene	NU-1000	Quenching fluorescence	360	173
	Uric acid	Hf-UiO-66-Py	Quenching fluorescence	340	166
	Cholesterol	Rh6G@NU-1000-CMCD	Turn-on fluorescence	470	167
	Biothiols	Bi-TBAPy	Turn-on fluorescence	396	87
Temperature	100–300 K	$\{[Cd(TBAPy)(H_2O)_2]\cdot 4(H_2O)\}_n$(1)	Temperature-dependent emission	355	59
	80–450 K	SION-7	Temperature-dependent emission	405	83
	293–460 K	$Zn(TBAPy)_{1/2}(H_2O)_2$	Temperature-dependent emission	315	62
	20–440 K	$M_2(TBAPy)(H_2O)_2$ [M = Co, Zn]	Temperature-dependent emission	420	95
Polycyclic Aromatic Hydrocarbons	Acenaphthylene	NU-1000	Quenching fluorescence	395	174
	Pyrene	NU-1000	Excimer fluorescence	395	174
	Fluoranthene	NU-1000	Exciplex fluorescence	395	174
pH	pH 1–10	NU-1000-CNF	Colorimetric		164

The quenching fluorescence mechanism can also be translated to applications involving analytes with different chemistry. The design of interacting sites, the chemistry of the analyte, and the cavities of MOFs play a role in the selective sensing. Huang *et al.*[94] successfully synthesized an anionic MOF featuring a combination of mononuclear and tetranuclear zinc clusters and a mix-and-match strategy of two different types of organic ligands (TBAPy and 6-benzylaminopurine). This MOF exhibited exclusive luminescence quenching effect by acetone as a result of the formation of small cavities, leading to the binding of acetone by multiple hydrogen bonds with the MOF. Another example of the rational design for sensing application exploiting fluorescence quenching is sensitivity to chiral analytes. Chandrasekhar *et al.*[103] developed a Zn-MOF (Zn-PLA) based on a pyrene-tetralactic acid linker, which can selectively sense histidine *via* fluorescing quenching. The nature of the chiral organic linkers in Zn-PLA imparted by the lactic acid moieties allowed the specific discrimination of histidine among all other amino acids, and the enantiodiscrimination of the D and L forms of histidine. Like the above, different rational design of pyrene-based MOFs has been applied for sensing applications exploiting quenching fluorescence of different molecules, like bio-molecules, ions, and gas and toxic molecules (Table 2).

Although in most cases the selectivity comes from the combination of the metal cluster and linker properties of the MOF itself, some cases require the use of post-synthetic modifications. This is the case of applications where require the inclusion of pyrene moieties in Zr-based MOFs,[156,166] or the inclusion of polymers. Gong *et al.*[167] designed a MOF where carboxymethyl β-cyclodextrin (β-CMCD) was grafted onto the NU-1000 MOF (NU-1000-CMCD) as an energy transfer bridge and to capture cholesterol recognition. Unlike the previous cases, the sensing mechanism in NU-1000-CMCD is a turn-on fluorescence. Fig. 7 shows a schematic of the structural and dimensional parameters of NU-1000-CMCD. The β-CMCD acts as a host–guest recognition for rhodamine 6G (Rh6G) or cholesterol; if Rh6G is attached to β-CMCD the luminescence is quenched due to the fluorescent resonance energy transfer (FRET) while the cholesterol induces the fluorescence restoration of the pyrene ligand. NU-1000 can also be used as a fluorescence turn-on probe for selectively and sensitively detecting H_2S and its derivatives S^{2-}, if tetrakis(4-carboxyphenyl)porphyrin (TCPP) is installed as linker *via* the solvothermal method.[168] The installation of TCPP in NU-1000 causes the natural quenching fluorescence of the pyrene ligands, as a result of TCPP–TBAPy interaction. The fluorescence is restored in $Zr(TBAPy)_5(TCPP)$ due to N–S bond formation of S^{2-} with N atoms in the porphyrin moiety. This suggests the role of N atoms in the porphyrin for the detection of H_2S derivatives S^{2-} in aqueous solutions. The tunability of MOFs allows a plethora of applications for smart design involving fluorescence and photophysical mechanisms.

The luminescence in pyrene-based MOFs can also be exploited for other applications such as temperature sensing.

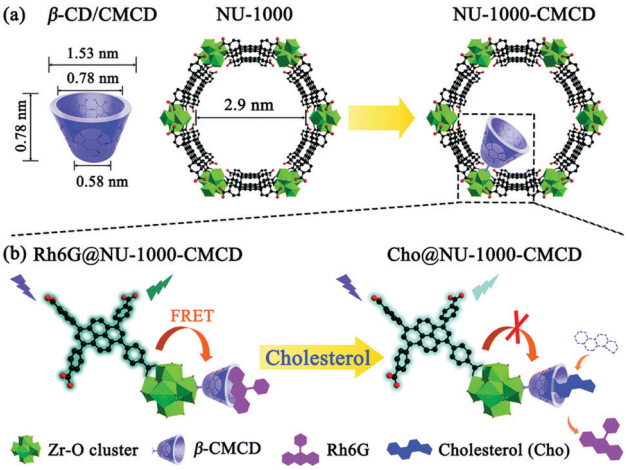

Fig. 7 (a) Structural and dimensional parameters of β-CD/CMCD and NU-1000 as well as NU-1000-CMCD. (b) Schematic illustration of the proposed sensing mechanism for cholesterol detection with β-CMCD as the recognition sites using a Rh6G@NU-1000-CMCD probe. Reprinted with permission from ref. 167.

Materials exhibiting tunable fluorescence emission upon heating or cooling are considered smart materials as their optical properties can be exquisitely controlled by adjusting the external temperature.[83] It is known that the pyrene-based MOF topology plays an important role in the interchromophoric interactions behavior of the excited stated,[169] yet the temperature is also an important factor. Gładysiak *et al.*[83] reported a pyrene-based MOF, SION-7, which can display either monomer or excimer fluorescence emission due to the temperature-dependent extent of interchromophoric interactions between the $TBAPy_3$-ligands within the framework. The same phenomena has been also reported in Cd, Co, and Zn TBAPy-based MOFs where the temperature is a key parameter in the interchromophoric interactions.[59,95] These materials display a linearly decreasing emission intensity dependence to the increase of temperature in the ranges of 100 to 300 K ($\{[Cd(TBAPy)(H_2O)_2]\cdot 4(H_2O)\}_n$) and 100 to 400 K ($M_2(TBAPy)(H_2O)_2$ [M = Co, Zn]). Zeng *et al.*[59] reported a relative thermal sensitivity of 0.319 K^{-1} with a maximum value of 0.32 K^{-1} at 300 K for $\{[Cd(TBAPy)(H_2O)_2]\cdot 4(H_2O)\}_n$, these values were comparable to those of the lanthanide coordination polymers. The emission intensities in these pyrene-based MOFs increase at lower temperatures since intramolecular rotations and non-radiative relaxations processes are restricted.[59] On the contrary, higher temperatures will promote more electron transitions by thermal energy activation within the excited states with varying vibrational levels hence more non-radiative decays process can occur.[83] Likewise, the MOF topology and porosity can directly lead to changes in the photophysical properties. The formation of pyrene excimers as a result of the MOF topology can be regulated by temperature-dependent spacing change or be hindered by solvent molecules interactions.[83]

3.2 Photocatalysis

Photocatalysis is a type of catalysis involving the acceleration of a photoreaction by adding substances (catalysts) that participate in the chemical reaction without being consumed. Photocatalysis, while varying in details in terms of reactions and mechanisms, can be described by four steps: (i) light absorption to generate electron-hole pairs carriers; (ii) separation of excited charge carriers; (iii) transfer of electrons and holes to the photocatalyst; and (iv) utilization of charge carriers for redox reactions.[175] The organic chromophore energy transfer mediator and light harvesting properties of pyrene have been exploited in the design of heterogeneous photocatalyst. Table 3 shows the main applications in the field of photocatalysis using pyrene-based MOFs. MOFs have shown to be excellent candidates for the sorption and degradation of chemical warfare agents thanks to their porous and tunable nature.[176] A recurrent use of pyrene-based MOFs is the sulfur mustard degradation. Omar K. Farha and Joseph T. Hupp have pioneered the field with the application of NU-1000 for the selective oxidation of 2-chloroethyl ethyl sulfide (CEES) *via* singlet oxygen ($^1O_2$) generation without producing the toxic sulfone.[176] This approach exploits the use of pyrene-based

Table 3 Photocatalytic pyrene-based MOFs

MOF Name	Photocatalysis	Co-Catalyst	Ref.
NU-1000	Sulfur mustard degradation	—	176 and 192
NiS-AIM	HER	—	184
JUC-138	Azure B photodegradation	—	102
Br-BDP@NU-1000	Sulfur mustard degradation	—	179
NU-1000-PCBA	Sulfur mustard degradation	—	180
CdS@NU-1000	HER	CdS	189
NU-1000	Photocatalytic atom-transfer radical addition		181
Cd-TBAPy	Water reduction and oxidation	Pt and CoPi	190
MoS_x-SIM	HER	—	193
Bi-TBAPy	HER	Pt	191
PPIX@NU-1000	Sulfur mustard degradation	—	194
$FeSC_{12}$-AIM	Nitrate reduction	—	182
ACM-1	HER	Pt	97
NU-400	Sulfur mustard degradation	—	65
PCN-822(Hf)	Amine oxidation	—	110
NU-1000	4-Methoxybenzyl alcohol oxidation	—	146
NU-1000-U	4-Methoxybenzyl alcohol oxidation	—	146
FDH@Rh-NU-1006	CO_2 reduction	NAD enzyme	183

linkers as UV photosensitizers in order to absorb light and generate an excited singlet state. This singlet can later be transformed into a triplet state *via* singlet to triplet inter-system crossing.[177,178] Energy transfer processes can take place from the pyrene triplet state to ground state triplet oxygen, thereby yielding singlet oxygen. The 3D crystal structure of MOFs provides a platform to heterogenized and isolated pyrene moieties in an ordered array, which can enhance the efficiency of singlet oxygen generation by preventing aggregation and photo-degradation.[176] NU-1000 inherits the photophysical properties of pyrene and under UV LED irradiation, 0.2 mmol CEES can be completely and selectively oxidized to CEESO within 15 min using 1 mol% of NU-1000 (2.16 mg, 2 μmol by pyrene unit).[176] When compared with 1.35 mg (2 μmol, 1 mol%) of the isolated linker, TBAPy, the complete conversion occurs after 30 min confirmed by gas chromatography and the selectivity of the photo oxidation reaction was corroborated by NMR experiments. The half-time of the NU-1000 MOF is 6.2 min while the half-time of the linker (TBAPy) is 10.5 min for complete conversion of CEES. The improved rate of reaction was associated with the rigid framework of pyrene linkers in NU-1000 preventing deactivation by aggregation.

Zr_6 node topology of NU-1000 can offer a platform to tune the photophysical and photochemical properties of the MOF *via* post-synthetic modifications.[121] Atilgan *et al.*[179] incorporated the BODIPY chromophore onto the Zr_6 metal node of NU-1000 *via* SALI. The resulting MOF named Br-BDP@NU-1000 (0.2 mol%, 0.4 μmol) presented approximately a half-time of 2 min for 0.2 mmol CEES complete photo-oxidation into CEESO, which is much faster than that of NU-1000. Importantly, the incorporation of BODIPY molecules allowed the material to display CEES photocatalytic activity under green LED irradiation, in contrast the UV LED sourced is needed for NU-1000. The post-synthetic modification of Zr_6 node has been a recurrent strategy to tune the singlet oxygen production including photosensitizers like fullerene[180] and porphyrin.[80] Other pyrene-based MOFs have also been used for photodegradation of pollutants as in the case of Azure B photodegradation in JUC-138.[102] A different mechanism of organic transformation was reported by Zhang *et al.*,[181] where the photocatalytic atom-transfer radical addition (ATRA) of perfluoroalkyl iodides onto olefins occurs in NU-1000. They showed that NU-1000 photochemically generates the reactive radical species by sensitisation of the perfluoroalkyl iodides through a photoinduced energy-transfer pathway. Importantly, the authors reported the importance of the visible-light source where the best performance (93% isolated yield) was obtained with a LED with a center wavelength of 405 nm, using 2.5 mol% of NU-1000 which is rationalized by the strong absorption of NU-1000 at 405 nm. NU-1000 has also been used for other organic transformations, such as a nitrate reduction photocatalyst by iron thiolate cluster incorporation into Zr_6 node of the NU-1000 MOF.[182] Choi *et al.*[182] showed how this new MOF (named as $FeSC_{12}$-AIM) in an aqueous solution containing nitrate (30 ppm of N, calculated by nitrogen mass) and ascorbic acid as a sacrificial electron donor, can photochemically transform NO^{3-} to NH^{4+} as a result of the photoexcitation of the pyrene linker to the iron thiolated cluster. In general, pyrene-based MOFs can be used for photocatalytic organic transformation reactions involving singlet oxygen or photoinduced energy transfer reactions.

The photo-sensitizing properties of pyrene-based MOFs have also been exploited in promising energy applications like photocatalytic CO_2 reduction[183] and H_2 production.[184] Theoretical and experimental studies have shown key features of photocatalytic systems like absorption,[185] charge transfer,[186,187] and charge-separation[187,188] present in pyrene-based MOFs. Inspired by natural photosynthesis, Chen *et al.*[183] encapsulated formate dehydrogenase (FDH) in a Zr pyrene-based MOF, NU-1006, anchored with Rh-based electron mediator in order to couple co-enzyme regeneration with enzymatic CO_2 reduction for efficient CO_2 fixation system. The material FHD@Rh-NU-1006 facilitates ultrafast photoinduced electron transfer, leading to CO_2 reduction to formic acid when combined with the co-enzyme, nicotinamide adenine dinucleotide (NAD). Other energy-related photo-catalytic applications with pyrene-based MOFs have focused on the synthesis of materials for hydrogen evolution reaction (HER) (Table 3). Peters *et al.*[184] reported the anchoring of NiS_x in NU-1000 *via* AIM, where the new material NiS-AIM can catalytically produce H_2 upon light illumination. The pyrene-based linkers act as a UV photosensitizer and the nickel sulfide-functionalized node catalyzes the reduction of water to generate hydrogen gas with a rate of 3.1 mmol g^{-1} h^{-1} under UV light (LED, maximum 390 nm). The visible light absorption profile of NiS-AIM was improved by the use of rose bengal dye as a photosensitizer. The porous nature of the MOF allows the diffusion of the dye, leading to an improvement in the light-absorption (at 550 nm) and enhancement in the H_2 production (4.8 mmol g^{-1} h^{-1}) upon visible light irradiation.[184] Another approach to improve NU-1000 HER photocatalysis was the dual modification by the incorporation of CdS nanaparticles (as a co-catalyst) along with reduced graphene oxide (RGO).[189] The addition of RGO led to more efficient charge separation and further accelerated the transfer of photogenerated electrons, than in the case where RGO is not considered. The material, CdS@NU-1000/1%RGO, presented a 12.1 times higher H_2 generation rate than that of commercial CdS under visible light. Remarkably, CdS@NU-1000/1%RGO displayed a significantly enhanced photostability compared to CdS.

Although the tunability of the optical properties of NU-1000 has been explored, there are other TBAPy-based MOFs with HER photocatalytic activity. TBAPy linkers have been combined with metal clusters such as Cd, Bi, and Ti which have led to materials with compelling HER properties. The cadmium MOF (Cd-TBAPy) is a 2D layer material exhibiting visible-light absorption around 600 nm and dual functions of water reduction and oxidation when combined with Pt and CoPi co-catalyst, respectively.[190] After loading suitable co-catalysts, the hydrogen and oxygen evolution rate can reach up to 4.3 and 81.7 μmol h^{-1}, respectively. In this case, the proper combination of TBAPy and the transition metal can lead to materials exhibiting better visible light absorption than pyrene itself. The bismuth (Bi-TBAPy)[191] and titanium (ACM-1)[97] MOFs are other

examples of pyrene-based MOFs with good HER when combined with co-catalyst. Both MOFs exhibit a typical ligand-to-metal charge transfer (LMCT) leading to intrinsic charge separation confirmed by XPS spectra and DFT calculations. Bi-TBAPy and ACM-1 optimal H_2 production rates are 140 μmol g^{-1} h^{-1} and 67 μmol h^{-1}, respectively, when combined with Pt nanoparticles. It is noteworthy to mention that ACM-1, unlike Bi-TBAPy, can present a reduced HER (5.9 μmol h^{-1}) without the presence of co-catalyst. The 1D titanium rod metal cluster in ACM-1 leads to position the Ti–O orbitals at the conduction band of the material, resulting in an efficient electron transfer from the organic ligand.[97] Despite the number of pyrene-based MOFs for photocatalytic applications is still small, the unmatched control over MOF photophysical properties have led to materials suitable for different application including the synergy of pyrene linkers with different metal clusters.

3.3 Adsorption and separation of molecules

MOFs have been widely studied for adsorption and separation applications due to their geometrically and crystallographically well-defined framework structures with high permanent porosity, large surface area, and remarkable thermal and mechanical stability. MOFs can be designed for desired separation and capture processes by tuning the microporous channels and introducing functional groups. There are several pyrene-based MOFs in the literature that have been investigated for adsorption and separation owing to different reasons, such as (i) preferential binding sites on the carboxylates and aromatic rings on the linker,[90,195] (ii) permanent porosity and framework stability in the presence of water,[78] (iii) suitable pyrene-pyrene distance for the adsorption and separation of gas molecules,[57,77,85] (iv) the presence of rotatable units connected to pyrene ligand, resulting in enhanced loading of the guest molecules in the structure,[60] (v) donor–acceptor interaction between the adsorbate molecule and pyrene,[91] and (vi) the possibility of using functional groups within the MOF as structure-directing agents.[84] In this section, we will discuss pyrene-based MOFs that have been investigated for adsorption and separation of different molecules and Table 4 will be summarizing all the performances.

3.3.1 Energy related gases. The synthesis of materials for selective gas adsorption or separation processes must take into account the physical properties (*e.g.* polarizability and quadrupole moment) and the host–guest interactions between the gas molecules and the adsorbent material. Therefore, the design of the organic ligand and selection of the metal ion are important when constructing a MOF structure for the selective capture of energetically important gases, such as carbon dioxide (CO_2), methane (CH_4), nitrogen N_2, or hydrogen (H_2). For example, the incorporation of large, planar, aromatic or methyl-substituted ligands can result in the formation of a pore size adjusted to the kinetic diameter of CH_4, resulting in increased uptake capacity of MOFs.[57] Pyrene-based MOFs are good candidates for gas adsorption and separation applications due to the rigid nature of the pyrene-based ligands, which results in well-adjusted pore size for specific gas molecules as well as structural robustness and stability. In a pyrene-based MOF, while having a large surface area and pore volume is important for the storage of gases such as CH_4 and H_2, the interaction of the gas molecule with the framework is more prominent for the separation of CO_2. With the synthesis of new and robust tetracarboxylate-pyrene ligands, the number of structures has started to rise incrementally.

Pyrene-based MOFs can have different structural characteristics based on the size of pyrene ligand, or its stacking in the framework, resulting in different gas adsorption performances.[68,73] UTSA-72 is a 2D microporous paddle-wheel MOF which was constructed from $Zn_2(COO)_4$ clusters connected by PTTB linkers.[73] Due to the presence of two kinds of cavities of 2.9 × 2.9 $Å^2$ and 2.4 × 4.6 $Å^2$, UTSA-72 was investigated toward the separation of CO_2 from CH_4 and N_2. The higher adsorption capacity of CO_2 than those of CH_4 and N_2 resulted in moderately high CO_2/N_2 (33.4) and CO_2/CH_4 (7.2) selectivity. Another pyrene-based MOF, NU-1100 was synthesized based on $Zr_6O_4(OH)_4^{12+}$ clusters and a pyrene-based tetratopic ligand PTBA,[105] which is a much bigger ligand in size compared to PTTB. This is due to the presence of ethynyl groups in between the pyrene core and benzoic acids. Consequently, the CH_4 gravimetric deliverable capacity of NU-1100 has been found significantly higher (0.24 g g^{-1}) than most promising CH_4-storage materials such as HKUST-1 (0.154 g g^{-1}), PCN-14 (0.136 g g^{-1}), and UTSA-20 (0.134 g g^{-1}). These studies were followed by other TBAPy-MOFs with rod SBUs including Mn(II), In(III) and Cd(II) metals (denoted as ROD-6,[196] ROD-7,[12] and ROD-8,[57] respectively). Although its lower surface area, the CO_2 uptake capacity of ROD-6 (7.73 wt%) surpasses that of ROD-7 (6.70 wt%) and is comparable to that of ROD-8 (7.90 wt%) at ambient conditions. This can be explained by the stronger interactions between the CO_2 molecules and the framework, resulting in a slightly increasing isosteric heat of adsorption (20–21 kJ mol^{-1})[77] ROD-8 was further investigated toward CH_4 adsorption, due to two main reasons: (i) the nearest pyrene-pyrene distance (4.35 Å) fits well to the CH_4 kinetic diameter of *ca.* 3.8 Å, and (ii) the isosteric heat of adsorption is close to the calculated optimal value of 18.8 kJ mol^{-1} for CH_4 adsorbents. As a result, CH_4 uptake in ROD-8 was obtained as 0.77 wt% at 298 K and 1 bar, which outperforms some of the reported MOFs to date.

Besides structural characteristics, it is well known that the presence of open-metal sites favors the adsorption of specific gases, such as CO_2.[76] Pyrene-based MOFs can be synthesized as to have open metal sites in the structure, based on the design of the ligand. A Co-based pyrene MOF constructed from 1,3,6,8-tetra(3,5-dicarboxyphenyl)pyrene (tdcppy) ligand was found to have additional cobalt sites in the structure, which are acting as open metal sites (Fig. 8).[100] Single-crystal X-ray diffraction analysis showed that while six carboxylate groups on the pyrene participate in composing the cobalt trigonal prismatic SBUs, the other two carboxylate groups bridge cobalt sites dangled on cobalt trigonal prismatic clusters, providing open metal sites for CO_2 uptake. In addition, anionic MOFs can be constructed using pyrene-based ligands, such as PTCA.[69–71] It was found out

Table 4 Pyrene-based MOFs for the adsorption and separation of different molecules

MOF name	Molecules	Adsorption performance	Ref
Energy-related gases			
Ni-TBAPy	CO_2 and CH_4 (@298 K, 1 bar)	15 and 10 $cm^3\ g^{-1}$	76
ROD-6	CO_2 and N_2 (@298 K, 1 bar)	39.36 and 3 $cm^3\ g^{-1}$	196
ROD-7	CO_2 and N_2 (@298 K, 1 bar)	34.09 and 2 $cm^3\ g^{-1}$	12 and 196
ROD-8	CO_2, CH_4 and N_2 (@298 K, 1 bar)	40.21, 17.16 and 2.5 $cm^3\ g^{-1}$	57
NU-1100	CO_2 (@298 K, 30 bar), CH_4 and H_2 (@298 K, 65 bar)	26.2, 16.8 and 6 mmol g^{-1}	105
UTSA-72	CO_2, CH_4 and N_2 (@296 K, 1 bar)	21.7, 4.4 and 1.1 $cm^3\ g^{-1}$	73
Mg-PTCA	CO_2 (@195 K, 1 bar), H_2 (@77 K, 1 bar), and O_2 (@77 K, 0.19 bar)	160.5, 92.2 and 200.1 $cm^3\ g^{-1}$	68
Co-tdcppy	CO_2 (@298 K, 1 bar)	61.6 $cm^3\ g^{-1}$	100
ZnLi-PTCA	CO_2, CH_4 and N_2 (@298 K, 1 bar)	60.9, 15.9 and 3.6 $cm^3\ g^{-1}$	70
Cd-PTC	CO_2 and CH_4 (@298 K, 1 bar)	58 and 7 $cm^3\ g^{-1}$	71
Ni-PTCA	CO_2, CH_4 and N_2 (@298 K, 1 bar)	65, 20 and 5 $cm^3\ g^{-1}$	69
NU-1000-SALI-9	CO_2 (@273 K, 0.15 bar)	6.2 $cm^3\ cm^{-3}$	130
NU-901-SALI-BA-3,5-NH_2	CO_2 (@273 K, 1 bar)	123 $cm^3\ g^{-1}$	199
PEI(50)@NU-1000	CO_2 and N_2 (@298 K, 0.15 bar)	1.06 and 0.0073 mmol g^{-1}	200
NU-505-Zn	N_2 (@77 K, 1 bar)	400 $cm^3\ g^{-1}$	78
Al-PyrMOF	CO_2 and N_2 (@313 K, 1 bar)	2.29 and 0.2 mmol g^{-1}	85
Organic and inorganic pollutants			
NU-1000	(SeO_3^{2-}) and (SeO_4^{2-})	102 and 62 mg g^{-1} in <1 min	204
NU-1000	Sb(III) and Sb(V)	136.97 and 287.88 mg g^{-1} in 10 h	203 and 205
NU-1000	($Cr_2O_2^{7-}$)	76.8 mg g^{-1} in 3 min	206
NU-1000	Atrazine	36 mg g^{-1} in <1 min	207
NU-1000	Glyphosate	8.97 mg g^{-1} in 3 min	208
NU-1000	(ReO_4^-)	210 mg g^{-1} in 5 min	209
NU-1000	2-CEES and DMMP	4.197 and 1.70 mmol g^{-1}	210
NU-1300	Proteins: Cyt-*c* and a-La	90 and 6% of Cyt-*c* and a-La in 20 h	79
UOF-1 and UOF-2	Cs^+	108 mg and 96 mg g^{-1} in 60 min	81
SION-82	VOCs	107 mg g^{-1} in equilibrium	98
Hydrocarbons			
Zn-TBAPy	mX and pX (@303 K, 15 bar)	3.36 and 2.11 mmol g^{-1}	60
NU-1105	Propane (@273 K, 40 bar)	700 $cm^3\ g^{-1}$	108
JXNU-5	Acetylene (C_2H_2) (@298 K, 1 bar)	55.9 $cm^3\ g^{-1}$	90
bioMOF 1-NH_2	C_2H_2, C_2H_4 and C_2H_6 (@298 K, 1 bar)	55.6, 52.4 and 51 $cm^3\ g^{-1}$	93
NU-1000	R134-a	17 mmol g^{-1}	214
NU-1000	Propane (@273 K) and isobutane (@298 K)	0.49 and 0.76 g g^{-1}	216
Carbohydrates and carbohydrate-derived aromatics			
IL/NU-1000	Coumaric and ferulic acids	66 and 72 mg g^{-1} in [Ch][Lys], and 70 and 95 mg g^{-1} in [EOA][OAc]	220
NU-1000	Phenolics (4-hydroxybenzaldehyde, 4-hydroxybenzoic acid, vanillin, vanillic acid, syringaldehyde, and syringic acid)	354, 325, 371, 391, 340, and 373 mg g^{-1}, respectively	218
NU-1000	HMF and furfural	240 and 467 mg g^{-1}	219
NU-1000	Cellobiose and maltose	1260 and 1383 mg g^{-1}	221
Radioactive gases			
NU-1106	Xe and Kr (@298 K, 1 bar)	38 and 16 $cm^3\ g^{-1}$	72
SION-8	I_2	340 mg g^{-1} in 200 h	91
NU-1000	I_2	1.45 g g^{-1} in 60 h	224

that the cations arising from the decomposition of the solvent molecule used in the synthesis act as the counter ions in the pores and favor the separation of CO_2 from CH_4 and N_2.

The presence of water in flue gas stream is an important problem for industrial settings for the capture of CO_2. Therefore, the selection of metal and ligand is highly important for the design of robust structures upon water exposure.[78,105] It is important to expand the understanding of the interaction of water with the pyrene-based MOF structures to rationally design feasible structures. Very recently, a detailed computational and experimental study was performed by Boyd *et al.*[85] to understand the effect of having an ''adsorbaphore'' in the MOF structure for CO_2 separation in industrial conditions. Adsorbaphore term was introduced to specify the common pore shape and chemistry of a binding site in a MOF that provides optimal interactions to preferentially bind to a particular guest molecule. A library of 325 000 hypothetical MOFs was generated and each MOF was screened to investigate its CO_2/N_2 selectivity and CO_2 working capacity. It was identified that the presence of two parallel pyrene and porphyrin rings (''adsorbaphores'') with

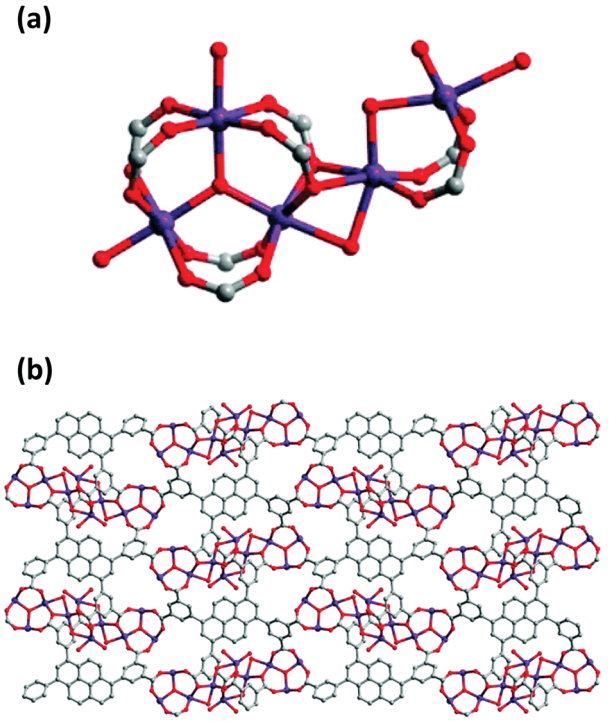

Fig. 8 (a) Open metal sites dangled on the cobalt trigonal prismatic SBU of the Co-based pyrene MOF, Co-tdcppy. Atom colour code: purple, Co; grey, C; red, O. (b) The structure of Co-based pyrene MOF viewed along the b direction. Modified and reprinted with permission from ref. 100.

interatomic spacings of approximately 7 Å favors the binding of CO_2, while excluding the presence of water molecules due to their low Henry coefficient. Based on these findings, a porphyrin-based MOF (Al-PMOF) and a pyrene-based MOF (Al-PyrMOF) were synthesized with tetrakis(4-carboxyphenyl) porphyrin (TCPP) and TBAPy ligands, which are coordinated to one-dimensional Al(III)-oxygen rods. (Fig. 9(a)). Al is an attractive choice as the metal due to being less costly and earth-abundant compared to other well-investigated metals, and it ensures a strong bond with the carboxylate O-atoms of the ligands resulting in enhancing the thermal and hydrolytic stability of a MOF. Both experiments and calculations proved that while the stacked rings of porphyrin and pyrene are preferential adsorption sites for CO_2 molecules, water molecules do not prefer to bind in between them. Moreover, the affinity of the MOF toward CO_2 is higher than that of N_2, resulting in good separation of CO_2/N_2 mixtures (Fig. 9(b)). Thanks to its highly stable framework in the presence of water, Al-PyrMOF showed a remarkable CO_2 working capacity in a humid environment compared to those of other commercially available materials (zeolite 13× and activated carbon) and well-studied water-stable MOF (UiO-66-NH_2) (Fig. 9(c)).

NU-1000 has been a well-investigated member of pyrene-based MOFs because of its high chemical and mechanical stability, which arises from the strong ionic bonding between Zr and carboxylate oxygen atoms. It has large surface area which can lead to high gas adsorption capacities, and selective porosity which is a favorable characteristic for gas separation applications. Therefore, NU-1000 has been investigated both computationally and experimentally for the capture of different gases.[197] The adsorption isotherms and the determination of the isosteric heats of adsorption of several gases (H_2, D_2, Ne, N_2, CO, CH_4, C_2H_6, Ar, Kr, and Xe) on NU-1000 have been demonstrated, where the adsorption sites were predicted and understood *via* DFT calculations.[195,198] Results showed that the adsorption of the gas molecules starts with strong adsorption sites near Zr atoms, followed by the filling of other adsorption sites on the nodes and organic framework. NU-1000 is also the perfect candidate for post-synthetic modifications thanks to the presence of functional groups (–OH groups) on Zr_6 nodes. Deria *et al.*[130] investigated the functionalization of NU-1000 with perfluoroalkane groups (SALI-*n*, where n = 1, 3, 7, 9 depending on the varying chain length of the perfluoroalkyl carboxylic acids) for improving the interactions with CO_2. The selection of perfluoroalkene groups was based on two main reasons: (i) fluorinated MOFs have been attractive candidates due to their hydrophobicity, which is an important feature for post combustion CO_2 capture, and (ii) the presence of C–F dipoles is expected to improve the interactions between the framework and the quadrupole of CO_2. As a result, SALI-*n* samples showed higher isosteric heat of adsorption values with increasing chain length, where the value of NU-1000 (17 kJ mol^{-1}) was doubled in SALI-9 (34 kJ mol^{-1}). SALI was applied to another pyrene-based Zr-MOF, NU-901, by the incorporation of amine moieties which are well-known functional groups for enhancing the interactions of CO_2 molecules with the framework.[199] CO_2 isotherms showed that NU-901-SALI-BA-3,5-NH_2 presented better CO_2 adsorption than those of activated NU-1000 and NU-901. It also showed better CO_2 uptake compared to that of NU-901-BA-NH_2, where the amine functionalization was introduced during the synthesis by the use of 4-aminobenzoic acid as the ligand. The inferior performance of NU-901-BA-NH_2 can be attributed to the position of the 4-amino benzoic acid, which significantly blocks the microporous channels and inhibits the access to the amino groups. In addition to SALI, post-synthetic modifications on NU-1000 have been also performed by the impregnation of amine molecules (polyethyleneimine) in the pores, resulting in approximately 37 times higher selectivity toward CO_2 than that of the pristine NU-1000.[200]

3.3.2 Organic and inorganic pollutants. The structural stability of the MOFs has been the major concern to date for the adsorption of organic and inorganic pollutants from water.[201] The sensitivity of MOFs to water is arising from the weak coordination between the metal and organic linkers, which can be overcome by their careful selection. Some pyrene-based MOFs can be attractive materials for this application thanks to not only their water stability but also their high porosity and specific adsorbate/adsorbent interactions.[202] For example, Zr_6-based pyrene-MOFs show exceptional water stability owing to their strong Zr(IV)–O bonds and high connectivity of the Zr node. Therefore, NU-1000 has been of interest to the adsorption and removal of organic and inorganic pollutants from water. In addition to its water stability, NU-1000 has large channels that can promote the diffusion of pollutant molecules, as well as terminal Zr–OH groups on the Zr_6-node which can be replaced by negatively charged analytes.[203]

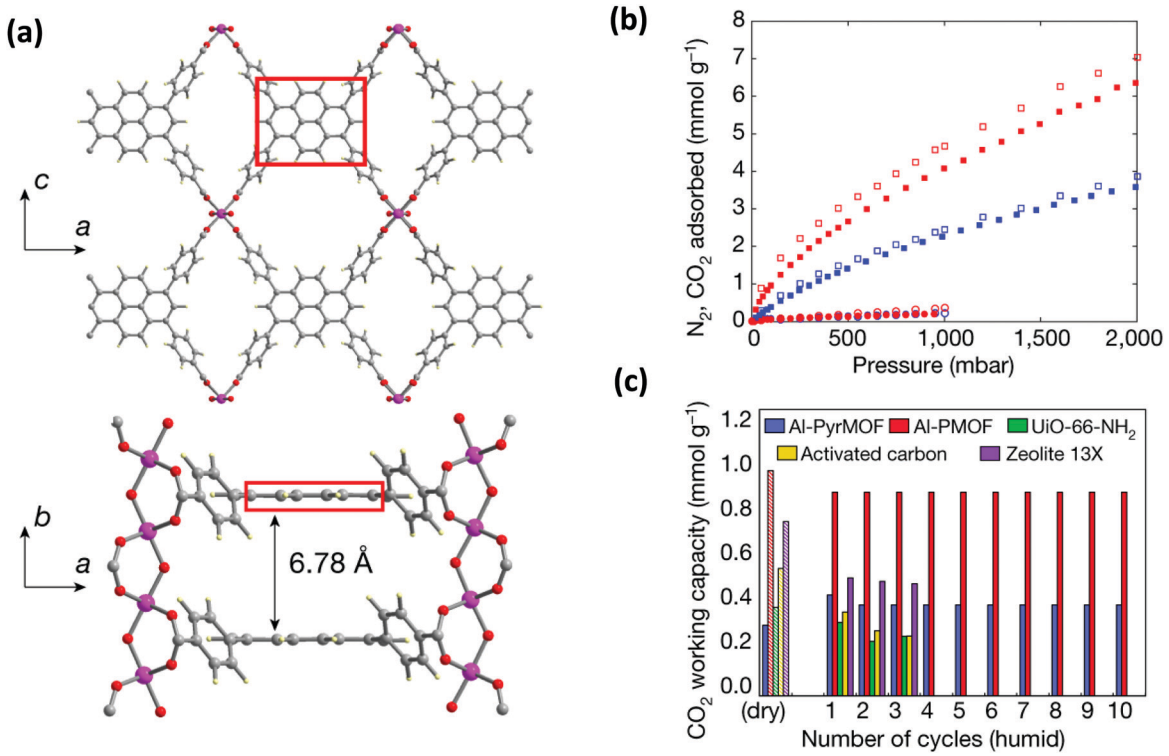

Fig. 9 (a) The representation of the three-dimensional non-interpenetrated structure of Al-PyrMOF that is constructed from Al(III) rods connected by TBAPy ligands. The distance between two adsorbaphores (shown in red box) is calculated as 6.78 Å, which is very close to the computational value. Atom colour code: pink, Al; grey, C; blue, N; red, O; pale yellow, H. (b) Experimental CO_2 (filled squares), experimental N_2 (filled circles), computational CO_2 (open squares) and computational N_2 (open circles) single-component adsorption isotherms collected on activated Al-PMOF (red) and Al-PyrMOF (blue) at 313 K. (c) Recycling ability of Al-PyrMOF in comparison with other materials under dry and humid (85% relative humidity) conditions, with 85/15 v/v of N_2/CO_2 (313 K and 1 bar). Modified and reprinted with permission from ref. 85.

Inorganic anions released from mining and industrial production activities are one of the major toxic pollutants in water, creating serious environmental and health problems. Since they are usually large molecules in size, the selection of the MOF based on the size of the analytes is the key criteria. NU-1000 has been studied for the removal of different toxic anions from water, not only because of its water stability but also thanks to its pore sizes. NU-1000 has uniform hexagonal channels with diameter 31 Å and triangular channels with diameter 10 Å aligned parallel to the *c*-axis, which are connected *via* small pores of 8 Å. Therefore, it has large enough pores for the diffusion of the anions. The anions in different sizes, including (i) selenite (SeO_3^{2-}, 4.82 Å) and selenate (SeO_4^{2-}, 5.20 Å),[204] (ii) antimonite ($Sb(OH)_3$, 3.05 Å) and antimonate ($Sb(OH)_6^-$, 7.36 Å),[203,205] and (iii) dichromate ($Cr_2O_7^{2-}$, 6.00 Å)[206] could be successfully removed from the aqueous solutions by NU-1000. The removal performance toward the anions SeO_3^{2-}, SeO_4^{2-}, Sb(III) and Sb(V) was remarkably better compared to some other Zr-MOFs, such as UiO-66 functionalized with different groups ($-NH_2$, –OH, and $-SO_3H$) and UiO-67. In the case of $Cr_2O_7^{2-}$, the uptake capacity of NU-1000 could surpass not only other Zr-MOFs but also some well studied MOFs, such as HKUST-1, ZIF-8, and MIL-100(Fe). These results highlight the importance of both large pore size and substantial bridging sites in the nodes of NU-1000 for the fast and efficient adsorption of different inorganic anions. In all cases, the presence of terminal hydroxyl groups on the Zr_6 nodes can be replaced by the anions and work as efficient adsorptive sites as demonstrated in Fig. 10. ICP-OES analysis established that no zirconium is lost to solution during the adsorption of the anions. Moreover, NU-1000 framework remains intact after the adsorption, proved by different characterization techniques; including PXRD, FTIR and surface area measurements.

NU-1000 is also a good candidate for the removal of organic pollutant molecules, including volatile organic compounds (VOCs) and herbicides, which are harmful to both environment and human health. Thanks to π–π stacking interactions between the VOCs and pyrene-based ligand, SION-82 synthesized by Sudan *et al.*[98] was found to capture some common VOCs (benzene, pyridine, and thiophene) effectively. SION-82 captured benzene efficiently (107 mg g^{-1}) in dry conditions, and no uptake decrease was observed in the presence of high relative humidity for at least six cycles. Atrazine is a widely used herbicide in the agricultural industry, which contaminates the surface and groundwater supplies. Akpinar *et al.*[207] studied the effect of the linkers in Zr-MOFs on atrazine uptake capacity and uptake kinetics. Results showed that although UiO-67, DUT-52, and NU-1000 have similar pore sizes and surface areas, NU-1000 showed an exceptional atrazine uptake because of π–π interactions between the pyrene and the atrazine. Another organic

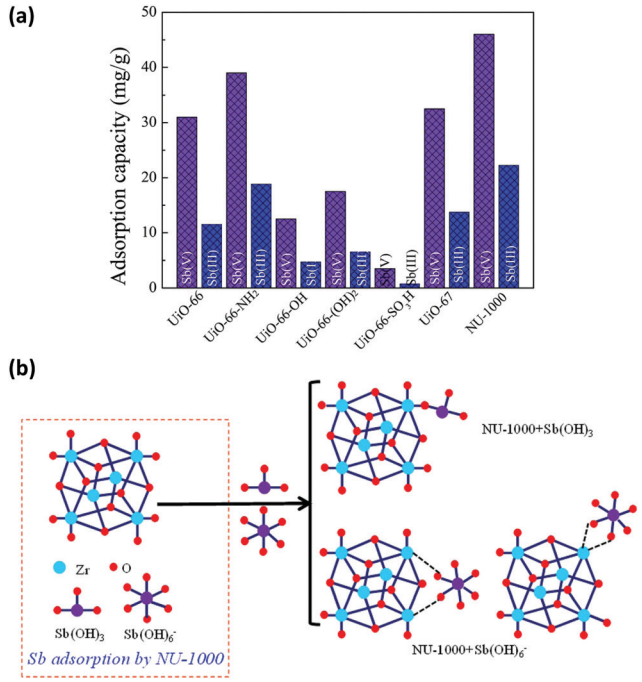

Fig. 10 (a) Adsorption rates of $Sb(OH)_3$ and $Sb(OH)_6^-$ in different Zr-MOFs, (b) different binding possibilities of $Sb(OH)_3$ and $Sb(OH)_6^-$ to the node of NU-1000. Reprinted with permission from ref. 205.

pollutant resulting from the use of herbicides is glyphosate, which causes damage to human cells and increases the risk of erosion and contamination of surface and groundwater sources. Pankajakshan *et al.*[208] studied the adsorption of glyphosate using NU-1000 and UiO-67. The selection of these MOFs were because of the higher affinity of Lewis acid Zr metal nodes for the phosphate functional group of glyphosate, which is a Lewis base. The presence of wide pores (31 Å) in NU-1000 allows the glyphosate solution to interact better with the metal nodes compared to UiO-67, resulting in better adsorption performance.

The nuclear weapon industry and the use of toxic chemical warfare agents (CWAs) result in extremely toxic pollutants. Therefore, efficient and safe removal is highly important. Technetium-99 (Tc-99) is a fission product resulting from nuclear weapon activities and it is in the form of a highly soluble, environmentally mobile, and volatile pertechnetate ion (TcO_4^-) in the oxidizing environment. Drout *et al.*[209] evaluated NU-1000 as a sorbent for aqueous perrhenate (ReO_4^-), which is the non-radioactive simulant for TcO_4^-. Single-crystal X-ray diffraction showed that ReO_4^- ions bind in a unique chelating mode in both small pore and mesopore of NU-1000 in addition to two non-chelating modes in each pore, resulting in a promising adsorption efficiency. Asha *et al.*[210] investigated NU-1000 toward the capture of two CWA simulants, 2-chloroethyl ethyl sulfide (2-CEES, the simulant of sulfur mustard gas), and dimethyl methyl phosphonate (DMMP, the simulant of sarin). NU-1000 performed efficient and reusable adsorption of the simulants from the aqueous medium. The remarkable performance of NU-1000 is due to the chemical interactions between the thioether and chloro groups of 2-CEES, and phosphate groups of DMMP, with the Zr–OH groups of the MOF. Further studies showed that DMMP can be effectively adsorbed even from the air at ambient conditions and decomposed in the pores of the MOF.[211]

Very recently, water-stable anionic pyrene-based uranium MOFs have drawn attention with the aim of efficient separation of organic dyes and biomolecules,[79] as well as the separation of fission products produced in the nuclear fuel cycle.[81] The combination of a uranium salt with a highly symmetrical carboxylic pyrene-based ligand eventuated in different porous uranyl frameworks. Li *et al.*[79] designed a 3D water-stable pyrene-based uranium MOF, NU-1300. Thanks to its anionic nature, NU-1300 shows a remarkable performance for the selective adsorption of positively charged molecules compared to negatively charged ones. This was proved by the study of selective adsorption of the cationic dyes (methylene blue (MEB), JanusGreen B (JB), ethyl violet (EV)) over an anionic dye (resorufin sodium salt (RS)). While 85% of RS remained in the solution, 10% of MEB, and 20% of JB and EV remained in the solution at the end of 42 h. The capture of anionic dyes was also evidenced by the changes in the absorbance of the supernatant solutions. The cation capture ability of NU-1300 was further confirmed by performing the separation of two proteins, a cationic enzyme (cytochrome *c*, Cyt-*c*) selectively over the anionic protein (a-lactabumin, a-La) analyzed by UV-Vis spectra. Similarly, Ai *et al.*[81] synthesized two porous pyrene-based uranium MOFs, UOF-1 and UOF-2, for the adsorption of radioactive Cs^+ cations from the aqueous solutions. Both MOFs were able to capture Cs^+ cations from the aqueous solution efficiently due to their anionic frameworks. Single-crystal XRD analysis of as-synthesized samples indicates that $[(CH_3)_2NH_2]^+$ cations are present in the channels of both MOFs as the counter ions. The crystallinity of structures remained the same after the adsorption of Cs^+ cations thanks to their exchange with $[(CH_3)_2NH_2]^+$ cations in the channels. Upon adsorption, two adjacent $[UO_2(COO)_3]^-$ SBUs share Cs atoms to form a 1D chain, and then these 1D chains are further linked by a TBAPy ligand to construct a 3D extended architecture.

3.3.3 Hydrocarbons. The adsorption and separation of hydrocarbons are of importance due to their use as feedstocks for the production of valuable consumer and industrial products. Pyrene-based MOFs are promising materials for the adsorption of hydrocarbons thanks to their structural features; such as large-enough pore sizes for the accommodation of hydrocarbon molecules,[60] and tunability for the synthesis of breathing frameworks based on the design of pyrene-ligand.[108] Some pyrene-based MOFs tend to have hierarchical structures by having both micropores and mesopores in their frameworks, resulting in different diffusion behaviors of the hydrocarbon molecules in different channels. A computational study was performed by Vargas *et al.*[212] on the hierarchical NU-1000 to investigate the adsorption dynamics of alkane molecules in different lengths (methane, ethane, propane, and butane) in the pores. Results showed that alkane molecules in the mesochannels and microchannels undergo much different dynamics: while the diffusion in mesochannels is fast, the diffusion in microchannels is slower

and depends on the molecular size of the alkane molecule. A similar result was obtained by Chen *et al.*,[213] where the diameter of the microchannels and the size of the windows that connect microchannels and mesochannels on NU-1000 were observed as determinant characteristics affecting the diffusion behavior, particularly at lower pressures. The hierarchical structure of NU-1000 can also facilitate its utilization in adsorption-based cooling systems.[214–216]

Pyrene-based MOFs are also favorable for the separation of hydrocarbon mixtures thanks to the favorable interaction of some hydrocarbon molecules with the pyrene.[217] The separation of acetylene (C_2H_2) from CO_2 is an important industrial hydrocarbon separation process with a major difficulty originating in the similar molecular shapes of C_2H_2 and CO_2. Moreover, the presence of water or moisture is usually a significant drawback for this industrial separation process. Based on these necessities, a pyrene-based MOF, JXNU-5 was constructed from TBAPy ligand and one-dimensional europium carboxylate rods by Liu *et al.*[90] The presence of strong π–π stacking interactions between conjugated pyrenes resulted in water-resistant JXNU-5. Structural investigations demonstrated that the carboxylate oxygen atoms of the europium carboxylate rods are exposed on the pore wall, which are desirable sites for the acidic H atoms of C_2H_2 molecules but are unfavorable sites for CO_2 molecules with two electronegative O atoms. Consequently, JXNU-5 could adsorb more C_2H_2 (55.9 $cm^3\ g^{-1}$) then CO_2 (34.8 $cm^3\ g^{-1}$) at 298 K and 1 atm. The separation of C_2 hydrocarbons including C_2H_2, C_2H_4 (ethylene) and C_2H_6 (ethane) from CH_4 is as important to ensure more effective use of natural gas and utilization of C_2 hydrocarbons for other useful processes. Huang *et al.*[93] synthesized $(Me_2NH_2)_2[Zn_6(TBAPy)_2(Ade\text{-}NH_2)_4(\mu_4\text{-}O)](DMF)_{10}(H_2O)_8$ (**bioMOF 1-NH$_2$**) by the coordination of Zn(II) with TBAPy and 2-aminoadenine (Ade-NH_2). The structure exhibits one-dimensional tubular channels with exposed Watson–Crick faces and nitrogen-rich purines, providing strong adsorption sites for C_2 hydrocarbons. The additional amine groups positioned toward the pores enhanced the adsorption capacity of more polarizable C_2 molecules by contrast with CH_4.

3.3.4 Carbohydrates and carbohydrate-derived aromatics. Physicochemical pretreatment is necessary to access polysaccharides which are tightly locked in cellulosic biomass feedstocks. However, some undesirable aromatic sugar-derived compounds are released into aqueous solutions unavoidably along with the sugars.[218] MOFs have been suggested as favorable candidates for the separation of these compounds. Pyrene-based MOFs are particularly promising thanks to the aromatic pyrene in the structure, which might favor the separation of furanics, furfural, and lignin-derived phenolics by π–π interactions since these compounds also possess aromaticity.[219] On this basis, NU-1000 has been of interest to the separation of sugar-derived organic compounds.

Different studies on NU-1000 have been performed by Yabushita *et al.* for the separation of aromatic compounds from hydrocarbons in aqueous solution, including (i) furanics (*e.g.* 5-hydroxymethylfurfural (HMF) and furfural)[219] (ii) phenolics (*e.g.* 4-hydroxybenzaldehyde, 4-hydroxybenzoic acid, vanillin, vanillic acid, syringaldehyde, and syringic acid),[218] and (iii) coumaric and ferulic acids.[220] In all studies, aromatic compounds have successfully been separated from the sugars that they were derived from. The adsorption of sugars such as glucose, fructose, and xylose was excluded in all cases when they are in competition with the aromatics. However, results showed that the use of ionic liquid (IL) can enhance the uptake of NU-1000 toward monomeric sugars as a result of the generation of new adsorption sites by the incorporation of IL into the MOF space.[220] NU-1000 can be further used for the molecular recognition of different types of sugars, which may be crucial for the selective synthesis of glucose from biomass-based feedstocks *via* cellulose depolymerization.[221] Previous studies on enzyme-catalyzed depolymerization of cellulose showed that the presence of cellobiose can result in product inhibition and glucose product degradation. Therefore, it is promising that NU-1000 can adsorb cellobiose efficiently while the adsorption of glucose was excluded. Electronic structure calculations demonstrated that the reason of the selective molecular recognition is the number of favorable CH–π interactions made by the axial CH groups on a single face of the molecule with pyrene units of the MOF, which is higher in the case of cellobiose compared to that of glucose (Fig. 11). Because of the same reason, the interaction of sugars with pyrene of NU-1000 are weaker than that of aromatics.[221]

3.3.5 Radioactive gases. The use of nuclear fuel should be reprocessed to recover fissile materials and reduce radioactive waste.[222] Along this process, the main problem is the release of volatile radionuclides. Pyrene-based MOFs are efficient materials for the capture of these molecules thanks to the presence of enriched π-conjugated electron cloud on the pyrene linker. The separation of krypton (Kr) from xenon (Xe) is important because of the longer half-life of radioactive ^{85}Kr ($t_{1/2}$ = 10.8 years) than that of radioactive ^{127}Xe ($t_{1/2}$ = 36.3 days).[222] NU-1106 synthesized by Maldonado *et al.*[72] performed Xe adsorption two times more than that of Kr, resulting in a promising Xe/Kr selectivity. This could be attributed to the greater polarizability of Xe and its stronger interaction with a complex π system of the pyrene. Another major volatile radionuclide is iodine (I_2), whose ^{129}I isotope has a half-life of 15.7 million years and can damage biosphere extremely in the long-term. Pyrene-based MOFs have been studied for the capture of I_2 vapor based on the well-known donor–acceptor interaction between pyrene and I_2.[223] Gładysiak *et al.*[91] synthesized SION-8, which could adsorb I_2 vapor at room temperature by reaching 34 wt% (340 mg g_{MOF}^{-1}) after 200 hours. The adsorption can be visually observed by the color change of the yellow powder of SION-8 to black. The electrochemical impedance spectroscopy measurements were performed to confirm the charge transfer between the pyrene core of TBAPy and I_2. While SION-8 is an insulator, the I_2-adsorbed SION-8 (SION-8 ⊃ I_2) showed electrical conductivity, proving the donor–acceptor charge transfer. Similarly, NU-1000 has been studied for the capture of volatile I_2 by Chen *et al.*[224] NU-1000 could adsorb 1.45 g_{I_2}/g_{MOF} at 80 °C, thanks to the presence of the –OH groups of Zr_6 nodes and enriched π-conjugated electron clouds on pyrene. Pyrene can donate abundant negative charges, making NU-1000 convenient to host iodine.

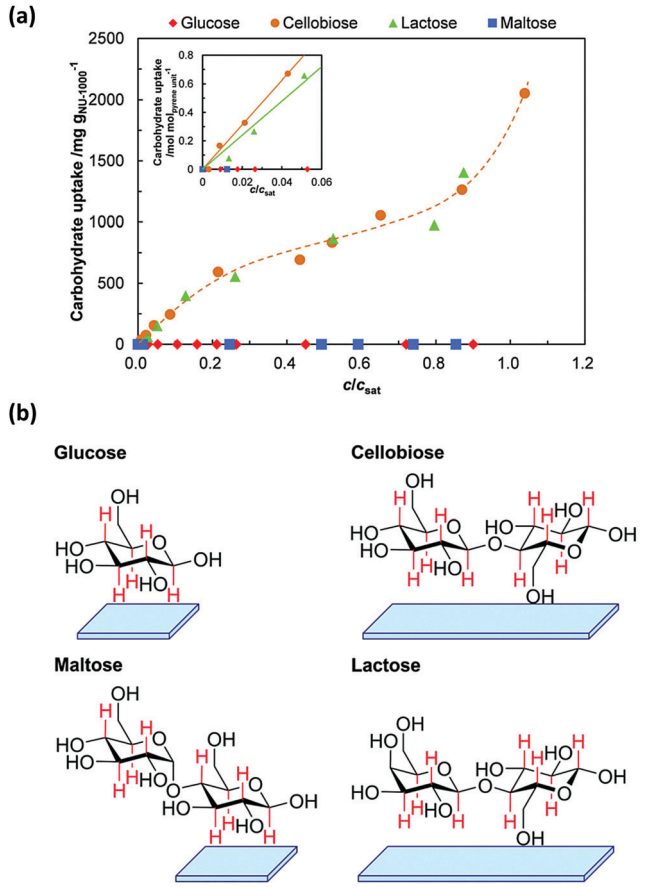

Fig. 11 (a) Adsorption isotherms of carbohydrates on NU-1000 at 297 K, where c/c_{sat} in x-axis defines the equilibrium concentration relative to the saturation concentration. The inset shows isotherms in a low concentration range. (b) Illustration of the structures of different carbohydrates and their adsorption on NU-1000. The red protons are on an axial plane of each carbohydrate. The blue plates represent the adsorptive areas of pyrene units in which the hydrocarbons can interact with. Modified and reprinted with permission from ref. 221.

Since the use of pyrene-based MOFs can be advantageous for the capture of radioactive gases, their stability under radiation conditions at nuclear energy reprocessing sites is highly important. Hanna *et al.*[225] investigated the radiolytic stability of NU-1000 by exposing gamma irradiation. The PXRD pattern of NU-1000 showed no change after both high and low irradiation dose, confirming the structural stability of the MOF. Moreover, the surface area and morphology remained the same as demonstrated by N_2 physisorption isotherms and SEM images. This can be attributed to (i) higher linker connectivity of NU-1000 making it more stable toward cleavage of the carboxylate oxygen-zirconium bonds, (ii) low density of Zr_6O_8 nodes in NU-1000, causing the absorption of a limited amount of radiation, and (iii) the absorption of radiation mainly by Zr-nodes then its transfer to the dangling –OH and H_2O groups, rather than damaging TBAPy linkers.

3.4 Heterogeneous catalysis

Heterogeneous catalysis is one of the most extensively studied fields with MOFs due to their high chemical versatility, porosity allowing molecules diffusion, and the presence of catalytically active centers in the structure. The catalytic function can be implemented at the organic ligand or metal node, which can be done by the direct synthesis or post-synthetic modification such as AIM and SALI. In addition, some catalytically active species can be incorporated in the pores of the MOF by encapsulation. In this way, MOFs can either participate in the catalytic reaction by stabilizing transition states, orienting molecules, or presenting additional active sites. They can also act as a medium for dispersing the catalytic species.[226] The inclusion of pyrene ligands in the structure of MOFs has drawn attention to heterogeneous catalysis due to its advantageous electronic properties. Studies on graphene and carbon nanotubes (CNT) showed that the introduction of pyrene into the catalytic systems can enhance the electron transfer efficiency due to the strong $\pi-\pi$ interactions, resulting in better catalytic activity.[227,228] Based on this, Tu *et al.*[88] synthesized Fe-TBAPy for benzene hydrolxylation, considering that the 3.4 Å pores sandwiched between the pyrene cores of TBAPy could be the strong adsorption-sites because of the strong $\pi-\pi$ interaction between the benzene and the pyrene. Therefore, as an emerging subfamily, pyrene-based MOFs have aroused interest in the last years and been investigated for several heterogeneous catalytic reactions computationally and experimentally. As yet, computational studies have focused on the study of energetic barriers, formation mechanisms and the post-synthetic modification of catalytic active sites on the Zr_6 nodes in NU-1000 for different catalytic reactions; including ethylene dimerization,[111,229,230] ethylene hydrogenation,[231] alkyne semihydrogenation,[232] alcohol dehydrogenation,[233] hydrolysis of CWAs,[234,235] and C–H bond activation.[236–238] In addition, computational studies have been informative about the importance of the selection of transition metals for the post-synthetic functionalization on the node, and supports for the design of heterogeneous catalyst.[239]

The interest in NU-1000 has increased to a very great extent thanks to the experimental post-synthetic modification methods, such as AIM, SIM, and SALI, to introduce different secondary metal components in the framework. The applicability of post-synthetic modifications is owing to the large mesopores of NU-1000, which allows efficient and homogeneous metalation on the zirconium nodes and promotes diffusive transport of substrates within the MOF during heterogeneous catalysis.[141] Moreover, the stability of the structure in different environments as well as the high porosity and large enough channels of NU-1000 also enable the impregnation of guest molecules. In the following sections, the experimental heterogeneous catalytic reactions performed by NU-1000 will be focused mainly due to its rising popularity among all pyrene-based MOFs.

3.4.1 Catalytic applications of guest-incorporated NU-1000.

NU-1000 is the perfect host material for supporting guests in different sizes, ranging from single atoms or small molecules to relatively large nanoparticles or bio-molecules. The encapsulation of metal nanoparticles is of interest since their sizes and shapes may lead to superior catalytic activity. DFT calculations performed on Cu NPs and NU-1000 by Ye *et al.*[240] showed that

TBAPy is responsible for the diffusion and nucleation of the Cu nanoparticles. From an energy point of view, the interactions are more favorable with the pyrene moiety than the Zr_6 node. Since the aggregation of active nanoparticles is a major problem in heterogeneous catalysis, Redfern *et al.*[241] prepared CuNPs@NU-1000 using the templating effect of structurally well-defined NU-1000. Cu–oxo clusters were first anchored uniformly on the Zr_6 node of NU-1000, followed by the mild reduction in a flow of H_2, resulting in Cu nanoparticles generated inside the pores of NU-1000. The material showed excellent activity and stability toward the semi-hydrogenation of acetylene to ethylene without the formation of any undesired product such as ethane. An enzyme (cutinase) was immobilized in the channels of NU-1000 by Li *et al.*[242] to enhance its stabilization, easy separation, and recyclability. The immobilized enzyme demonstrated better structural stability, and resulting cutinase@NU-1000 material showed better catalytic activity toward the hydrolysis of different esters than that of free enzyme. A bulky molecule, $[Mg(OMe)_2(MeOH)_2]_4$ was incorporated in the mesopores of NU-1000 by o Gil-San-Millan *et al.*[243] for the hydrolytic degradation of organophosphonate-based nerve agents. The catalytic activity of NU-1000 was improved toward the hydrolytic degradation of P–F and P–S bonds of toxic nerve agents by the incorporation of $[Mg(OMe)_2(MeOH)_2]_4$. Monte Carlo computational modeling demonstrated that $[Mg(OMe)_2(MeOH)2]_4$ sits in the mesopore channels of NU-1000 while toxic molecules can diffuse through both micropores and mesopores.

Due to their tendency to aggregate and instability in solutions, polyoxometalates (POMs) are one of the most studied species supported by NU-1000.[244] POMs are anionic metal oxide clusters composed of group V or VI transition metals having acid–base and redox properties. NU-1000 has been found as an appropriate support for POMs thanks to its small triangular channels (12 Å) enabling the incorporation of large POMs while the larger (31 Å) hexagonal channels promote the substrate diffusion.[245] For example, Ahn *et al.*[246] showed that the incorporation of phosphotungstic acid (PTA, $H_3PW_{12}O_{40}$) in NU-1000 can be successfully performed and can provide the tungsten oxide active sites for the acid-catalyzed reaction of *o*-xylene isomerization/disproportionation. The structure remained stable after the catalysis, showing the applicability of POM-incorporated MOFs (POM@MOFs) even for aggressive reactions such as hydrocarbon isomerization.

POMs are also successful catalysts for acid and oxidation reactions; therefore, POM@MOFs have been studied for the oxidative detoxification of a mustard gas simulant, CEES. The oxidation products can be either a singly oxidized sulfoxide (CEESO), or a doubly oxidized sulfone ($CEESO_2$). While CEESO is considered nontoxic, $CEESO_2$ has detrimental effects similar to the mustard gas. Therefore, the selectivity of the reaction is highly important. Two different POMs, $H_3PW_{12}O_{40}$ and $H_5PV_2Mo_{10}O_{40}$, have been encapsulated in NU-1000 (named as PW_{12}@NU-1000[245,247,248] and PV_2Mo_{10}@NU1000,[244] respectively) for the oxidation of CEES using hydrogen peroxide (H_2O_2) as the oxidant. Results showed that while 100% conversion of the parent agent is successfully done, the problem is the selectivity toward the desired non-toxic oxidation product.[244] For example, Buru *et al.*[245] showed that PW_{12}@NU-1000 could successfully convert CEES in 20 min; however, the selectivity toward CEESO remained at 57%. They also investigated the performance of $H_3PW_{12}O_{40}$ and NU-1000 individually, finding that while $H_3PW_{12}O_{40}$ promoted the selective oxidation of CEES, NU-1000 is overoxidizing CEES by the formation of $CEESO_2$. Based on this, the effect of the POM location and accessibility of substrates on the catalytic rate and selectivity have been investigated using the same system. The samples were activated in different ways, under vacuum at 120 °C for PW_{12}@NU-1000-120, and by supercritical CO_2 drying for PW_{12}@NU-1000-$scCO_2$.[247] While 100% conversion in 20 min with 59% selectivity was observed for PW_{12}@NU-1000-120, 100% conversion in <10 min with 90% selectivity was obtained for PW_{12}@NU-1000-$scCO_2$. Volumetric N_2 sorption isotherms showed that PW_{12}@NU-1000-$scCO_2$ has a reduced mesopore volume, yet PW_{12}@NU-1000-120 has reduced micropore volume. This can indicate that in PW_{12}@NU-1000-120, the POM is situated in micropores and the mesopores of MOF are accessible, resulting in the formation of both CEESO and $CEESO_2$ products. When the POM is situated in the mesopores as in the case of PW_{12}@NU-1000-$scCO_2$, diffusion of the substrate to POM in the pores is no longer hindered and singly-oxidized product is formed almost exclusively.

3.4.2 Catalytic applications of cluster-metalated NU-1000. NU-1000 is an excellent platform for metalation by AIM and SIM given its thermal and structural stability, 31 Å wide mesoporous hexagonal channels, and spatially isolated –OH groups on the Zr_6 nodes. AIM and SIM functionalization of NU-1000 have been mainly performed by the deposition of single metal atoms, metal clusters, metal oxides, and metal sulfides on the Zr nodes to perform different catalytic applications; such as hydrogenation,[128,135,249–254] oxidation,[129,141,145,255–257] dehydration,[258–260] oligomerization,[147,261] epoxidation,[142,262] polymerization,[263] and hydrolysis.[264] Studies showed that the formation of single-site catalysts including metal atoms, clusters or oxides can enhance the catalytic activity toward different aforementioned catalytic reactions thanks to the strong interactions between the deposited metal site and the Zr_6 node. Moreover, the agglomeration and migration of the metal ions could be inhibited. Consequently, resulting catalysts were found to be stable and reusable at high temperatures and under different catalytic environments. Table 5 summarizes the studies with AIM- and SIM-modified NU-1000 up to date.

SALI-based functionalization of MOF nodes enables of the fine-tuning the electronic properties and/or the Brønsted acid character of the MOF catalyst. In the case of NU-1000, SALI approach takes advantage of the ability of the Zr_6 nodes to be altered through the reaction between the free Zr–OH moieties (labile –OH and H_2O ligands) and introduced nonstructural organic ligands.[90] The functional ligands may be carboxylic acid containing molecules,[265–269] phosphonic acid containing molecules,[270] or perfluoroalkane chains,[271] in which their addition in NU-1000 results in enhanced activity in different catalytic reactions. Moreover, the further modification of the ligands with varying electron-donating or electron-withdrawing

Table 5 Cluster-metalated AIM- and SIM-NU-1000 materials for different catalytic applications

Reaction	Reactant	Material name	Ref.
Hydrogenation	*m*-Nitrophenol	CoS-AIM	128
	Ethylene	$Ir(C_2H_4)_2$-supported NU-1000	249 and 250
	Ethylene	Ni-AIM	135
	Ethene	ReO_x-functionalized NU-1000	251
	Ethylene	Pt-AIM	253
	Diphenylacetylene	Rh-Ga-NU-1000	254
Oxidation	Benzyl alcohol	Co-Al-NU-1000	255
	Methane	Cu-NU-1000	256
	Propane	Co-SIM + NU-1000	129
		Co-AIM + NU-1000	
	Propane	CoAIM-M-SIM-NU-1000 (M = Ni, Zn, Al, Ti, Mo)	257
	4-Methoxybenzyl alcohol	V-NU-1000	141
	4-Methoxybenzyl alcohol	Zr-NU-1000-V	145
Dehydration	Ethanol	Al-NU-1000	258
	2-Propanol	Si-NU-1000	259
	Glucose	PO_4/NU	260
Oligomerization	Ethylene	Ni-Facac-AIM-NU-1000	
		Ni-Acac-AIM-NU-1000	261
	Ethylene	Cr-SIM-NU-1000	147
Epoxidation	Cyclohexene	Mo-SIM	142
	Cyclohexene	Nb-AIM	
		Nb-SIM	262
Polymerization	Ethylene and 1-hexene	Hf-NU-1000-ZrBn	263
Hydrolysis	Nerve agent simulant	Ce-*n*-SIM-NU-1000	
		Ce-l-SIM-NU-1000	264

groups can be performed to tune the electronic environment provided by the Zr_6 nodes.[267] SALI-modification of NU-1000 can be performed with an organic ligand,[268] or a metal complex featuring an organic ligand.[269] NU-1000 functionalized by 5,5-di-thio-bis(2-nitrobenzoic acid) ligand (DTNB@NU-1000) was found to be catalytically active for the degradation and subsequent detection of a nerve agent, which was observed by the release of the chromophore degradation product by visual inspection of filtered samples.[268] The immobilization of an Ir(III) complex with a bis-phosphinite pincer ligand in NU-1000 was performed to enhance the catalytic activity toward the hydrogenation of liquid alkenes (1-decene and styrene) compared to that of homogeneous Ir(III)-complex, by preventing leaching of Ir from the structure.[269] SALI-based ligand incorporation can be followed by anchoring catalytically active metal sites on the ligand attached to the Zr nodes. Madrahimov *et al.*[270] synthesized NU-1000-bpy-$NiCl_2$ by SALI-modification of NU-1000 with 5-methylphosphonate-2,2′-bipyridine (NU-1000-bpy), followed by the exposure of NU-1000-bpy material to a solution of anhydrous $NiCl_2$. While NU-1000 and NU-1000-bpy showed no activity for liquid-phase ethylene dimerization, NU-1000-bpy-$NiCl_2$ showed 95% conversion with 93% selectivity toward the desired product, 1-butene. Similarly, Berijani *et al.*[266] immobilized L-tartaric acid on the Zr_6 nodes of NU-1000 and then anchored Mo(IV)-complex on the ligand as the Lewis acid site, forming a chiral heterogeneous catalyst C-NU-1000-Mo. The catalyst could successfully perform the epoxidation of various prochiral alkenes to form enantiomers of epoxides, where the conversion of styrene to styrene epoxide was completed in 5 h with 86% selectivity. The deposition of metal ions on a specific location can be also provided by SALI-modification. Peters *et al.*[265] modified NU-1000 with naphthalene dicarboxylate (NDC) linkers to block the small cavities where few-atom clusters of cobalt oxide preferentially grow. This approach can be highly useful where catalyst location matters for the enhanced catalytic reactivity. In addition to the deposition of metal ions, metal nanoparticles can be incorporated in SALI-modified NU-1000 as studied by Huang *et al.*[271] NU-1000 has been modified with perfluoroalkane groups to provide a hydrophobic platform to encapsulate Pd nanoparticles in the pores. The resulting material Pd@F15-NU-1000 was found to be catalytically active (87% conversion with 21% selectivity) for the direct C–H arylation of indoles in water.

3.5 Electrochemistry applications

MOFs have recently attracted the attention of electrochemical applications like electrochemical catalysis,[272] supercapacitors,[273] batteries,[274] and electrochromic devices.[75] The presence of well defined porous channels is one feature of interest for ion transport. However, one major limitation of MOFs for being fully considered in electrical and electrochemical applications is their intrinsic low electrical and direction-dependent conductivity. Charge transport in MOFs presents a small electronic coupling and frontier orbitals overlap, given the separation between linkers.[275] In this regard, pyrene-based MOFs like NU-901 and NU-1000 have been modified *via* post-synthetic modifications to improve the conductivity properties suitable for electrochemical applications. Wang *et al.*[276] incorporated thiophene oligomers on the Zr_6 node of NU-1000 *via* SALI to improve the electronic conductivity of the material. The length of the oligomers allowed the electrochemical conversion to a channel-anchored strands of polythiophene, resulting in a material with an improved conductivity without compromising the MOF porosity. Another strategy is to exploit the donor nature of the

pyrene moiety combined with electron acceptor molecules. The porous topology of NU-1000 and NU-901 have been exploited to the encapsulation of acceptor moieties like metallacarboranes[277] and buckminsterfullerene (C_{60})[278] as guest molecules, tuning the conductivity *via* donor–acceptor interactions.

Although different strategies can lead to conductive MOFs, it is important to understand the mechanisms of charge transport in MOFs. Charge propagation in MOFs can be as a result of ligand-node orbital energy overlap, π-stacking interactions and redox hopping. The last one is of great importance for electrocatalytic applications. Several studies have anchored redox active building blocks like metallocenes in NU-1000 for redox hopping transfer and as a redox shuttle in photoelectrochemical or electrocatalytic systems.[279–281] Celis-Salazar *et al.*[281] studied the electron diffusion and ion diffusion in the redox-hopping process in three metallocene-doped (M = Fe, Ru, Os) NU-1000 MOFs *via* chronoamperometric response measurements. Their results highlighted the importance of metal for electron diffusion, likewise ion mobility can lower due to ion-pairing associations. The electron redox hopping rates inside M-NU-1000 frameworks can be controlled through the modifications of the self-exchange rates of redox centers and proper selection of counteranions.[281] Charge transport properties can be also affected by the topology of the MOF. In NU-1000 the redox-hopping-based charge transport is highly anisotropic, presenting a higher diffusion coefficient along the one-dimensional mesopores.[282] These fundamental electronic properties and findings have direct implication for the design and further optimization of pyrene-based MOFs in electrochemical applications, where the understanding of the charge transport mechanism behavior is essential.

Based on redox-active and catalytic functionalities, electroactive pyrene-based MOFs can be synthesized as thin films *via* atomic layer deposition (ALD)[283] or electrophoretic deposition (EPD).[284] EPD thin-film technique distinguishes from the previously discussed ALD (Section 2.3.1) by the direct use of an electric field. EPF is based on the movement and deposition of charged particles under the electric field onto a conductive electrode, to develop thin or thick films and coatings. The thickness and morphology of the films can be controlled by simply adjusting the depositing time and applied potential.[285] These thin films can be used as molecular switches,[286,287] bias-switchable permselectivity anions membranes,[279] and electrocatalysts for OER,[283,288] HER,[289,290] and CO_2 reduction.[291] Among these applications, electrocatalytic OER and HER are of interest since electrocatalytic water splitting can provide a much more sustainable and carbon-neutral route for energy generation. The intermittent nature of renewable power sources is a common problem for the technology design of energy-storage devices. Electrochemical water splitting is a promising pathway to overcome this because it produces the energy-dense and clean-burning fuel hydrogen. In such a scenario, intermittent energies such as wind and solar can be used to generate electricity, and when available drive the splitting of water at electrocatalyst electrodes in electrolyzers.[292] Noh *et al.*[289] anchored molybdenum sulfide (MoS_x) in NU-1000 *via* SIM (MoS_x-SIM) to support multiple catalyst active sites for electrocatalytic HER. MoS_x-SIM presented a low electrocatalytic HER activity in electrode-supported thin-film form, due to the insulating nature of the thin film MOF which leaves the catalytic sites electrochemically isolated from the underlying electrode. To overcome such limitation, molecular viologen-type redox mediators were included to effectively diffuse in the MOF and to deliver the electrons from the underlying electrode to the MoS_x catalytic units. Mechanistic studies showed that overall control of the rate of catalysis can be defined by mediator-to-catalyst electron transfer, solution-to-catalyst proton transfer, or both.[289,290] Kung *et al.*[283] performed the chemical growth of uniform thin films of NU-1000 on transparent fluorine-doped tin oxide (FTO) conducting glass, followed by the deposition of Co(II) ions, resulting in the oxidation catalyst Co-AIM NU-1000. Cyclic voltammetric (CV) experiments showed that Co-AIM-NU-1000 is electrochemically active. The charge transfer occurred by hole hopping through the repeating pyrene units, meanwhile the counterions can diffuse through the regular channels for the neutralization of the charges formed on the linkers. The pH was found to be important for the oxidation efficiency as the material electrocatalyzes the four-electron conversion of hydroxide ion to dioxygen at pH = 11 while it shows a poor activity at pH = 8.2, 9, and 10.

3.6 Bio-medical applications

MOFs have emerged in the field of bio-medicine applications. They are of particular interest because of their crystal porosity, tunable functionalities and properties, and availability to encapsulate molecules.[293] Pyrene-based MOFs have also been envisioned and conceived as smart materials for biological applications. The luminescence properties of pyrene-based MOFs is one of the attractive properties for the detection of biomarkers related to diseases.[87,166,173] The advantage of these MOFs based sensors is that they can be implemented as MOF-coated paper test strips.[166] The optical properties of pyrene-based MOFs have also been considered as an X-ray computed tomography (CT) contrast agent. Robison *et al.*[92] reported *in vitro* studies of a bismuth pyrene MOF (Bi-NU-901), showing ~7 times better contrast intensity compared to that of a zirconium MOF (NU-901) with the same topology and ~14 times better contrast than a commercially available CT contrast agent. Their results are of interest to bio-imaging applications for clinical tests given the need to have agents with the lowest dose possible, maximum contrast between tissue and background, and minimal toxicity. In this case, Bi-NU-901 could require much less material compared to contrast agents in current use.[92] Another optical property of pyrene-based MOFs has been used in the field of photodynamic therapy, where the capability of singlet generation can be use to kill cancerous and precancerous cells after light activation.[294] Zhao *et al.*[294] designed pyrene-based MOF nanoparticles as a photodynamic therapy nanoplatform. The material is made from NU-1000 mixed with TCPP *via* ligand substitution, subsequently, its surface is functionalized with poly-(ethylene glycol) (PEG) and folic acid for biocompatibility and tumor targeting effect,

respectively. The MOF nanoparticles could generate reactive oxygen species under 650 nm laser irradiation efficiently. The nanoparticles displayed low toxicity and good photodynamic effect with antitumor efficacy *in vitro* and *in vivo* experiments.[294]

The natural crystalline porosity of MOFs has attracted the attention for the development of new and efficient drug delivery systems.[296] Drug delivery systems are devices that enable a therapeutic substance to selectively reach its site of action without reaching the non-target cell, organs, or tissues. Such devices should accomplish a controlled and sustained release of the medicine, to minimize side effects and ensure the efficacy of the pharmaceutical upon reaching the desired target.[297] MOFs are promising for this biomedical application since they can be modified to acquired functionalities to give biostability, target selectivity, and encapsulation of the cargo.[61] There has been recent progress in using pyrene-MOFs as promising drug delivery systems. This includes applications like insulin delivery,[298,299] and chemotherapy treatments.[295,297,300,301] MOFs bring different advantages over traditional pharmaceuticals. In the case of oral insulin delivery nanocarriers, MOFs can exhibit higher insulin loading capacities as a result of their porosity. Chen *et al.*[298] immobilised insulin in NU-1000 obtaining a high loading of ~40 wt% in only 30 min. The pore topology and dimensionality allow the effective diffusion of insulin through the framework, and also exclude digestive insulin enzymes like pepsin under simulated stomach environment conditions. Most importantly, the nanocarriers exhibit the controlled release under conditions mimicking the delivery target point. These last features of selective target and controlled release are of great interest to cancer treatment applications. Zhao *et al.*[295] synthesized PEG NU-1000 MOF for the encapsulation of an anticancer drug Doxorubicin (DOX) (Fig. 12). The material DOX@NU-1000@PEG displayed good biocompatibility and could inhibit tumor growth efficiently with a long-time release behavior for over 2 weeks. On the other hand, in some cases, it is necessary to control the release kinetics as in the case of 5-fluorouracil (5-FU) for breast cancer treatment. Hu *et al.*[301] synthesized a Mg pyrene-based MOF (TDL-Mg) with suitable host–guest interactions with 5-FU, leading to a medically reasonable sustained release rate and curative effect on HeLa cancer cells. Likewise, the advantage of using a pyrene-based MOF like TDL-Mg is thanks to the natural fluorescent properties which were also exploited to monitored the 5-FU release using the "turn-on" fluorescence mechanism.

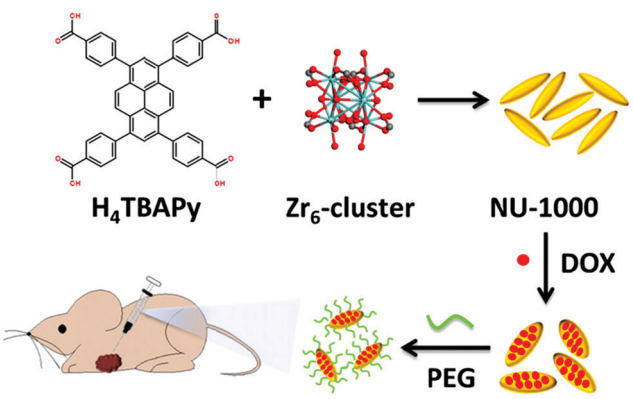

Fig. 12 Preparation and application of NU-1000 nanoparticles for chemotherapy. Doxorubicin (DOX) molecules are encapsulated in the NU-1000 nanoparticles and functionalized with polyethylene glycol (PEG). Reprinted with permission from ref. 295.

4 Concluding remarks and future prospects

Pyrene-based MOFs have attracted attention in different research fields as mentioned previously, given the promising structural, optical, and electronic properties of the pyrene moiety. Up to date, more than 20 different pyrene-based ligands have been combined with different metals (from transition metals to lanthanides), resulting in well-defined structures with varying structural characteristics such as porosity, pore size, and topology, which are the key components in many applications mentioned in this review. Pore surface engineering using post-modification methods (such as AIM, SIM, and SALI) has encouraged researchers to decorate metal nodes with various single metal sites, metal clusters, and linkers, resulting in the desired functionalization of the structures for target applications.

There have been numerous attempts for synthesizing novel pyrene-based molecules, in addition to the studies exploring their combination with metals in coordination complexes. Nevertheless, pyrene-based MOFs are one of the relatively new subsets of the extensive MOF-related research studies. The curiosity on pyrene-based MOFs has increased tremendously with the continued development of novel pyrene-based ligands over the past few years. However, the challenges faced throughout the synthesis of pyrene derivatives (mainly during the coupling reactions), as well as in the prediction of the coordination environment of the pyrene-based ligands are still the main difficulties. Therefore, the research is still at an early stage in terms of the variety of pyrene linker structures and the number of reported pyrene-based MOFs. Most of the pyrene-based organic ligands rely on similar chemistry, where pyrene core is decorated with benzene-derivatives with different functionalities (mostly carboxylates) at -1, -3, -6 and -8 positions. Hence, the effect of different electrophilic aromatic substitutions on the coordination with metals should be unveiled by concentrating more on the ligand design. For example, electron-donating groups such as pyrazole or thiol can be considered as the next-step functionalization on the pyrene core, resulting in a novel MOF chemistry based on the interactions with metal nodes.

It is not easy to predict the resulting MOF structure as the MOF synthesis is complicated with too many variables and this is valid for all different MOF families. Therefore, the relationship between the synthesis conditions and the resulting topologies of MOFs are still not well understood. Different experimental protocols can lead to well distinctive topological MOF structures, despite the starting precursors are the same ligand and transition metal element. Therefore, there is a need for the fundamental

understanding of the effect of different synthetic routes for the development of new MOFs with the same metal chemistry, as in the case of Zn-TBAPy MOFs. Pyrene-based MOFs is a good platform for the systematic investigation of the effect of reaction conditions on the resulting structures thanks to the possibility of synthesizing a significant number of structures with promising physicochemical features. Machine learning tools can be exploited to capture the importance of the synthesis parameters to gain a better understanding of pyrene-based MOF synthesis conditions and pay a better experimental design and optimal synthesis conditions. Consequently, computational hypothetical MOF generation and screening strategies can expand the library of pyrene-based MOFs that can lead the experimental attempts in the right direction. Such studies can lead to the prediction of crucial characteristics, such as the optical properties, surface chemistry, and pore shape required for target specific applications.

Conflicts of interest

There are no conflicts to declare.

Acknowledgements

This work has been supported by the National Centre of Competence in Research (NCCR) Materials' Revolution: Computational Design and Discovery of Novel Materials (MARVEL) of the Swiss National Science Foundation (SNSF) and the Swiss National Supercomputing Centre (CSCS) under project ID s1005. A. O.-G. acknowledges the financial support of the Swiss National Science Foundation (SNSF) under Grant 200021_172759. D. O. was supported by the European Research Council (ERC) under the European Union's Horizon 2020 research and innovation programme (grant agreement No. 666983, MaGic).

References

1 X. Feng, J. Hu, C. Redshaw and T. Yamato, *Chem. – Eur. J.*, 2016, **22**, 11898–11916.
2 R. Haldar, L. Heinke and C. Wöll, *Adv. Mater.*, 2020, **32**, 1905227.
3 A. Laurent, *Ann. Chim. Phys.*, 1837, **66**, 136–137.
4 T. M. Figueira-Duarte and K. Mullen, *Chem. Rev.*, 2011, **111**, 7260–7314.
5 D. Zych, *Molecules*, 2019, **24**, 2551.
6 A. J. Howarth, M. B. Majewski and M. O. Wolf, *Coord. Chem. Rev.*, 2015, **282**, 139–149.
7 B. J. Burnett, P. M. Barron and W. Choe, *CrystEngComm*, 2012, **14**, 3839–3846.
8 N. U. Day, C. C. Wamser and M. G. Walter, *Polym. Int.*, 2015, **64**, 833–857.
9 C. F. Pereira, M. M. Simões, J. P. Tomé and F. A. Almeida, Paz, *Molecules*, 2016, **21**, 1348.
10 J. M. Casas-Solvas, J. D. Howgego and A. P. Davis, *Org. Biomol. Chem.*, 2014, **12**, 212–232.
11 E. Manandhar and K. J. Wallace, *Inorg. Chim. Acta*, 2012, **381**, 15–43.
12 K. C. Stylianou, R. Heck, S. Y. Chong, J. Bacsa, J. T. A. Jones, Y. Z. Khimyak, D. Bradshaw and M. J. Rosseinsky, *J. Am. Chem. Soc.*, 2010, **132**, 4119–4130.
13 M. Eddaoudi, J. Kim, N. Rosi, D. Vodak, J. Wachter, M. O'Keeffe and O. M. Yaghi, *Science*, 2002, **295**, 469–472.
14 L.-M. Yang, P. Ravindran, P. Vajeeston and M. Tilset, *Phys. Chem. Chem. Phys.*, 2012, **14**, 4713–4723.
15 T. Kuroda-Sowa, M. Munakata and H. Matsuda, S.-i. Akiyama and M. Maekawa, *J. Chem. Soc., Dalton Trans.*, 1995, 2201–2208.
16 L. Tchertanov and C. Pascard, *Acta Crystallogr., Sect. B: Struct. Sci.*, 1997, **53**, 904–915.
17 F. H. Herbstein, *Acta Crystallogr., Sect. B: Struct. Sci.*, 2001, **57**, 517–519.
18 R. Sekiya and S.-i. Nishikiori, *Chem. Commun.*, 2001, 2612–2613.
19 B. D. Wagner, G. J. McManus, B. Moulton and M. J. Zaworotko, *Chem. Commun.*, 2002, 2176–2177.
20 T. Kuroda-Sowa, S. Q. Liu, Y. Yamazaki, M. Munakata, M. Maekawa, Y. Suenaga, H. Konaka and H. Nakagawa, *Inorg. Chem.*, 2005, **44**, 1686–1692.
21 R. Sekiya, S.-i. Nishikiori and K. Ogura, *Inorg. Chem.*, 2006, **45**, 9233–9244.
22 G. J. McManus, J. J. Perry, M. Perry, B. D. Wagner and M. J. Zaworotko, *J. Am. Chem. Soc.*, 2007, **129**, 9094–9101.
23 Q. Wang, J. Zhang, C.-F. Zhuang, Y. Tang and C.-Y. Su, *Inorg. Chem.*, 2009, **48**, 287–295.
24 L. Rajput and K. Biradha, *CrystEngComm*, 2009, **11**, 1220.
25 R. Sekiya, S.-i. Nishikiori and R. Kuroda, *CrystEngComm*, 2009, **11**, 2251.
26 L. Rajput and K. Biradha, *New J. Chem.*, 2010, **34**, 2415.
27 R. Sekiya and S.-i. Nishikiori, *Chem. Commun.*, 2012, **48**, 5022.
28 G. Mukherjee and K. Biradha, *Chem. Commun.*, 2012, **48**, 4293.
29 M. Nishio, N. Motokawa, M. Takemura and H. Miyasaka, *Dalton Trans.*, 2013, **42**, 15898.
30 G. Mukherjee and K. Biradha, *Cryst. Growth Des.*, 2014, **14**, 419–422.
31 J.-W. Ye, H.-L. Zhou, S.-Y. Liu, X.-N. Cheng, R.-B. Lin, X.-L. Qi, J.-P. Zhang and X.-M. Chen, *Chem. Mater.*, 2015, **27**, 8255–8260.
32 A. C. Tella, O. A. Ameen, P. A. Ajibade and L. O. Alimi, *J. Porous Mater.*, 2015, **22**, 1599–1605.
33 T. Delgado, M. Meneses-Sánchez, L. Piñeiro-López, C. Bartual-Murgui, M. C. Muñoz and J. A. Real, *Chem. Sci.*, 2018, **9**, 8446–8452.
34 H.-R. Fu, X.-X. Wu, L.-F. Ma, F. Wang and J. Zhang, *ACS Appl. Mater. Interfaces*, 2018, **10**, 18012–18020.
35 D. Shen, G. Wang, Z. Liu, P. Li, K. Cai, C. Cheng, Y. Shi, J.-M. Han, C.-W. Kung, X. Gong, Q.-H. Guo, H. Chen, A. C.-H. Sue, Y. Y. Botros, A. Facchetti, O. K. Farha, T. J. Marks and J. F. Stoddart, *J. Am. Chem. Soc.*, 2018, **140**, 11402–11407.

36 L. Zhao, J. Yang, M. Gong, Y. Zhang and J. Gu, *J. Mater. Chem. C*, 2020, **8**, 3904–3913.
37 M. Meneses-Sánchez, L. Piñeiro-López, T. Delgado, C. Bartual-Murgui, M. C. Muñoz, P. Chakraborty and J. A. Real, *J. Mater. Chem. C*, 2020, **8**, 1623–1633.
38 J. X. Li, Q. L. Guan, Y. Wang, Z. X. You, Y. H. Xing, F. Y. Bai and L. X. Sun, *New J. Chem.*, 2020, **44**, 1446–1454.
39 R. Dalapati, S. Nandi and S. Biswas, *Dalton Trans.*, 2020, **49**, 8684–8692.
40 A. J. Blake, N. R. Champness, A. N. Khlobystov, D. A. Lemenovskii, W.-S. Li and M. Schröder, *Chem. Commun.*, 1997, 1339–1340.
41 A. J. Blake, G. Baum, N. R. Champness, S. S. M. Chung, P. A. Cooke, D. Fenske, A. N. Khlobystov, D. A. Lemenovskii, W.-S. Li and M. Schröder, *J. Chem. Soc., Dalton Trans.*, 2000, 4285–4291.
42 G. L. Ning, L. P. Wu, K. Sugimoto, M. Munakata, T. Kuroda-Sowa and M. Maekawa, *J. Chem. Soc., Dalton Trans.*, 1999, 2529–2536.
43 N. L. Rosi, J. Kim, M. Eddaoudi, B. Chen, M. O'Keeffe and O. M. Yaghi, *J. Am. Chem. Soc.*, 2005, **127**, 1504–1518.
44 F.-F. Li, J.-F. Ma, S.-Y. Song, J. Yang, Y.-Y. Liu and Z.-M. Su, *Inorg. Chem.*, 2005, **44**, 9374–9383.
45 C. A. Williams, A. J. Blake, C. Wilson, P. Hubberstey and M. Schröder, *Cryst. Growth Des.*, 2008, **8**, 911–922.
46 G. Huang, Y.-Q. Sun, Z. Xu, M. Zeller and A. D. Hunter, *Dalton Trans.*, 2009, 5083–5093.
47 C.-C. Tsai, T.-T. Luo, J.-F. Yin, H.-C. Lin and K.-L. Lu, *Inorg. Chem.*, 2009, **48**, 8650–8652.
48 J. Hu, M.-H. Nguyen and J. H. Yip, *Inorg. Chem.*, 2011, **50**, 7429–7439.
49 N. Zhao, F. Sun, H. He, J. Jia and G. Zhu, *Cryst. Growth Des.*, 2014, **14**, 1738–1743.
50 T. C. Wang, W. Bury, D. A. Gómez-Gualdrón, N. A. Vermeulen, J. E. Mondloch, P. Deria, K. Zhang, P. Z. Moghadam, A. A. Sarjeant, R. Q. Snurr, J. F. Stoddart, J. T. Hupp and O. K. Farha, *J. Am. Chem. Soc.*, 2015, **137**, 3585–3591.
51 S. S. Park, C. H. Hendon, A. J. Fielding, A. Walsh, M. OKeeffe and M. Dincă, *J. Am. Chem. Soc.*, 2017, **139**, 3619–3622.
52 M. Roy, A. A. Lonardo, D. N. Pham, A. Kreider-Mueller, J. A. Golen and D. R. Manke, *CrystEngComm*, 2019, **21**, 4255–4257.
53 J. M. Taylor, R. Vaidhyanathan, S. S. Iremonger and G. K. Shimizu, *J. Am. Chem. Soc.*, 2012, **134**, 14338–14340.
54 S. B. Kalidindi, S. Nayak, M. E. Briggs, S. Jansat, A. P. Katsoulidis, G. J. Miller, J. E. Warren, D. Antypov, F. Corà, B. Slater, M. R. Prestly, C. Martí-Gastaldo and M. J. Rosseinsky, *Angew. Chem., Int. Ed.*, 2015, **54**, 221–226.
55 C. Dong, J. Bai, X.-L. Lv, W. Wu, J. Lv and J.-R. Li, *Inorg. Chem.*, 2019, **58**, 15909–15916.
56 L. Robison, R. J. Drout, L. R. Redfern, F. A. Son, M. C. Wasson, S. Goswami, Z. Chen, A. Olszewski, K. B. Idrees, T. Islamoglu and O. K. Farha, *Chem. Mater.*, 2020, **32**, 3545–3552.
57 R.-J. Li, M. Li, X.-P. Zhou, S. W. Ng, M. O'Keeffe and D. Li, *CrystEngComm*, 2014, **16**, 6291–6295.
58 Y. Xiao, Y. Qi, X. Wang, X. Wang, F. Zhang and C. Li, *Adv. Mater.*, 2018, **30**, 1803401.
59 X. Zeng, R. Liu, D. Liu, Q. Liu and Y. Wang, *Z. Anorg. Allg. Chem.*, 2019, **645**, 1379–1383.
60 K. C. Stylianou, J. Rabone, S. Y. Chong, R. Heck, J. Armstrong, P. V. Wiper, K. E. Jelfs, S. Zlatogorsky, J. Bacsa, A. G. McLennan, C. P. Ireland, Y. Z. Khimyak, K. M. Thomas, D. Bradshaw and M. J. Rosseinsky, *J. Am. Chem. Soc.*, 2012, **134**, 20466–20478.
61 A. V. Vinogradov, H. Zaake-Hertling, A. S. Drozdov, P. Lönnecke, G. A. Seisenbaeva, V. G. Kessler, V. V. Vinogradov and E. Hey-Hawkins, *Chem. Commun.*, 2015, **51**, 17764–17767.
62 J.-H. Qin, Y.-D. Huang, Y. Zhao, X.-G. Yang, F.-F. Li, C. Wang and L.-F. Ma, *Inorg. Chem.*, 2019, **58**, 15013–15016.
63 R. Seetharaj, P. Vandana, P. Arya and S. Mathew, *Arab. J. Chem.*, 2019, **12**, 295–315.
64 F. P. Kinik, A. Ortega-Guerrero, D. Ongari, C. P. Ireland and B. Smit, *Mater. Cloud Archive*, 2020, **156**, 2020, DOI: 10.24435/materialscloud:z5-ct.
65 G. Ayoub, M. Arhangelskis, X. Zhang, F. Son, T. Islamoglu, T. Friščić and O. K. Farha, *Beilstein J. Nanotechnol.*, 2019, **10**, 2422–2427.
66 A. García-García, I. Oyarzabal, J. Cepeda, J. M. Seco, A. A. García-Valdivia, S. Gómez-Ruiz, A. Salinas-Castillo, D. Choquesillo-Lazarte and A. Rodríguez-Diéquez, *New J. Chem.*, 2018, **42**, 832–837.
67 J. Park and M. Oh, *CrystEngComm*, 2016, **18**, 8372–8376.
68 Y.-L. Huang, Y.-N. Gong, L. Jiang and T.-B. Lu, *Chem. Commun.*, 2013, **49**, 1753–1755.
69 Y.-L. Huang, L. Jiang and T.-B. Lu, *ChemPlusChem*, 2016, **81**, 780.
70 Y.-L. Huang, D.-C. Zhong, L. Jiang, Y.-N. Gong and T.-B. Lu, *Inorg. Chem.*, 2017, **56**, 705–708.
71 L. Hu, X.-J. Hong, X.-M. Lin, J. Lin, Q.-X. Cheng, B. Lokesh and Y.-P. Cai, *Cryst. Growth Des.*, 2018, **18**, 7088–7093.
72 R. R. Maldonado, X. Zhang, S. Hanna, X. Gong, N. C. Gianneschi, J. T. Hupp and O. K. Farha, *Dalton Trans.*, 2020, **49**, 6553–6556.
73 H. Alawisi, B. Li, Y. He, H. D. Arman, A. M. Asiri, H. Wang and B. Chen, *Cryst. Growth Des.*, 2014, **14**, 2522–2526.
74 J. E. Mondloch, W. Bury, D. Fairen-Jimenez, S. Kwon, E. J. DeMarco, M. H. Weston, A. A. Sarjeant, S. T. Nguyen, P. C. Stair, R. Q. Snurr, O. K. Farha and J. T. Hupp, *J. Am. Chem. Soc.*, 2013, **135**, 10294–10297.
75 C.-W. Kung, T. C. Wang, J. E. Mondloch, D. Fairen-Jimenez, D. M. Gardner, W. Bury, J. M. Klingsporn, J. C. Barnes, R. Van Duyne, J. F. Stoddart, M. R. Wasielewski, O. K. Farha and J. T. Hupp, *Chem. Mater.*, 2013, **25**, 5012–5017.
76 K. C. Stylianou, J. Bacsa, D. Bradshaw and M. J. Rosseinsky, *Z. Anorg. Allg. Chem.*, 2014, **640**, 2123–2131.
77 R.-J. Li, M. Li, X.-P. Zhou, D. Li and M. O'Keeffe, *Chem. Commun.*, 2014, **50**, 4047–4049.

78 O. Karagiaridi, W. Bury, D. Fairen-Jimenez, C. E. Wilmer, A. A. Sarjeant, J. T. Hupp and O. K. Farha, *Inorg. Chem.*, 2014, **53**, 10432–10436.
79 P. Li, N. A. Vermeulen, X. Gong, C. D. Malliakas, J. F. Stoddart, J. T. Hupp and O. K. Farha, *Angew. Chem., Int. Ed.*, 2016, **55**, 10358–10362.
80 K. C. Park, C. Seo, G. Gupta, J. Kim and C. Y. Lee, *ACS Appl. Mater. Interfaces*, 2017, **9**, 38670–38677.
81 J. Ai, F.-Y. Chen, C.-Y. Gao, H.-R. Tian, Q.-J. Pan and Z.-M. Sun, *Inorg. Chem.*, 2018, **57**, 4419–4426.
82 L. Guo, M. Wang and D. Cao, *Small*, 2018, **14**, 1703822.
83 A. Gładysiak, T. N. Nguyen, R. Bounds, A. Zacharia, G. Itskos, J. A. Reimer and K. C. Stylianou, *Chem. Sci.*, 2019, **10**, 6140–6148.
84 S. L. Anderson, P. G. Boyd, A. Gładysiak, T. N. Nguyen, R. G. Palgrave, D. Kubicki, L. Emsley, D. Bradshaw, M. J. Rosseinsky, B. Smit and K. C. Stylianou, *Nat. Commun.*, 2019, **10**, 1–8.
85 P. G. Boyd, A. Chidambaram, E. García-Díez, C. P. Ireland, T. D. Daff, R. Bounds, A. Gładysiak, P. Schouwink, S. M. Moosavi, M. M. Maroto-Valer, J. A. Reimer, A. R. Navarro, T. K. Woo, S. Garcia, K. C. Stylianou and B. Smit, *Nature*, 2019, **576**, 253–256.
86 Y. Xiao, X. Guo, J. Liu, L. Liu, F. Zhang and C. Li, *Chin. J. Catal.*, 2019, **40**, 1339–1344.
87 Q. L. Guan, Y. H. Xing, J. Liu, C. Han, C. Y. Hou and F. Y. Bai, *J. Phys. Chem. C*, 2019, **123**, 23287–23296.
88 T. N. Tu, H. T. T. Nguyen, H. T. D. Nguyen, M. V. Nguyen, T. D. Nguyen, N. T. Tran and K. T. Lim, *RSC Adv.*, 2019, **9**, 16784–16789.
89 Y. Hasegawa, T. Matsui, Y. Kitagawa, T. Nakanishi, T. Seki, H. Ito, Y. Nakasaka, T. Masuda and K. Fushimi, *Chem. – Eur. J.*, 2019, **25**, 12308–12315.
90 R. Liu, Q.-Y. Liu, R. Krishna, W. Wang, C.-T. He and Y.-L. Wang, *Inorg. Chem.*, 2019, **58**, 5089–5095.
91 A. Gładysiak, T. N. Nguyen, M. Spodaryk, J. Lee, J. B. Neaton, A. Züttel and K. C. Stylianou, *Chem. – Eur. J.*, 2019, **25**, 501–506.
92 L. Robison, L. Zhang, R. J. Drout, P. Li, C. R. Haney, A. Brikha, H. Noh, B. L. Mehdi, N. D. Browning, V. P. Dravid, Q. Cui, T. Islamoglu and O. K. Farha, *ACS Appl. Bio Mater.*, 2019, **2**, 1197–1203.
93 Y.-L. Huang, P.-L. Qiu, H. Zeng, H. Liu, D. Luo, Y. Y. Li, W. Lu and D. Li, Eur, *J. Inorg. Chem.*, 2019, 4205–4210.
94 Y.-L. Huang, P.-L. Qiu, J.-P. Bai, D. Luo, W. Lu and D. Li, *Inorg. Chem.*, 2019, **58**, 7667–7671.
95 Y.-D. Huang, J.-H. Qin, X.-G. Yang, H.-R. Wang, F.-F. Li and L.-F. Ma, *J. Solid State Chem.*, 2020, **285**, 121252.
96 Z. Hu, C. Qiao, Z. Xia, F. Li, J. Han, Q. Wei, Q. Yang, G. Xie, S. Chen and S. Gao, *ACS Appl. Mater. Interfaces*, 2020, **12**, 14914–14923.
97 A. Cadiau, N. Kolobov, S. Srinivasan, M. G. Goesten, H. Haspel, A. V. Bavykina, M. R. Tchalala, P. Maity, A. Goryachev, A. S. Poryvaev, M. Eddaoudi, M. V. Fedin, O. F. Mohammed and J. Gascon, *Angew. Chem., Int. Ed.*, 2020, **32**, 97–104.
98 S. Sudan, A. Gładysiak, B. Valizadeh, J.-H. Lee and K. C. Stylianou, *Inorg. Chem.*, 2020, **59**, 9029–9036.
99 S. Xie, H. Wang, Z. Liu, R. Dai and L. Huang, *RSC Adv.*, 2015, **5**, 7121–7124.
100 W.-Y. Gao, S. Palakurty, L. Wojtas, Y.-S. Chen and S. Ma, *Inorg. Chem. Front.*, 2015, **2**, 369–372.
101 N. Zhao, F. Sun, S. Zhang, H. He, J. Liu, Q. Li and G. Zhu, *Inorg. Chem.*, 2015, **54**, 65–68.
102 N. Zhao, F. Sun, N. Zhang and G. Zhu, *Cryst. Growth Des.*, 2017, **17**, 2453–2457.
103 P. Chandrasekhar, A. Mukhopadhyay, G. Savitha and J. N. Moorthy, *Chem. Sci.*, 2016, **7**, 3085–3091.
104 P. Li, S.-Y. Moon, M. A. Guelta, L. Lin, D. A. Gómez-Gualdrón, R. Q. Snurr, S. P. Harvey, J. T. Hupp and O. K. Farha, *ACS Nano*, 2016, **10**, 9174–9182.
105 O. V. Gutov, W. Bury, D. A. Gomez-Gualdron, V. Krungleviciute, D. Fairen-Jimenez, J. E. Mondloch, A. A. Sarjeant, S. S. Al-Juaid, R. Q. Snurr, J. T. Hupp, T. Yildirim and O. K. Farha, *Chem. – Eur. J.*, 2014, **20**, 12389–12393.
106 A. Bajpai, A. Mukhopadhyay, M. S. Krishna, S. Govardhan and J. N. Moorthy, *IUCrJ*, 2015, **2**, 552–562.
107 P. Li, Q. Chen, T. C. Wang, N. A. Vermeulen, B. L. Mehdi, A. Dohnalkova, N. D. Browning, D. Shen, R. Anderson, D. A. Gómez-Gualdrón, F. M. Cetin, J. Jagiello, A. M. Asiri, J. F. Stoddart and O. K. Farha, *Chemistry*, 2018, **4**, 1022–1034.
108 P. Deria, D. A. Gómez-Gualdrón, W. Bury, H. T. Schaef, T. C. Wang, P. K. Thallapally, A. A. Sarjeant, R. Q. Snurr, J. T. Hupp and O. K. Farha, *J. Am. Chem. Soc.*, 2015, **137**, 13183–13190.
109 R. Zou, X. Ren, F. Huang, Y. Zhao, J. Liu, X. Jing, F. Liao, Y. Wang, J. Lin, R. Zou and J. Sun, *J. Mater. Chem. A*, 2015, **3**, 23493–23500.
110 Y. Zhang, J. Pang, J. Li, X. Yang, M. Feng, P. Cai and H.-C. Zhou, *Chem. Sci.*, 2019, **10**, 8455–8460.
111 J. Ye, L. Gagliardi, C. J. Cramer and D. G. Truhlar, *J. Catal.*, 2017, **354**, 278–286.
112 T. C. Wang, N. A. Vermeulen, I. S. Kim, A. B. F. Martinson, J. F. Stoddart, J. T. Hupp and O. K. Farha, *Nat. Protoc.*, 2016, **11**, 149.
113 L. C. Gallington, I. S. Kim, W.-G. Liu, A. A. Yakovenko, A. E. Platero-Prats, Z. Li, T. C. Wang, J. T. Hupp, O. K. Farha, D. G. Truhlar, A. B. F. Martinson and K. W. Chapman, *J. Am. Chem. Soc.*, 2016, **138**, 13513–13516.
114 T. E. Webber, W.-G. Liu, S. P. Desai, C. C. Lu, D. G. Truhlar and R. L. Penn, *ACS Appl. Mater. Interfaces*, 2017, **9**, 39342–39346.
115 F. Cheng, E. S. Marshall, A. J. Young, P. J. Robinson, J.-S. G. Bouillard, A. M. Adawi, N. A. Vermeulen, O. K. Farha, M. R. Reithofer and J. M. Chin, *Chem. – Eur. J.*, 2017, **23**, 15578–15582.
116 T. Islamoglu, K.-i. Otake, P. Li, C. T. Buru, A. W. Peters, I. Akpinar, S. J. Garibay and O. K. Farha, *CrystEngComm*, 2018, **20**, 5913–5918.
117 T. E. Webber, S. P. Desai, R. L. Combs, S. Bingham, C. C. Lu and R. L. Penn, *Cryst. Growth Des.*, 2020, **20**, 2965–2972.

118 J. E. Mondloch, M. J. Katz, N. Planas, D. Semrouni, L. Gagliardi, J. T. Hupp and O. K. Farha, *Chem. Commun.*, 2014, **50**, 8944.
119 S. Yuan, J. Peng, Y. Zhang and Y. Shao-Horn, *J. Phys. Chem. C*, 2019, **123**, 28266–28274.
120 X.-P. Wu, L. Gagliardi and D. G. Truhlar, *Phys. Chem. Chem. Phys.*, 2018, **20**, 1778–1786.
121 N. Planas, J. E. Mondloch, S. Tussupbayev, J. Borycz, L. Gagliardi, J. T. Hupp, O. K. Farha and C. J. Cramer, *J. Phys. Chem. Lett.*, 2014, **5**, 3716–3723.
122 R. C. Klet, Y. Liu, T. C. Wang, J. T. Hupp and O. K. Farha, *J. Mater. Chem. A*, 2016, **4**, 1479–1485.
123 D. Yang, V. Bernales, T. Islamoglu, O. K. Farha, J. T. Hupp, C. J. Cramer, L. Gagliardi and B. C. Gates, *J. Am. Chem. Soc.*, 2016, **138**, 15189–15196.
124 W.-G. Liu and D. G. Truhlar, *Chem. Mater.*, 2017, **29**, 8073–8081.
125 H. García and S. Navalón, *Metal–Organic Frameworks: Applications in Separations and Catalysis*, John Wiley & Sons, Ltd, Weinheim, Germany, 2018.
126 R. C. Klet, T. C. Wang, L. E. Fernandez, D. G. Truhlar, J. T. Hupp and O. K. Farha, *Chem. Mater.*, 2016, **28**, 1213–1219.
127 C.-W. Kung, J. E. Mondloch, T. C. Wang, W. Bury, W. Hoffeditz, B. M. Klahr, R. C. Klet, M. J. Pellin, O. K. Farha and J. T. Hupp, *ACS Appl. Mater. Interfaces*, 2015, **7**, 28223–28230.
128 A. W. Peters, Z. Li, O. K. Farha and J. T. Hupp, *ACS Nano*, 2015, **9**, 8484–8490.
129 Z. Li, A. W. Peters, V. Bernales, M. A. Ortuño, N. M. Schweitzer, M. R. DeStefano, L. C. Gallington, A. E. Platero-Prats, K. W. Chapman, C. J. Cramer, L. Gagliardi, J. T. Hupp and O. K. Farha, *ACS Cent. Sci.*, 2017, **3**, 31–38.
130 P. Deria, J. E. Mondloch, E. Tylianakis, P. Ghosh, W. Bury, R. Q. Snurr, J. T. Hupp and O. K. Farha, *J. Am. Chem. Soc.*, 2013, **135**, 16801–16804.
131 P. Deria, W. Bury, J. T. Hupp and O. K. Farha, *Chem. Commun.*, 2014, **50**, 1965–1968.
132 P. Deria, W. Bury, I. Hod, C.-W. Kung, O. Karagiaridi, J. T. Hupp and O. K. Farha, *Inorg. Chem.*, 2015, **54**, 2185–2192.
133 R. W. Johnson, A. Hultqvist and S. F. Bent, *Mater. Today*, 2014, **17**, 236–246.
134 T. Islamoglu, S. Goswami, Z. Li, A. J. Howarth, O. K. Farha and J. T. Hupp, *Acc. Chem. Res.*, 2017, **50**, 805–813.
135 Z. Li, N. M. Schweitzer, A. B. League, V. Bernales, A. W. Peters, A. B. Getsoian, T. C. Wang, J. T. Miller, A. Vjunov, J. L. Fulton, J. A. Lercher, C. J. Cramer, L. Gagliardi, J. T. Hupp and O. K. Farha, *J. Am. Chem. Soc.*, 2016, **138**, 1977–1982.
136 I. S. Kim, J. Borycz, A. E. Platero-Prats, S. Tussupbayev, T. C. Wang, O. K. Farha, J. T. Hupp, L. Gagliardi, K. W. Chapman, C. J. Cramer and A. B. F. Martinson, *Chem. Mater.*, 2015, **27**, 4772–4778.
137 A. E. Platero-Prats, A. B. League, V. Bernales, J. Ye, L. C. Gallington, A. Vjunov, N. M. Schweitzer, Z. Li, J. Zheng, B. L. Mehdi, A. J. Stevens, A. Dohnalkova, M. Balasubramanian, O. K. Farha, J. T. Hupp, N. D. Browning, J. L. Fulton, D. M. Camaioni, J. A. Lercher, D. G. Truhlar, L. Gagliardi, C. J. Cramer and K. W. Chapman, *J. Am. Chem. Soc.*, 2017, **139**, 10410–10418.
138 A. Halder, S. Lee, B. Yang, M. J. Pellin, S. Vajda, Z. Li, Y. Yang, O. K. Farha and J. T. Hupp, *J. Chem. Phys.*, 2020, **152**, 084703.
139 J. M. Lownsbury, I. A. Santos-López, W. Zhang, C. T. Campbell, H. S. Yu, W.-G. Liu, C. J. Cramer, D. G. Truhlar, T. Wang, J. T. Hupp and O. K. Farha, *J. Phys. Chem. C*, 2016, **120**, 16850–16862.
140 C. T. Lollar, J.-S. Qin, J. Pang, S. Yuan, B. Becker and H.-C. Zhou, *Langmuir*, 2018, **34**, 13795–13807.
141 Y. Cui, M. Rimoldi, A. E. Platero-Prats, K. W. Chapman, J. T. Hupp and O. K. Farha, *ChemCatChem*, 2018, **10**, 1772–1777.
142 H. Noh, Y. Cui, A. W. Peters, D. R. Pahls, M. A. Ortuño, N. A. Vermeulen, C. J. Cramer, L. Gagliardi, J. T. Hupp and O. K. Farha, *J. Am. Chem. Soc.*, 2016, **138**, 14720–14726.
143 H. Noh, C.-W. Kung, K.-I. Otake, A. W. Peters, Z. Li, Y. Liao, X. Gong, O. K. Farha and J. T. Hupp, *ACS Catal.*, 2018, **8**, 9848–9858.
144 C.-W. Kung, C. O. Audu, A. W. Peters, H. Noh, O. K. Farha and J. T. Hupp, *ACS Energy Lett.*, 2017, **2**, 2394–2401.
145 K.-i. Otake, Y. Cui, C. T. Buru, Z. Li, J. T. Hupp and O. K. Farha, *J. Am. Chem. Soc.*, 2018, **140**, 8652–8656.
146 J. G. Knapp, X. Zhang, T. Elkin, L. E. Wolfsberg, S. L. Hanna, F. A. Son, B. L. Scott and O. K. Farha, *CrystEngComm*, 2020, **22**, 2097–2102.
147 T. A. Goetjen, X. Zhang, J. Liu, J. T. Hupp and O. K. Farha, *ACS Sustainable Chem. Eng.*, 2019, **7**, 2553–2557.
148 T.-F. Liu, N. A. Vermeulen, A. J. Howarth, P. Li, A. A. Sarjeant, J. T. Hupp and O. K. Farha, *Eur. J. Inorg. Chem.*, 2016, 4349–4352.
149 Z. Li, A. W. Peters, V. Bernales, M. A. Ortuño, N. M. Schweitzer, M. R. DeStefano, L. C. Gallington, A. E. Platero-Prats, K. W. Chapman, C. J. Cramer, L. Gagliardi, J. T. Hupp and O. K. Farha, *ACS Cent. Sci.*, 2017, **3**, 31–38.
150 C. D. Malonzo, S. M. Shaker, L. Ren, S. D. Prinslow, A. E. Platero-Prats, L. C. Gallington, J. Borycz, A. B. Thompson, T. C. Wang, O. K. Farha, J. T. Hupp, C. C. Lu, K. W. Chapman, J. C. Myers, R. L. Penn, L. Gagliardi, M. Tsapatsis and A. Stein, *J. Am. Chem. Soc.*, 2016, **138**, 2739–2748.
151 P. Deria, J. E. Mondloch, O. Karagiaridi, W. Bury, J. T. Hupp and O. K. Farha, *Chem. Soc. Rev.*, 2014, **43**, 5896–5912.
152 W. Zhao, Z. Wang, C. D. Malonzo, T. E. Webber, A. E. Platero-Prats, F. Sotomayor, N. A. Vermeulen, T. C. Wang, J. T. Hupp, O. K. Farha, R. L. Penn, K. W. Chapman, M. Thommes and A. Stein, *Chem. Mater.*, 2018, **30**, 1301–1315.
153 C. D. Malonzo, Z. Wang, J. Duan, W. Zhao, T. E. Webber, Z. Li, I. S. Kim, A. Kumar, A. Bhan, A. E. Platero-Prats,

K. W. Chapman, O. K. Farha, J. T. Hupp, A. B. F. Martinson, R. L. Penn and A. Stein, *Inorg. Chem.*, 2018, **57**, 2782–2790.
154 Y. Cui, Y. Yue, G. Qian and B. Chen, *Chem. Rev.*, 2012, **112**, 1126–1162.
155 W. P. Lustig, S. Mukherjee, N. D. Rudd, A. V. Desai, J. Li and S. K. Ghosh, *Chem. Soc. Rev.*, 2017, **46**, 3242–3285.
156 W. Cho, H. J. Lee, G. Choi, S. Choi and M. Oh, *J. Am. Chem. Soc.*, 2014, **136**, 12201–12204.
157 A. Karmakar, P. Samanta, S. Dutta and S. K. Ghosh, *Chem. – Asian J.*, 2019, **14**, 4506–4519.
158 R. A. Bermúdez, Y. Colón, G. A. Tejada and J. L. Colón, *Langmuir*, 2005, **21**, 890–895.
159 F. M. Winnik, *Chem. Rev.*, 1993, **93**, 587–614.
160 Y. Ge, Y. Wen, H. Liu, T. Lu, Y. Yu, X. Zhang, B. Li, S.-T. Zhang, W. Li and B. Yang, *J. Mater. Chem. C*, 2020, **8**, 11830–11838.
161 G. K. Bains, S. H. Kim, E. J. Sorin and V. Narayanaswami, *Biochem*, 2012, **51**, 6207–6219.
162 T. Itoh, *Chem. Rev.*, 2012, **112**, 4541–4568.
163 R. Dalapati and S. Biswas, *Sens. Actuators, B*, 2017, **239**, 759–767.
164 S.-Y. Moon, A. J. Howarth, T. Wang, N. A. Vermeulen, J. T. Hupp and O. K. Farha, *Chem. Commun.*, 2016, **52**, 3438–3441.
165 Y. Tang, H. Wu, J. Chen, J. Jia, J. Yu, W. Xu, Y. Fu, Q. He, H. Cao and J. Cheng, *Dyes Pigm.*, 2019, **167**, 10–15.
166 R. Dalapati and S. Biswas, *Inorg. Chem.*, 2019, **58**, 5654–5663.
167 M. Gong, J. Yang, Y. Li, Q. Zhuang and J. Gu, *J. Mater. Chem. C*, 2019, **7**, 12674–12681.
168 L. Guo, M. Wang and D. Cao, *Small*, 2018, **14**, 1703822.
169 P. Deria, J. Yu, T. Smith and R. P. Balaraman, *J. Am. Chem. Soc.*, 2017, **139**, 5973–5983.
170 Z.-J. Lin, H.-Q. Zheng, H.-Y. Zheng, L.-P. Lin, Q. Xin and R. Cao, *Inorg. Chem.*, 2017, **56**, 14178–14188.
171 C. Liu and B. Yan, *Sens. Actuators, B*, 2016, **235**, 541–546.
172 J. Kim, J. S. Oh, K. C. Park, G. Gupta and C. Yeon Lee, *Inorg. Chim. Acta*, 2019, **486**, 69–73.
173 Y. Zhou, Q. Yang, J. Cuan, Y. Wang, N. Gan, Y. Cao and T. Li, *Analyst*, 2018, **143**, 3628–3634.
174 D. Ning, Q. Liu, Q. Wang, X.-M. Du, Y. Li and W.-J. Ruan, *Dalton Trans.*, 2019, **48**, 5705–5712.
175 S. Zhu and D. Wang, *Adv. Energy Mater.*, 2017, **7**, 1700841.
176 Y. Liu, C. T. Buru, A. J. Howarth, J. J. Mahle, J. H. Buchanan, J. B. DeCoste, J. T. Hupp and O. K. Farha, *J. Mater. Chem. A*, 2016, **4**, 13809–13813.
177 M. C. DeRosa and R. J. Crutchley, *Coord. Chem. Rev.*, 2002, **233–234**, 351–371.
178 K. K. Ng and G. Zheng, *Chem. Rev.*, 2015, **115**, 11012–11042.
179 A. Atilgan, T. Islamoglu, A. J. Howarth, J. T. Hupp and O. K. Farha, *ACS Appl. Mater. Interfaces*, 2017, **9**, 24555–24560.
180 A. J. Howarth, C. T. Buru, Y. Liu, A. M. Ploskonka, K. J. Hartlieb, M. McEntee, J. J. Mahle, J. H. Buchanan, E. M. Durke, S. S. Al-Juaid, J. F. Stoddart, J. B. DeCoste, J. T. Hupp and O. K. Farha, *Chem. – Eur. J.*, 2017, **23**, 214–218.
181 T. Zhang, P. Wang, Z. Gao, Y. An, C. He and C. Duan, *RSC Adv.*, 2018, **8**, 32610–32620.
182 H. Choi, A. W. Peters, H. Noh, L. C. Gallington, A. E. Platero-Prats, M. R. DeStefano, M. Rimoldi, S. Goswami, K. W. Chapman, O. K. Farha and J. T. Hupp, *ACS Appl. Energy Mater*, 2019, **2**, 8695–8700.
183 Y. Chen, P. Li, J. Zhou, C. T. Buru, L. Đorđević, P. Li, X. Zhang, M. M. Cetin, J. F. Stoddart, S. I. Stupp, M. R. Wasielewski and O. K. Farha, *J. Am. Chem. Soc.*, 2020, **142**, 1768–1773.
184 A. W. Peters, Z. Li, O. K. Farha and J. T. Hupp, *ACS Appl. Mater. Interfaces*, 2016, **8**, 20675–20681.
185 X. Li, J. Yu, D. J. Gosztola, H. C. Fry and P. Deria, *J. Am. Chem. Soc.*, 2019, **141**, 16849–16857.
186 J. Yu, J. Park, A. Van Wyk, G. Rumbles and P. Deria, *J. Am. Chem. Soc.*, 2018, **140**, 10488–10496.
187 E. Caballero-Mancebo, B. Cohen, S. Smolders, D. E. De Vos and A. Douhal, *Adv. Sci.*, 2019, **6**, 1901020.
188 I. Choudhuri and D. G. Truhlar, *J. Phys. Chem. C*, 2020, **124**, 8504–8513.
189 P. P. Bag, X.-S. Wang, P. Sahoo, J. Xiong and R. Cao, *Catal. Sci. Technol.*, 2017, **7**, 5113–5119.
190 Y. Xiao, Y. Qi, X. Wang, X. Wang, F. Zhang and C. Li, *Adv. Mater.*, 2018, **30**, 1803401.
191 Y. Xiao, X. Guo, J. Liu, L. Liu, F. Zhang and C. Li, *Chin. J. Catal.*, 2019, **40**, 1339–1344.
192 C. T. Buru, M. B. Majewski, A. J. Howarth, R. H. Lavroff, C.-W. Kung, A. W. Peters, S. Goswami and O. K. Farha, *ACS Appl. Mater. Interfaces*, 2018, **10**, 23802–23806.
193 H. Noh, Y. Yang, S. Ahn, A. W. Peters, O. K. Farha and J. T. Hupp, *J. Electrochem. Soc.*, 2019, **166**, H3154–H3158.
194 M. S. Lee, S. J. Garibay, A. M. Ploskonka and J. B. DeCoste, *MRS Commun.*, 2019, **9**, 464–473.
195 W. Zhang, Y. Ma, I. A. Santos-Loópez, J. M. Lownsbury, H. Yu, W.-G. Liu, D. G. Truhlar, C. T. Campbell and O. E. Vilches, *J. Am. Chem. Soc.*, 2018, **140**, 328–338.
196 R.-J. Li, M. Li, X.-P. Zhou, D. Li and M. O'Keeffe, *Chem. Commun.*, 2014, **50**, 4047–4049.
197 S. Vandenbrande, T. Verstraelen, J. J. Gutiérrez-Sevillano, M. Waroquier and V. Van Speybroeck, *J. Phys. Chem. C*, 2017, **121**, 25309–25322.
198 G. O. Vissers, W. Zhang, O. E. Vilches, W.-G. Liu, H. S. Yu, D. G. Truhlar and C. T. Campbell, *J. Phys. Chem. C*, 2019, **123**, 6586–6591.
199 S. J. Garibay, I. Iordanov, T. Islamoglu, J. B. DeCoste and O. K. Farha, *CrystEngComm*, 2018, **20**, 7066–7070.
200 J. H. Kang, T.-U. Yoon, S.-Y. Kim, M.-B. Kim, H.-J. Kim, H.-C. Yang and Y.-S. Bae, *Microporous Mesoporous Mater.*, 2019, **281**, 84–91.
201 E. M. Dias and C. Petit, *J. Mater. Chem. A*, 2015, **3**, 22484–22506.
202 S. Kato, R. J. Drout and O. K. Farha, *Cell Rep.*, 2020, **1**, 100006.

203 S. Rangwani, A. J. Howarth, M. R. DeStefano, C. D. Malliakas, A. E. Platero-Prats, K. W. Chapman and O. K. Farha, *Polyhedron*, 2018, **151**, 338–343.
204 A. J. Howarth, M. J. Katz, T. C. Wang, A. E. Platero-Prats, K. W. Chapman, J. T. Hupp and O. K. Farha, *J. Am. Chem. Soc.*, 2015, **137**, 7488–7494.
205 J. Li, X. Li, T. Hayat, A. Alsaedi and C. Chen, *ACS Sustainable Chem. Eng.*, 2017, **5**, 11496–11503.
206 Z.-J. Lin, H.-Q. Zheng, H.-Y. Zheng, L.-P. Lin, Q. Xin and R. Cao, *Inorg. Chem.*, 2017, **56**, 14178–14188.
207 I. Akpinar, R. J. Drout, T. Islamoglu, S. Kato, J. Lyu and O. K. Farha, *ACS Appl. Mater. Interfaces*, 2019, **11**, 6097–6103.
208 A. Pankajakshan, M. Sinha, A. A. Ojha and S. Mandal, *ACS Omega*, 2018, **3**, 7832–7839.
209 R. J. Drout, K. Otake, A. J. Howarth, T. Islamoglu, L. Zhu, C. Xiao, S. Wang and O. K. Farha, *Chem. Mater.*, 2018, **30**, 1277–1284.
210 P. Asha, M. Sinha and S. Mandal, *RSC Adv.*, 2017, **7**, 6691–6696.
211 A. M. Plonka, Q. Wang, W. O. Gordon, A. Balboa, D. Troya, W. Guo, C. H. Sharp, S. D. Senanayake, J. R. Morris, C. L. Hill and A. I. Frenkel, *J. Am. Chem. Soc.*, 2017, **139**, 599–602.
212 E. Vargas L and R. Q. Snurr, *Langmuir*, 2015, **31**, 10056–10065.
213 H. Chen and R. Q. Snurr, *Langmuir*, 2020, **36**, 1372–1378.
214 J. Zheng, D. Barpaga, O. Y. Gutiérrez, N. D. Browning, B. L. Mehdi, O. K. Farha, J. A. Lercher, B. P. McGrail and R. K. Motkuri, *ACS Appl. Energy Mater.*, 2018, **1**, 5853–5858.
215 X. Xia, M. Cao, Z. Liu, W. Li and S. Li, *Chem. Eng. Sci.*, 2019, **204**, 48–58.
216 H. Chen, Z. Chen, O. K. Farha and R. Q. Snurr, *ACS Sustainable Chem. Eng.*, 2019, **7**, 18242–18246.
217 Z. Bao, G. Chang, H. Xing, R. Krishna, Q. Ren and B. Chen, *Energy Environ. Sci.*, 2016, **9**, 3612–3641.
218 M. Yabushita, P. Li, K. A. Durkin, H. Kobayashi, A. Fukuoka, O. K. Farha and A. Katz, *Langmuir*, 2017, **33**, 4129–4137.
219 M. Yabushita, P. Li, H. Kobayashi, A. Fukuoka, O. K. Farha and A. Katz, *Chem. Commun.*, 2016, **52**, 11791–11794.
220 M. Yabushita, G. Papa, P. Li, A. Fukuoka, O. K. Farha, B. A. Simmons and A. Katz, *Fuel Process. Technol.*, 2020, **197**, 106189.
221 M. Yabushita, P. Li, V. Bernales, H. Kobayashi, A. Fukuoka, L. Gagliardi, O. K. Farha and A. Katz, *Chem. Commun.*, 2016, **52**, 7094–7097.
222 D. Banerjee, C. M. Simon, A. M. Plonka, R. K. Motkuri, J. Liu, X. Chen, B. Smit, J. B. Parise, M. Haranczyk and P. K. Thallapally, *Nat. Commun.*, 2016, **7**, 1–7.
223 M. Kawabe, K. Masuda and J. Yamaguchi, *J. Phys. Soc. Jpn.*, 1968, **24**, 1281–1285.
224 P. Chen, X. He, M. Pang, X. Dong, S. Zhao and W. Zhang, *ACS Appl. Mater. Interfaces*, 2020, **12**, 20429–20439.
225 S. L. Hanna, D. X. Rademacher, D. J. Hanson, T. Islamoglu, A. K. Olszewski, T. M. Nenoff and O. K. Farha, *Ind. Eng. Chem. Res.*, 2020, **59**, 7520–7526.
226 J. Gascon, A. Corma, F. Kapteijn and F. X. Llabres i Xamena, *ACS Catal.*, 2014, **4**, 361–378.
227 P. D. Tran, A. Le Goff, J. Heidkamp, B. Jousselme, N. Guillet, S. Palacin, H. Dau, M. Fontecave and V. Artero, *Angew. Chem., Int. Ed.*, 2011, **50**, 1371–1374.
228 H. Lei, C. Liu, Z. Wang, Z. Zhang, M. Zhang, X. Chang, W. Zhang and R. Cao, *ACS Catal.*, 2016, **6**, 6429–6437.
229 J. Ye, L. Gagliardi, C. J. Cramer and D. G. Truhlar, *J. Catal.*, 2018, **360**, 160–167.
230 S. Pellizzeri, M. Barona, V. Bernales, P. Miró, P. Liao, L. Gagliardi, R. Q. Snurr and R. B. Getman, *Catal. Today*, 2018, **312**, 149–157.
231 A. Benali, Y. Luo, H. Shin, D. Pahls and O. Heinonen, *J. Phys. Chem. C*, 2018, **122**, 16683–16691.
232 S. P. Desai, J. Ye, T. Islamoglu, O. K. Farha and C. C. Lu, *Organometallics*, 2019, **38**, 3466–3473.
233 M. A. Ortuño, V. Bernales, L. Gagliardi and C. J. Cramer, *J. Phys. Chem. C*, 2016, **120**, 24697–24705.
234 H. Chen, P. Liao, M. L. Mendonca and R. Q. Snurr, *J. Phys. Chem. C*, 2018, **122**, 12362–12368.
235 M. L. Mendonca and R. Q. Snurr, *ACS Catal.*, 2019, **10**, 1310–1323.
236 D. R. Pahls, M. A. Ortuño, P. H. Winegar, C. J. Cramer and L. Gagliardi, *Inorg. Chem.*, 2017, **56**, 8739–8743.
237 M. C. Simons, M. A. Ortuño, V. Bernales, C. A. Gaggioli, C. J. Cramer, A. Bhan and L. Gagliardi, *ACS Catal.*, 2018, **8**, 2864–2869.
238 C. A. Gaggioli, J. Sauer and L. Gagliardi, *J. Am. Chem. Soc.*, 2019, **141**, 14603–14611.
239 B. Yang, K. Sharkas, L. Gagliardi and D. G. Truhlar, *Catal. Sci. Technol.*, 2019, **9**, 7003–7015.
240 J. Ye, C. J. Cramer and D. G. Truhlar, *J. Phys. Chem. C*, 2018, **122**, 26987–26997.
241 L. R. Redfern, Z. Li, X. Zhang and O. K. Farha, *ACS Appl. Nano Mater.*, 2018, **1**, 4413–4417.
242 P. Li, J. A. Modica, A. J. Howarth, E. Vargas, P. Z. Moghadam, R. Q. Snurr, M. Mrksich, J. T. Hupp and O. K. Farha, *Chem*, 2016, **1**, 154–169.
243 R. Gil-San-Millan, E. López-Maya, A. E. Platero-Prats, V. Torres-Pérez, P. Delgado, A. W. Augustyniak, M. K. Kim, H. W. Lee, S. G. Ryu and J. A. Navarro, *J. Am. Chem. Soc.*, 2019, **141**, 11801–11805.
244 C. T. Buru, M. C. Wasson and O. K. Farha, *ACS Appl. Nano Mater.*, 2019, **3**, 658–664.
245 C. T. Buru, P. Li, B. L. Mehdi, A. Dohnalkova, A. E. Platero-Prats, N. D. Browning, K. W. Chapman, J. T. Hupp and O. K. Farha, *Chem. Mater.*, 2017, **29**, 5174–5181.
246 S. Ahn, S. L. Nauert, C. T. Buru, M. Rimoldi, H. Choi, N. M. Schweitzer, J. T. Hupp, O. K. Farha and J. M. Notestein, *J. Am. Chem. Soc.*, 2018, **140**, 8535–8543.
247 C. T. Buru, A. E. Platero-Prats, D. G. Chica, M. G. Kanatzidis, K. W. Chapman and O. K. Farha, *J. Mater. Chem. A*, 2018, **6**, 7389–7394.
248 C. T. Buru, J. Lyu, J. Liu and O. K. Farha, *Front. Mater.*, 2019, **6**, 152.
249 D. Yang, S. O. Odoh, T. C. Wang, O. K. Farha, J. T. Hupp, C. J. Cramer, L. Gagliardi and B. C. Gates, *J. Am. Chem. Soc.*, 2015, **137**, 7391–7396.

250 D. Yang, S. O. Odoh, J. Borycz, T. C. Wang, O. K. Farha, J. T. Hupp, C. J. Cramer, L. Gagliardi and B. C. Gates, *ACS Catal.*, 2016, **6**, 235–247.
251 M. Rimoldi, J. T. Hupp and O. K. Farha, *ACS Appl. Mater. Interfaces*, 2017, **9**, 35067–35074.
252 V. Bernales, D. Yang, J. Yu, G. Gümüslü, C. J. Cramer, B. C. Gates and L. Gagliardi, *ACS Appl. Mater. Interfaces*, 2017, **9**, 33511–33520.
253 I. S. Kim, Z. Li, J. Zheng, A. E. Platero-Prats, A. Mavrandonakis, S. Pellizzeri, M. Ferrandon, A. Vjunov, L. C. Gallington, T. E. Webber, N. A. Vermeulen, R. L. Penn, R. B. Getman, C. J. Cramer, K. W. Chapman, D. M. Camaioni, J. L. Fulton, J. A. Lercher, O. K. Farha, J. T. Hupp and A. B. F. Martinson, *Angew. Chem., Int. Ed.*, 2018, **57**, 909–913.
254 S. P. Desai, J. Ye, J. Zheng, M. S. Ferrandon, T. E. Webber, A. E. Platero-Prats, J. Duan, P. Garcia-Holley, D. M. Camaioni, K. W. Chapman, M. Delferro, O. K. Farha, J. L. Fulton, L. Gagliardi, J. A. Lercher, R. L. Penn, A. Stein and C. C. Lu, *J. Am. Chem. Soc.*, 2018, **140**, 15309–15318.
255 A. B. Thompson, D. R. Pahls, V. Bernales, L. C. Gallington, C. D. Malonzo, T. Webber, S. J. Tereniak, T. C. Wang, S. P. Desai, Z. Li, I. S. Kim, L. Gagliardi, R. L. Penn, K. W. Chapman, A. Stein, O. K. Farha, J. T. Hupp, A. B. F. Martinson and C. C. Lu, *Chem. Mater.*, 2016, **28**, 6753–6762.
256 T. Ikuno, J. Zheng, A. Vjunov, M. Sanchez-Sanchez, M. A. Ortuño, D. R. Pahls, J. L. Fulton, D. M. Camaioni, Z. Li, D. Ray, B. L. Mehdi, N. D. Browning, O. K. Farha, J. T. Hupp, C. J. Cramer, L. Gagliardi and J. A. Lercher, *J. Am. Chem. Soc.*, 2017, **139**, 10294–10301.
257 Z. Li, A. W. Peters, A. E. Platero-Prats, J. Liu, C.-W. Kung, H. Noh, M. R. DeStefano, N. M. Schweitzer, K. W. Chapman, J. T. Hupp and O. K. Farha, *J. Am. Chem. Soc.*, 2017, **139**, 15251–15258.
258 M. Rimoldi, V. Bernales, J. Borycz, A. Vjunov, L. C. Gallington, A. E. Platero-Prats, I. S. Kim, J. L. Fulton, A. B. F. Martinson, J. A. Lercher, K. W. Chapman, C. J. Cramer, L. Gagliardi, J. T. Hupp and O. K. Farha, *Chem. Mater.*, 2017, **29**, 1058–1068.
259 M. Rimoldi, L. C. Gallington, K. W. Chapman, K. MacRenaris, J. T. Hupp and O. K. Farha, *Chem. – Eur. J.*, 2017, **23**, 8532–8536.
260 M. Yabushita, P. Li, T. Islamoglu, H. Kobayashi, A. Fukuoka, O. K. Farha and A. Katz, *Ind. Eng. Chem. Res.*, 2017, **56**, 7141–7148.
261 J. Liu, J. Ye, Z. Li, K.-I. Otake, Y. Liao, A. W. Peters, H. Noh, D. G. Truhlar, L. Gagliardi, C. J. Cramer, O. K. Farha and J. T. Hupp, *J. Am. Chem. Soc.*, 2018, **140**, 11174–11178.
262 S. Ahn, N. E. Thornburg, Z. Li, T. C. Wang, L. C. Gallington, K. W. Chapman, J. M. Notestein, J. T. Hupp and O. K. Farha, *Inorg. Chem.*, 2016, **55**, 11954–11961.
263 R. C. Klet, S. Tussupbayev, J. Borycz, J. R. Gallagher, M. M. Stalzer, J. T. Miller, L. Gagliardi, J. T. Hupp, T. J. Marks, C. J. Cramer, M. Delferro and O. K. Farha, *J. Am. Chem. Soc.*, 2015, **137**, 15680–15683.
264 J. Liu, L. R. Redfern, Y. Liao, T. Islamoglu, A. Atilgan, O. K. Farha and J. T. Hupp, *ACS Appl. Mater. Interfaces*, 2019, **11**, 47822–47829.
265 A. W. Peters, K. Otake, A. E. Platero-Prats, Z. Li, M. R. DeStefano, K. W. Chapman, O. K. Farha and J. T. Hupp, *ACS Appl. Mater. Interfaces*, 2018, **10**, 15073–15078.
266 K. Berijani, A. Morsali and J. T. Hupp, *Catal. Sci. Technol.*, 2019, **9**, 3388–3397.
267 J. Liu, Z. Li, X. Zhang, K.-I. Otake, L. Zhang, A. W. Peters, M. J. Young, N. M. Bedford, S. P. Letourneau, D. J. Mandia, J. W. Elam, O. K. Farha and J. T. Hupp, *ACS Catal.*, 2019, **9**, 3198–3207.
268 M. C. de Koning, G. W. Peterson, M. van Grol, I. Iordanov and M. McEntee, *Chem. Mater.*, 2019, **31**, 7417–7424.
269 M. Rimoldi, A. Nakamura, N. A. Vermeulen, J. J. Henkelis, A. K. Blackburn, J. T. Hupp, J. F. Stoddart and O. K. Farha, *Chem. Sci.*, 2016, **7**, 4980–4984.
270 S. T. Madrahimov, J. R. Gallagher, G. Zhang, Z. Meinhart, S. J. Garibay, M. Delferro, J. T. Miller, O. K. Farha, J. T. Hupp and S. T. Nguyen, *ACS Catal.*, 2015, **5**, 6713–6718.
271 Y.-B. Huang, M. Shen, X. Wang, P. Huang, R. Chen, Z.-J. Lin and R. Cao, *J. Catal.*, 2016, **333**, 1–7.
272 Q. Shi, S. Fu, C. Zhu, J. Song, D. Du and Y. Lin, *Mater. Horiz.*, 2019, **6**, 684–702.
273 R. R. Salunkhe, Y. V. Kaneti, J. Kim, J. H. Kim and Y. Yamauchi, *Acc. Chem. Res.*, 2016, **49**, 2796–2806.
274 R. Zhao, Z. Liang, R. Zou and Q. Xu, *Joule*, 2018, **2**, 2235–2259.
275 S. Patwardhan and G. C. Schatz, *J. Phys. Chem. C*, 2015, **119**, 24238–24247.
276 T. C. Wang, I. Hod, C. O. Audu, N. A. Vermeulen, S. T. Nguyen, O. K. Farha and J. T. Hupp, *ACS Appl. Mater. Interfaces*, 2017, **9**, 12584–12591.
277 C.-W. Kung, K. Otake, C. T. Buru, S. Goswami, Y. Cui, J. T. Hupp, A. M. Spokoyny and O. K. Farha, *J. Am. Chem. Soc.*, 2018, **140**, 3871–3875.
278 S. Goswami, D. Ray, K.-I. Otake, C.-W. Kung, S. J. Garibay, T. Islamoglu, A. Atilgan, Y. Cui, C. J. Cramer, O. K. Farha and J. T. Hupp, *Chem. Sci.*, 2018, **9**, 4477–4482.
279 I. Hod, W. Bury, D. M. Gardner, P. Deria, V. Roznyatovskiy, M. R. Wasielewski, O. K. Farha and J. T. Hupp, *J. Phys. Chem. Lett.*, 2015, **6**, 586–591.
280 A. Van Wyk, T. Smith, J. Park and P. Deria, *J. Am. Chem. Soc.*, 2018, **140**, 2756–2760.
281 P. J. Celis-Salazar, M. Cai, C. A. Cucinell, S. R. Ahrenholtz, C. C. Epley, P. M. Usov and A. J. Morris, *J. Am. Chem. Soc.*, 2019, **141**, 11947–11953.
282 S. Goswami, I. Hod, J. D. Duan, C.-W. Kung, M. Rimoldi, C. D. Malliakas, R. H. Palmer, O. K. Farha and J. T. Hupp, *J. Am. Chem. Soc.*, 2019, **141**, 17696–17702.
283 C.-W. Kung, J. E. Mondloch, T. C. Wang, W. Bury, W. Hoffeditz, B. M. Klahr, R. C. Klet, M. J. Pellin, O. K. Farha and J. T. Hupp, *ACS Appl. Mater. Interfaces*, 2015, **7**, 28223–28230.

284 I. Hod, W. Bury, D. M. Karlin, P. Deria, C.-W. Kung, M. J. Katz, M. So, B. Klahr, D. Jin, Y.-W. Chung, T. W. Odom, O. K. Farha and J. T. Hupp, *Adv. Mater.*, 2014, **26**, 6295–6300.
285 L. Besra and M. Liu, *Prog. Mater. Sci.*, 2007, **52**, 1–61.
286 P. R. McGonigal, P. Deria, I. Hod, P. Z. Moghadam, A.-J. Avestro, N. E. Horwitz, I. C. Gibbs-Hall, A. K. Blackburn, D. Chen, Y. Y. Botros, M. R. Wasielewski, R. Q. Snurr, J. T. Hupp, O. K. Farha and J. F. Stoddart, *Proc. Natl. Acad. Sci. U. S. A.*, 2015, **112**, 11161–11168.
287 Q. Chen, J. Sun, P. Li, I. Hod, P. Z. Moghadam, Z. S. Kean, R. Q. Snurr, J. T. Hupp, O. K. Farha and J. F. Stoddart, *J. Am. Chem. Soc.*, 2016, **138**, 14242–14245.
288 Y. Diao, J. Hu, S. Cheng, F. Ma, M.-Q. Li, X. Hu, Y. Y. Li, J. He and Z. Xu, *Inorg. Chem.*, 2020, **59**, 5626–5631.
289 H. Noh, C.-W. Kung, K.-I. Otake, A. W. Peters, Z. Li, Y. Liao, X. Gong, O. K. Farha and J. T. Hupp, *ACS Catal.*, 2018, **8**, 9848–9858.
290 H. Noh, Y. Yang, X. Zhang, T. A. Goetjen, Z. H. Syed, Z. Lu, S. Ahn, O. K. Farha and J. T. Hupp, *ChemElectroChem*, 2020, **7**, 509–516.
291 C.-W. Kung, C. O. Audu, A. W. Peters, H. Noh, O. K. Farha and J. T. Hupp, *ACS Energy Lett.*, 2017, **2**, 2394–2401.
292 A. G. Wallace and M. D. Symes, *Trends Chem.*, 2019, **1**, 247–258.
293 S. Kato, K.-i. Otake, H. Chen, I. Akpinar, C. T. Buru, T. Islamoglu, R. Q. Snurr and O. K. Farha, *J. Am. Chem. Soc.*, 2019, **141**, 2568–2576.
294 X. Zhao, Z. Zhang, X. Cai, B. Ding, C. Sun, G. Liu, C. Hu, S. Shao and M. Pang, *ACS Appl. Mater. Interfaces*, 2019, **11**, 7884–7892.
295 X. Zhao, S. Liu, C. Hu, Y. Liu, M. Pang and J. Lin, *ACS Appl. Bio Mater.*, 2019, **2**, 4436–4441.
296 M. Pander, A. Żelichowska and W. Bury, *Polyhedron*, 2018, **156**, 131–137.
297 M. H. Teplensky, M. Fantham, P. Li, T. C. Wang, J. P. Mehta, L. J. Young, P. Z. Moghadam, J. T. Hupp, O. K. Farha, C. F. Kaminski and D. Fairen-Jimenez, *J. Am. Chem. Soc.*, 2017, **139**, 7522–7532.
298 Y. Chen, P. Li, J. A. Modica, R. J. Drout and O. K. Farha, *J. Am. Chem. Soc.*, 2018, **140**, 5678–5681.
299 S. Wang, Y. Chen, S. Wang, P. Li, C. A. Mirkin and O. K. Farha, *J. Am. Chem. Soc.*, 2019, **141**, 2215–2219.
300 D. Chen, D. Yang, C. A. Dougherty, W. Lu, H. Wu, X. He, T. Cai, M. E. Van Dort, B. D. Ross and H. Hong, *ACS Nano*, 2017, **11**, 4315–4327.
301 Z. Hu, C. Qiao, Z. Xia, F. Li, J. Han, Q. Wei, Q. Yang, G. Xie, S. Chen and S. Gao, *ACS Appl. Mater. Interfaces*, 2020, **12**, 14914–14923.